Stony Brook University

Characterization of cellular mechanisms involved in CO_2/H^+ chemoreception using a mathematical model

A Dissertation presented

by

Juan Manuel Cordovez

to

The Graduate School

in Partial Fulfillment of the

requirements

for the Degree of

Doctor of Philosophy

in

Biomedical Engineering

Stony Brook University

December 2009

Stony Brook University

The Graduate School

Juan Manuel Cordovez

We, the dissertation committee for the above candidate for the Doctor of Philosophy degree, hereby recommend acceptance of this dissertation.

Irene C. Solomon. Advisor
Associate professor. Physiology and Biophysics

Emilia Entcheva. Chairperson of defense
Associate professor. Biomedical Engineering

Leon C. Moore
Professor. Physiology and Biophysics

Chris Clausen
Associate professor. Physiology and Biophysics

Steve Hempleman
Professor. Northern Arizona University. Biological Sciences

This dissertation is accepted by the graduate school

Lawrence Martin
Dean of the Graduate School

Abstract of the dissertation

Characterization of cellular mechanisms involved in CO_2/H^+ chemoreception using a mathematical model

by

Juan Manuel Cordovez

in

Biomedical Engineering

Stony Brook University

2009

Specialized neurons located in different regions of the brainstem have been identified as central respiratory chemoreceptors (CRC), whose primary role is to transduce changes in CO_2/H^+ levels into an electrical response that leads to adjustments in ventilation and restoration of normal levels of arterial CO_2. Despite intensive research, the cellular mechanisms mediating this response have remained elusive. Nevertheless, it is known that during hypercapnic acidosis (HA), intracellular pH (pH_i) in CRC falls and no pH_i recovery occurs; while in non-chemosensitive neurons, pH_i recovery is seen during HA. CRC also change their firing rate in response to acidification, suggesting a link between pH_i regulation and the electrical response. To investigate potential mechanisms for these responses, we developed a mathematical model to study pH_i regulation in CRC and non-chemosensitive neurons. The model includes kinetic descriptions of the Na^+/H^+ exchanger, the Cl^-/HCO_3^- exchanger, and carbonic anhydrase as well as cell volume regulation (via NKCC and KCC cotransporters) and passive diffusion of major ions. Simulation experiments demonstrated that differences between CRC and non-chemosensitive neurons cannot be explained by different NHE isoforms; however, alterations in this transport mechanism affect the ability of the neuron to regulate pH_i, indicating that different levels of expression and/or an unidentified isoform may participate. To address the link between pH_i regulation and cell excitability, the model was expanded to include mechanisms for action-potential generation. To accomplish this, parameters for fast and slow Na^+ and K^+ currents were identified using a typical Hodgkin-Huxley (HH) excitable cell model, and then incorporated into our transport model. Simulation experiments revealed that (1) the small changes in ionic composition seen during HA are sufficient to alter the electrical state of the neuron and drive the HA-induced increase in firing frequency, demonstrating that Ca^{2+} and pH sensitive K^+ channels are not required for the excitable response, and (2) HCO_3^- is an important element for modulation of the excitable response during HA. We conclude that differences in multiple, not single, cellular mechanisms mediate the different behaviors of CRC and non-chemosensitive neurons.

To Julieta, Eva, and Violeta.
For their support and inspiration.

Table of contents

List of Symbols

Symbol	Description	Units
W	Cell Volume	cm^3
A	Cell Area	cm^2
i	Superscript denoting intracellular	
o	Superscript denoting extracellular	
j	Subscript denoting solute (Na^+, K^+, etc.) or Buffer system	
z_j	Valence of solute j	
C_j^i	Intracellular concentration of solute j	mM
C_j^o	Extracellular concentration of solute j	mM
J_j	Flux of solute j	$\mu mol \cdot s^{-1} \cdot cm^{-2}$
J_W	Water Flux	$cm^3 \cdot s^{-1} \cdot cm^{-2}$
P_j	Diffusive membrane permeability of solute j	$cm \cdot s^{-1}$
P_W	Membrane water permeability	$cm \cdot s^{-1} \cdot mM^{-1}$
σ_j	Reflection constant of solute j	
F	Faraday's constant	$coul \cdot mol^{-1}$
R	Gas Constant	$J \cdot mol^{-1} \cdot K^{-1}$
T	Absolute Temperature	K
V	Membrane Potential	mV
U	Normalized membrane potential [=VF/(RT)]	
I_j	Ionic current (= Fz_jJ_j)	$\mu A \cdot cm^{-2}$
I_T	Total ionic current ($= \sum_j I_j$)	$\mu A \cdot cm^{-2}$
Na^+-K^+-ATPase Parameters		
i_p	Net pump current	$\mu A \cdot cm^{-2}$
i_{max}	Maximum pump current	$\mu A \cdot cm^{-2}$

$K_{Na,p}$	C^i_{Na} producing half-maximal pump current	mM
$K_{K,p}$	C^o_K producing half-maximal pump current	mM
Proton buffers CO_2		
K_j	Equilibrium constant of the buffer system *j*	mM
B^o_j	Total extracellular concentration of buffer system *j*	mM
B^i_j	Total intracellular concentration of buffer system *j*	mM
H^i_T	Total intracellular concentration of H^+ and proton donors	mM
H^o_T	Total extracellular concentration of H^+ and proton donors	mM
k_h	CO_2 hydration rate constant	s^{-1}
k_d	CO_2 dehydration rate constant	s^{-1}
C_{CO2}	CO_2 concentration [= $0.03P_{CO2}$ (mmHg)]	mM
Na^+-H^+ Exchanger		
K_{Na}	Na^+ equilibrium constant	mM
K_K	K^+ equilibrium constant	mM
K_{NH4}	NH_4^+ equilibrium constant	mM
p_{Na}	Na^+ permeation coefficient	$cm \cdot s^{-1}$
p_H	K^+ permeation coefficient	$cm \cdot s^{-1}$
p_{NH4}	NH_4^+ permeation coefficient	$cm \cdot s^{-1}$
E_{NHE}	Total amount of carrier	arbitrary units
Cl^--HCO_3^+ Exchanger		
k_1-k_{12}	Rate constants	s^{-1} or $mM^{-1} \cdot s^{-1}$
k_{Cl}	Cl^- dissociation constant	mM

k_{HCO3}	HCO_3^- dissociation constant	mM
E_{AE}	Total amount of carrier	arbitrary units
$Na^+,K^+,2Cl^-$ cotransporter (KCC)		
E_{NKCC}^{MAX}	Maximum amount of carrier	arbitrary units
E_{NKCC}^{MIN}	Minimum amount of carrier	arbitrary units
E_{NKCC}	Amount of carrier $(E_{KCC}^{MIN} < E_{KCC} < E_{KCC}^{MAX})$	arbitrary units
K^+,Cl^- cotransporter (KCC)		
E_{KCC}^{MAX}	Maximum amount of carrier	arbitrary units
E_{KCC}^{MIN}	Minimum amount of carrier	arbitrary units
E_{KCC}	Amount of carrier $(E_{KCC}^{MIN} < E_{KCC} < E_{KCC}^{MAX})$	arbitrary units
Excitability variables and parameters		
c_m	Membrane capacitance	$\mu F \cdot cm^{-2}$ or pF
g_j	Ionic conductance for ion *j*	nS
$\bar{g}_j$	Maximum ionic conductance for ion *j*	nS
E_j	Equilibrium potential for ion *j*	mV
x	Index referring to gating variable (m,n or h)	
α_x	Forward rate constant for gating variable *x*	
β_x	Reverse rate constant for gating variable *x*	
x_∞	Steady-state value for gating variable *x*	
τ_x	Time constant for gating variable *x*	ms

List of Figures

List of Tables

Acknowledgment

I would like to leave a note about my gratitude and appreciation for the help and support I received during these years from my committee members. In particular to Dr. Solomon, Dr. Clausen and Dr. Moore. I am fortunate to say that I do not only consider them people with the highest scientific merit but also with exceptional human values. Thanks to them, I would never forget these fascinating years at Stony Brook.

Chapter 1. Preliminary comments

1.1 Introduction and Motivation

Organisms maintain whole body homeostasis by adjusting their metabolic rates, behavioral responses, and energy expenditure. Such responses require sensors that monitor the internal/external environment continuously, and these sensors must connect to the appropriate regions of the body to elicit an appropriate and coordinated response. One of the most remarkable mechanisms for cell and whole body homeostasis is respiration. The continuous movement of air into and out of the body, which is referred to as ventilation, not only brings the oxygen (O_2) required for metabolic activities but also removes waste in the form of carbon dioxide (CO_2), which is produced by the process of cellular metabolism. CO_2 is considered to be freely permeable across cell membranes, and its accumulation affects pH in every compartment in the body. An increase in CO_2 causes a decrease in pH (referred to as acidosis) while a decrease in CO_2 produces an increase in pH (referred to as alkalosis). pH is important for cell survival since pH affects the rates of reactions and dictates the state or structural conformation of vital proteins. Not surprisingly, CO_2/H^+ sensors have been found in virtually all multi-cellular organisms, and in particular, mammals have two sets of such sensors. One set is located peripherally at the level of the carotid bodies, and the second set resides within the central nervous system (CNS) in the brainstem. Peripheral chemoreceptors sense primarily O_2 but are also capable of sensing CO_2 and H^+, in what is called the modulatory effect of O_2 (42, 61). When O_2 levels are within the normal range, peripheral chemoreceptors do not contribute to the response to increased CO_2/H^+ levels, but when CO_2/H^+ levels are enhanced, reductions in O_2 exacerbate the the ventilatory response. Since both sets of chemoreceptors affect gas composition in the alveoli, their primary role is related to respiration. Central respiratory chemoreceptors (CRC) sense mainly CO_2/H^+, and affect respiration by adjusting the rate and depth of ventilation. These adjustments represent an initial response that brings blood gases back to normal, but full compensation of changes in blood pH require participation of the kidneys.

Central CO_2/H^+ chemoreception, as it relates to ventilation, occurs only in excitable cells; however, all cells in the body exhibit CO_2/H^+ reactions. Thus, for a cell to be considered a CRC, it must be capable of transmitting the CO_2/H^+ signal immediately to the appropriate respiratory-related CNS circuits. CRC interact with respiratory nuclei where respiratory rhythm is generated (i.e., the central pattern generator (CPG)), so that changes in CO_2/H^+ can be rapidly compensated for by changes in ventilation. CRC are believed to be located in multiple regions of the brainstem, many of which participate in functions ranging from breathing automaticity during sleep and wakefulness to control of breathing during active exercise. Diseases that affect CRC, like the congenital central hypoventilation syndrome (CCHS), central sleep apnea, and sudden infant death syndrome

(SIDS), are life threatening diseases that would benefit from improved understanding of the mechanisms by which CRC function.

Finally, many key questions in the field of central CO_2/H^+ chemoreception remain to be fully elucidated. These include: What are the mechanisms by which CRC detect changes in CO_2/H^+? How many CRC are there and where are they located? What is the role of each one of the CRC sites? What are the sensing molecules and what is(are) the signal(s)? How do these sensing molecules affect cell activity to adjust ventilation? How do CRC interact with the respiratory CPG? In the following sections, we review some of the main topics in central CO_2/H^+ chemoreception, and introduce the reader to our approach for studying some of these issues.

1.2 Background and significance

History of studies in central chemoreception

The simple activity of moving air into and out of our bodies, which is referred to a ventilation or breathing, is a fundamental requirement for life. Yet, we do not understand it completely. Breathing is obviously important for gas exchange with the environment (delivery of O_2 to and removal of CO_2 from the body), but the respiratory system also supports a series of important homeostatic physiological functions like acid/base regulation, phonation, and protection against hazardous substances (44, 45). It is known that an elevation of CO_2 is the main stimulus to increase ventilation, and specialized cells located both peripherally in the carotid bodies and centrally in the brainstem sense changes in O_2, CO_2, and/or H^+, and alter ventilation accordingly. These observations, which seem obvious, are the result of over a century of research, which is filled with many interesting historical findings, some of which will be re-visited here. The information provided below has been the topic of a number of extensive reviews and studies (44, 56, 58, 79, 86, 110, 151, 153, 154) and will therefore only be briefly reviewed here.

Early studies of CRC date back before 1900. It was probably Haldane (1860-1936) who planted in our minds the idea of a single signal that correlates with an increase/decrease in ventilation (59); this idea has never been abandoned completely (110). He thought that it was mainly CO_2 that drives ventilation based on his animal experiments, but also attributed a minor role for O_2 in ventilatory drive based on the increase in ventilation seen during hypoxia. He postulated that both signals exerted the common effect of increasing H^+ concentration in the brain (59), but a few years later, it was found that although hypoxia increases ventilation, it may also increase arterial pH (a finding that is contrary to the observation that low pH increases ventilation) (86, 95, 112). This observation ultimately turned out to be a confounding effect arising from the peripheral chemoreceptors (which had not yet been identified), but it suggested that changes in ventilatory drive could not be explained exclusively by an increase in H^+ (fall in pH).

A few years later, Winterstein, in what he called the *reaction theory*, proposed that CO_2 and O_2 act on a single receptor by a single mechanism (153). The common factor was H^+ in the blood, which were produced by the hydration of CO_2 or acid formation during hypoxia. This idea was basically a formalization of Haldane's observations (110, 112). Later, it was clear that the reaction theory did not hold based on a number of earlier different findings. Amongst these findings were the observations of Collip (32), who demonstrated that ventilation increases in response to the addition of HCO_3^- to the blood even though this perturbation increases blood pH and Winterstein himself, who found that the addition of NH_4Cl, which acidifies the blood, decreases ventilation; both of these observations are at odds with the reaction theory (86). Thus, in his modified version of the reaction theory, Winterstein separated the effects of pH changes in the blood from pH changes in the respiratory center. Moreover, Jacobs (134) found that the addition of HCO_3^- and NH_4Cl to the blood caused intracellular alkalinization and acidification, respectively, which would be expected when outside pH (pH_o) is kept constant (152). Accordingly, Winterstein proposed that an increase in CO_2 or decrease in O_2 would augment ventilation by reducing pH at the chemoreceptor site. Unfortunately, it was not clear whether this referred to intracellular pH (pH_i) or the pH surrounding the chemoreceptors (110).

At about the same time Winterstein presented his original *reaction theory*, Gray (54) published what would become the first model of central respiratory chemoreception. Gray's theory, known as the multiple factors theory, proposed that CO_2, O_2, and pH are all being sensed by different receptors in different places, and they exert different effects on respiratory output. The theory accounts for the observations that hypercapnic acidosis (HA), an increase in CO_2 that causes a decrease in pH_i, produces a greater increase in ventilation compared to metabolic acidosis while a decrease in O_2 causes a diminished, but still, an increase in ventilation. Gray did not address the cellular mechanisms by which the cell could detect changes in these species. As such, his model can hardly be challenged, but it reflects the findings that centers outside of the brain can control ventilation. These centers outside of the brain were characterized by the classical experiments of Heymans and Heymans (70) where they showed that hypercapnia or anoxemia increases ventilation when applied on the carotid bodies, which are known today as peripheral chemoreceptors. Later, Heymans demonstrated that transection of afferent fibers from the carotid body eliminates the hyperventilatory response to hypoxia (61).

After multiple demonstrations that H^+ concentration is fundamental to the ventilatory response, investigators started to realize that pH can be measured in many places and, contrary to the beliefs at the time, blood pH does not reflect cerebrospinal fluid (CSF) pH or brain extracellular pH. Jacobs (134) suggested the existence of a barrier between the brain and the blood (blood-brain-barrier) that behaves similar to the cell membrane, and thus prevents charged particles from freely crossing. This idea meant that changes in pH in the blood could result in opposite pH effects in the brain. For example, the addition of HCO_3^- in the

blood, which raises blood pH, would cause acidification in the brain by promoting the permeation of the uncharged carbonic acid (H_2CO_3). When reliable techniques to measure pH_o became available, the idea of a single signal was revived, and this time the candidate was pH_o in the brain. Leusen (84), Pappenheimer (106), and others, used acids to stimulate ventilation in different animal models. Later, Loeschcke (1982) re-stated Winterstein's *reaction theory*, but argued that the signal was pH_o instead of CO_2, and that the receptor had different sensitivity to acidosis depending upon whether the fall in pH was caused by HA or metabolic acidosis. This property was needed to explain the differences in ventilation elicited by HA versus hypoxia (61, 81, 110, 112).

But the difference in ventilation obtained when pH_o is varied under different experimental conditions (e.g., HA versus metabolic acidosis) made many investigators believe that it was not pH_o alone that drives ventilation but rather a combination of CO_2 and pH_o, consistent with the multiple factors theory (110). Others suggested that pH_i rather than pH_o was the correct stimulus (127). Unfortunately, for those who thought that pH_i was the single signal, local CNS hypoxia produces only a decrease in pH_i with no alteration in ventilation.

Evidence for a far more complicated explanation came from studies that exposed neurons to an increase in CO_2, which resulted in a greater decrease in pH_o compared to pH_i due to intracellular buffers. This led to the proposal that the pH_i-pH_o gradient across the membrane dictates the ventilatory response (110). In support of this idea, blocking the intracellular buffering capacity (β_{int}) and allowing pH_i to drop to the same extent as pH_o revealed that the same increase in CO_2 is no longer accompanied by an increase in ventilation (98, 100). This observation suggests that the alteration of the pH_i-pH_o gradient correlates with the ventilatory response. However, the drug used to decrease β_{int} can interfere directly with the receptors.

Many of these studies suffer from methodological concerns and technical limitations. For example, as mentioned previously, it is difficult to determine from many of the studies which tissue pH was actually measured. Also, contributions from peripheral chemoreceptors were only taken into account after their discovery; therefore, the very early studies are difficult to interpret due to unaccounted feedback mechanisms. Finally, the vast majority of these studies treated the surface of ventral medulla as the only chemoreception site and the experimental treatment may have affected other chemosensitive sites (110). Despite these limitations, certain findings are so common that they have to be accounted for by any model of central chemoreception. One of these findings is that acidosis produced by increased CO_2 is a stronger stimulus for increasing ventilation than is metabolic acidosis.

Despite decades of searching for the single stimulus that increases ventilation, it feels like we were still at the beginning awaiting confirmation that the pH_i-pH_o gradient can explain changes in ventilation and fulfill the dream of having one single stimulus that correlates with ventilation. Or, one has to be ready to accept a multiple-factor hypothesis, with receptors that could potentially

be sensing changes in CO_2, pH_i, pH_o, and (why not?) HCO_3^-. To this end, Putnam and colleagues recently proposed a multifactor model for central CO_2/H^+ chemoreception. In this model, they argue that HA increases CO_2 and this has an independent effect on pH_i and pH_o that depends on the β_{int} and pH regulation mechanisms in the neuron. They also propose sensors for both signals in chemosensitive neurons, with these sensors ultimately leading to changes in cell excitability, alteration of firing rates (FR), and modulation of ventilation (73, 110).

Today, we know that CO_2 exerts an effect on ventilation by acidifying CRC. We also know a great deal about the neural circuitry that generates the respiratory rhythm, but we still do not know the molecular mechanisms responsible for the sensing of CO_2/H^+, the relative importance of the different chemoreceptor sites under different behavioral challenges (i.e., awake, sleep, exercise), and if the CRC are composed of cells outside the respiratory nuclei that modulate rhythm (presynaptic) or if they include regular respiratory neurons with CO_2/H^+ sensing capabilities (post synaptic) (71). These important questions remain unanswered.

Evolution of CO_2/H^+ chemosensitivity

CO_2/H^+ chemosensitivity is fundamental for air breathing in tetrapods, nevertheless there is evidence that the origin of central chemoreception goes back to our fish ancestors (2). Traditionally, breathing in fishes was considered driven by peripheral chemoreceptors. However, Wilson reported that elements in the gar brainstem (primitive air breathing fish) are sufficient to produce putative air breathing bursts (150). From lung breathing fishes to current mammals, it is believed that air breathing was invented multiple times, and along with it, central chemosensitivity appeared in those animals (92, 113). Nattie has suggested in an elegant manner that CO_2/H^+ chemoreception could have arisen in a similar fashion as the control of temperature (97). The observation that temperature-sensitive neurons are present at many locations within the CNS suggests that a relatively simple temperature control system arose first and more complicated systems where added in parallel to the existing ones (97). Thus, different chemosensitive areas could reflect the transition from water to land, the development of homeothermy, the need for sleep, and the differentiation of sleep into REM and NREM types (51, 97).

Diseases associated with defects in CO_2/H^+ chemosensitivity

Abnormalities in CO_2/H^+ chemoreception have important clinical implications. For example, anatomical alterations in the human brainstem from infants who died of SIDS suggest a role of central chemoreceptors in this lethal disorder (97). In SIDS victims, neurons from the rostral ventrolateral medulla (rVLM) have been shown to exhibit decreased receptor binding and to be reduced in number compared to the non-SIDS normal rVLM region (74). CCHS, which is a rare developmental disease caused by mutations in the transcription factor Phox2b, is

characterized by a virtually complete loss of central respiratory chemoreception (56). Mutation of Phox2b has also been implicated in central sleep apnea (56), which is a common disorder that is considered a major public health burden (141). CCHS is often accompanied by central sleep apnea, as expected, but during active states (i.e., awake or exercise), chemoreflex responses do not appear to be altered (56). These examples highlight the importance in developing an understanding of the role of CRC in normal and disease states, as this will surely promote the advancement of the field and provide hope to those waiting for cures for these respiratory disorders.

Central respiratory chemoreceptors: definition and degree of chemosensitivity

CRC are a group of specialized cells that detect changes of chemical substances, similar to taste receptors, pain receptors, or avian intrapulmonary chemoreceptors (9). CRC detect changes in CO_2/ H^+ and alter ventilation through the respiratory network accordingly (40, 42). In this document, we use the term CRC for a neuron that meets the following three requirements based on the definition by Putnam and colleagues (110): 1) they have to respond either by an increase or decrease in their firing rate (FR) to changes of CO_2/ H^+; 2) they should be intrinsically responsive to changes of CO_2/H^+, meaning that the response is not due to synaptic stimulation by adjacent neurons; and 3) they have to alter ventilation, either directly or by projecting to intermediate respiratory neurons. Unfortunately, in mammals, no single neuron has been shown to meet all of these requirements (110). This could be mainly due to the fact that reduced preparations (where most of the experimental data are being generated) cannot be proven to be connected to respiratory centers *in vivo*. However, requirements 1 and 2 have been readily met in many neurons in multiple regions in the brainstem, and this has led to a tremendous advancement in the understanding of intrinsic CO_2/H^+ chemoreceptors.

As just mentioned, one important finding in mammals is the presence of multiple sites that meet the criteria for intrinsic chemosensitive neurons. There is a debate about whether they are present in discrete locations or, rather, are a continuum of neurons that exhibit different degrees of chemosensitivity. Currently there are two hypothesis: 1) the specialized chemoreceptor theory that envisions a small and specialized population of neurons in the brainstem capable of detecting small pH fluctuations and 2) the distributed chemosensitivity theory that argues that central chemoreception is a widespread response of brainstem neurons, including respiratory nuclei, to changes in pH that ultimately modulate the central response to changes in blood pH (56, 57). Evidence for the former has come from individuals with CCHS that lack almost entirely central chemosensitivity and yet breath relatively normally when awake or exercising. This indicates that CCHS patients must have a relatively intact respiratory CPG. Thus, central respiratory chemoreception cannot rely solely on the pH sensitivity of the CPG, but must also involve other neurons that activate the CPG

synaptically (56). Arguments in favor of the distributed chemoreception theory can be found in Nattie and colleagues and Richerson and colleagues among others (101, 118).

Even though it is widely accepted that there are many sites for central chemoreception and they are widespread along the brainstem (13, 71, 118), there is still debate, and some groups believe, that some of the candidate regions do not meet the criteria to be a CRC. Over the last two decades, the identification of sites has been the main contribution to the field, and it remains an active research area, but now the debate has moved towards identifying specific cellular phenotypes (38, 118, 137) and trying to elucidate the players for the transduction process from the signal to excitability response.

Traditionally, a change (increase/decrease) in the FR of a known respiratory-related group of neurons when exposed to HA has been used to quantify the degree of chemosensitivity of a region (3, 67, 85, 140). Another way to explore chemosensitivity is by measuring the ventilatory response of an anesthetized animal to local acidification (decrease in pH) in a respiratory-related region (as a percentage of the response of the whole animal breathing 9% CO_2) (39, 76, 145). In addition, three different ways of quantifying chemosensitivity are popular in the literature: 1) measurement of the slope of the absolute FR after changing pH_o; 2) measurement of the relative change in FR as percentage of the baseline FR in a control solution after a decrease in pH_o by a standard amount (e.g., 0.1 pH units); and 3) determination of the chemosensitivity index (CI) where a CI = 100% corresponds to no sensitivity and CI = 200% and CI = 50% correspond to double and half the original FR, respectively (116, 118). Relative changes in FR have been suggested to be more appropriate when comparing different regions (110).

Finally, the difficulty in identifying CRC has led to many alternative studies focusing on CO_2/H^+ sensing molecules instead of cells. In order to be considered a putative CO_2/H^+ sensing molecules, three requirements have to be met: 1) they have to be expressed in the brainstem; 2) they have to be sensitive to physiologic levels of CO_2; and 3) they have to couple CO_2 to membrane excitability (71).

Location of central respiratory chemoreceptors and their role

Putative central chemosensitive regions appear to be widespread in the brainstem, and include the ventrolateral medulla (VLM) (31, 115), retrotrapezoid nucleus (RTN) (85, 95-97, 99, 135), NTS (48, 93), locus coeruleus (LC) (46, 95), rostral aspect of the ventral respiratory group (rVRG) (116), pre-Bötzinger complex (129), and medullary raphé nuclei (118, 142) as well as the fastigal nucleus of the cerebellum (155) (see Figure 1.1 for neuroanatomical location of these sites). Experiments measuring changes in FR have revealed that in response to HA, approximately half of the neurons in the dorsal medulla, ventral medulla, and medullary raphé are excited and half are inhibited (110). In contrast, in the LC, >80% of neurons are stimulated by HA (110). Experiments have also

revealed that focal injections of acetazolamide (which produces focal tissue acidosis) increase ventilation (measured as phrenic nerve discharge) by 30% when applied in the LC, 34% when applied to the NTS, 20% when applied to the VLM including the RTN, and 32% when applied to the medullary raphé (110). Phrenic nerve discharge is also increased in response to focal CO_2 applied to the midline caudal medullary raphé and pre-Bötzinger complex (110). It is interesting to note that in all of these regions, a different response is seen when the CI is used to quantify the response to HA. Table 1.1 shows that the RTN has the strongest response overall, but interestingly, none of these regions account for the response of the system as a whole.

Specific chemosensitive sites and their roles remain to be elucidated, but it is known that many of these chemosensitive regions participate in other homeostatic functions, and their contribution to respiration has been found to be state dependent. For example, in an unanesthetized rat model, acidification of the RTN was shown to increase ventilation by 24% during the awake state, but not during sleep, and this increase was mediated by a change exclusively in tidal volume (97). In the same experiment, the medullary raphé was found to be silent in response to hypercapnia during the awake state but active during sleep. The medullary raphé has been suggested to participate in arousal, thermoregulation, nociception, and respiration. Finally, the NTS was found to be active while both asleep and awake. The authors of these studies concluded that these findings support the development of CO_2/H^+ control system in a step-wise fashion in parallel with the evolution of sleep.

Signals in central chemoreception

In theory, the sensory components underlying ventilatory control could be responding to changes of O_2, CO_2, pH, and/or HCO_3^-. In the following, we explore each of these species in more detail.

CO_2: The main arguments for a role of CO_2 are the large ventilatory response elicited by HA compared to that evoked by metabolic acidosis and its known function in other chemoreceptors (60). Nevertheless, all of the theories that have suggested CO_2 as a possible signal fail to identify this molecule as an exclusive signal because increased levels of in CO_2 (i.e., HA) are always associated with a fall in pH_o and pH_i (61-63, 86, 110); thus, CO_2 alone cannot explain the response to HA. The idea of a CO_2 sensor, however, cannot be ruled out because recent findings show that molecular CO_2 activates L-type Ca^{++} channels in glomus cells independently of its effects on pH_i and pH_o (131).

HCO_3^-: The role of HCO_3^- is not well understood because of its strong relation with pH. Nevertheless, HCO_3^- has been shown to activate adenyl cyclase and promote activation of cAMP which opens L-type Ca^{++} channels (131). In addition, activation of $GABA_A$ channels, that are permeable to Cl^- and HCO_3^- (110), results in an efflux of HCO_3^-, and therefore produces acidification of the intracellular compartment and alkalinization of the extracellular space. Finally, aside from the

role of HCO_3^- acting as a weak base in pH regulation, most neurons express an AE that exchanges Cl^- for HCO_3^-. The AE is HCO_3^- dependent, and its effect is independent of the direct effects of HCO_3^- on pH. For these reasons, we think that a careful examination of the role of HCO_3^- in the ventilatory response to HA and other acid-base disturbances is warranted.

pH_o and pH_i : Early experiments attempted to differentiate between the effects of pH_i and pH_o on the ventilatory response by comparing the effects elicited by HA (increase in CO_2 at constant HCO_3^-) to those produced by metabolic acidosis (MA) (a decrease in pH_i and pH_o without changes in CO_2). Although both HA and MA elicit increases in ventilation, the ventilatory response to MA is less robust. This observation suggests that pH_i and pH_o, which are altered in both of these acid-base disturbances, may play a role in the ventilatory response (77); however, since CO_2 is unchanged in MA, a role for CO_2 is less clear. Further, since these experiments provided no information regarding the rate of change or the magnitude of change in pH_i and pH_o during HA or MA, the true contributions of these signals to ventilation is difficult to quantify. It is also unclear how one could delineate the precise effects of pH_i versus those of pH_o based on these experiments. Regardless, the observations from this series of experiments suggests that pH_i and pH_o may both contribute to the CO_2/H^+ chemosensitive response albeit the precise contributions of these signaling molecules remains to be quantified. To date, however, there are no techniques available to clamp pH_i in order to identify and quantify its contribution to the ventilatory response.

Accumulating evidence, however, suggests that pH_i may be the primary stimulus for the CO_2/H^+ chemosensitive response. It has been shown that when brain surface CO_2 is maintained constant, the addition of acetazolamide (a CA inhibitor) decreases pH_o to the same extent as that caused by HA (but with no significant fall in pH_i), but does not significantly alter in ventilation (15). This result suggests that pH_o does not participate in the CO_2/H^+ response, and that pH_i must play a role; this observation, however, is not wholly consistent with those of previous experiments (139). Further, isohydric hypercapnia (IH) produced by an increase in CO_2 and an elevated HCO_3^- so that constant pH_o is maintained, isocapnic acidosis (IA) produced by a decrease in HCO_3^- that causes a decrease in pH_i and pH_o with constant CO_2, and acidified HEPES buffer which reduces only the pH_i-pH_o gradient with no change in CO_2 all increase ventilation (140), suggesting a role for pH_i. In addition, a significant correlation between pH_i and FR but not between pH_i-pH_o gradient and FR has been reported (121). Taken together, these observations further support the idea that pH_i may be the primary stimulus for chemosensitive neurons.

All of the above experiments suggest pH_i is the main signal in central CO_2/H^+ chemoreception. Unfortunately, there is also evidence against pH_i as the primary stimulus. The main observation is the so-called hypoxia paradox, where hypoxia-induced intracellular acidification of the brainstem (to the same extent seen with HA) does not stimulate ventilation. An increase in ventilation, however, can be obtained during an anoxic challenge if pH_i is decreased with hypercapnia (110).

Furthermore, during hypoxia-induced acidification, chemosensitive NTS and VLM neurons acidify and remain acidified to the same extent as during HA, but they show no FR response (110). While these findings suggest that pH_i does not appear to participate in the CO_2/H^+ response, they do provide support to the idea that CO_2 must have a role.

Other signals that have been proposed to be involved in central CO_2/H^+ chemosensitivity are Ca^{++} (110), gap junctions (128), CA (102), and glia (14), all of which participate either in cell excitability or pH regulation, both crucial aspects in CO_2/H^+ chemoreception.

Type of response to HA

Experiments measuring pH_i using the pH-sensitive dye BCECF have revealed that neurons from putative chemosensitive areas of the medulla (VLM and NTS) acidify and remain acidic during exposure to HA. In contrast, neurons from non-chemosensitive areas (inferior olive (IO) and hypoglossal motor nuclues (Hyp)) show pH_i recovery from acidification during the acid exposure (121). However, there appears to be a developmental shift in the pH_i response to HA in neurons from non-chemosensitive areas, such that they lack pH_i recovery when studied in older animals (>P15) (104), suggesting that this response may not be unique to chemosensitive neurons. In addition, results from experiments conducted in the brainstem of the invertebrate *Helix aspersa* suggest that identification of neurons as chemosensitive based on pH_i regulatory profiles is not ideal as this appears to be an insensitive marker of chemosensitivity (53). Specificity to the species studied remains to be explored.

Based on previous observations and the proposed definition of a CRC, we can postulate that there are two main responses of a chemosensitive neuron to HA: 1) during HA, they do not regulate pH_i and 2) during HA, they increase or decrease FR (excitation or inhibition) (53, 121). These characteristics are necessary but not sufficient to define a neuron as a chemoreceptor. However, widespread poor pH_i regulation in brainstem neurons regardless of their excitability makes this issue an important study topic (19, 121, 146).

From a theoretical perspective, one would expect that if pH_i is an important signal in CO_2/H^+ chemoreception, then chemosensitive neurons would regulate pH_i differently. As such, one or more of the following mechanisms would be expected to be different between chemosensitive and non-chemosensitive neurons: 1) intrinsic buffering capacity (β_{int}), 2) the ability of pH_i to closely track pH_o, and 3) the lack or inhibition of pH_i regulating mechanisms during acid/base disturbances (124). As a result, experiments searching for evidence of cellular differences between chemosensitive and non-chemosensitive neurons has become popular. The initial evidence supporting a difference between chemosensitive and non-chemosensitive neurons comes from studies demonstrating that different acid-base perturbations elicit different pH_i regulatory responses in chemosensitive neurons (RTN and VLM) and non-chemosensitive

neurons (IO and Hyp). These experiments have shown that: 1) β_{int} is the same in neurons from chemosensitive and non-chemosensitive areas of the medulla (using an ammonium prepulse experiment); 2) the pH_o-pH_i relationship has a steeper slope in chemosensitive neurons than in non-chemosensitive neurons (for a given change in pH_o, pH_i in chemosensitive neurons changes to a greater degree); and 3) the removal of extracellular Cl^- at steady-state pH results in intracellular alkalinization in all Hyp, IO, and VLM neurons, but results in acidification in NTS neurons. This suggests that the AE is present in Hyp, IO, and VLM neurons but not in NTS neurons (121).

One interesting finding is the steeper pH_o-pH_i relationship in chemosensitive neurons, partially due to the fact that they do not recover from alkalinization. In NTS neurons, it is possible to explain this by the fact that they do not have the AE. VLM neurons, on the other hand, have an AE; thus, a possible explanation of why they do not recover may be related to the sensitivity of the AE to pH_o. Another possibility is that this behavior is mediated by an acidifying HCO_3^- efflux through a channel that has not yet been described (121).

It has also been proposed that the chemosensitive signal could be initiated in the dendrites as opposed to the soma. Experiments that induced HA (15% CO_2) that resulted in similar acidification of dendrites and soma showed that acidification was faster in the more distal regions of the dendrite (123). Neither the dendrites nor the soma exhibited pH_i recovery during HA, but both regions contained the pH_i regulating mechanisms because they both show recovery under an ammonium prepulse (123). Exposing only the dendrite to HA does not increase the FR but exposing only the soma does increase the FR to near maximum. Therefore, there appear to be no spatial differences in the pH_i response to HA when ones moves from the soma to the more distal dendrites, but activation of the neuron requires somatic exposure to acidosis (123).

Regulation of intracellular pH

The regulation of pH_i is accomplished, in part, by an array of cellular transporters, such as the Na^+/H^+ exchanger (NHE), Cl^-/HCO_3^+ exchanger (AE), the Na^+ driven Cl^-/HCO_3^- exchanger, and the Na^+-HCO_3^- cotransporter, which work as acid loaders or acid extruders (21, 26). The exact contribution of each one of these transporters to pH homeostasis is not known, but a lot can be learned from the chemosensitivity experiments. Also, important for pH_i regulation is buffering capacity of the cell. In general cells have many buffer systems like the CO_2/HCO_3^-, which accounts for 1/3 to 2/3 of the total buffering power (78), or the ammonium buffer pair (NH_4^+/NH_3) and inorganic phosphate ($H_2PO_4^-/HPO_4^=$). Proteins also have the ability to reversibly bind or release protons, thereby increasing the buffering power of the cell (16, 17, 126). The final total buffering capacity of a cell is the sum of all individual buffer pairs.

The reversible hydration of CO_2 is perhaps the most pertinent reaction for respiratory control in animals. Other reactions include formation of carbamates

and formation of HCO_3^- from the reaction of CO_2 and hydroxyl and others buffers might play significant roles under other conditions. The production of H^+ by CO_2 is represented by:

$$CO_2 + H_2O \xleftrightarrow{k_h / k_d} H_2CO_3 \xleftrightarrow{k_{+1} / k_{-1}} HCO_3^- + H^+ \tag{1.1}$$

where k_h and k_d are hydration and dehydration rate constants in s^{-1}. At 37 ^oC in physiological saline, k_h = 0.18 s^{-1} and k_d = 64 s^{-1} (68). k_{+1} and k_{-1} are rate constants for ionization and protonation of carbonic acid. k_{+1} = 4.7x10^{10} $M^{-1}s^{-1}$ and k_{-1} = 8x10^6 s^{-1} (68). The second reaction is so fast at physiological time scales that it can be always be considered to be in equilibrium

$$\frac{k_{+1}}{k_{-1}} = \frac{C_{H^+} C_{HCO_3^-}}{C_{H_2CO_3}} = K' \tag{1.2}$$

and if we apply this scheme for the whole reaction at equilibrium, we get

$$K' = \frac{C_{H^+} C_{HCO_3^-}}{C_{CO_2}} \tag{1.3}$$

where K' is the equilibrium constant for the two reactions shown in equation 1.1. Doing the same analysis for the hydration/dehydration reaction, we get:

$$\frac{C_{H_2CO_3}}{C_{CO_2}} = \frac{k_h}{k_d} \tag{1.4}$$

and substituting equations 1.4 into 1.2 yields the Henderson-Hasselbalch equation, that allows for prediction of changes in pH when CO_2 is varied:

$$pH = pK + \log \frac{C_{HCO_3^-}}{C_{CO_2}} \tag{1.5}$$

where $K = K'kh / kd$. The instantaneous rate of change of CO_2 in equation 1.1 at a constant pH is very fast with a half-time of 3.7 s, demonstrating that the uncatalized reaction of CO_2 is very fast at physiological conditions (80). Carbonic anhydrase (CA) can increase the speed of the reaction by 1000 fold at 37 ^oC and it is present in brain tissue (80).

If one wants to incorporate the effects of proteins and another elements that affect the buffering capacity of the cell, a simple approach would be to define the rate of change of protons (dQ) in a single buffer system as the difference between the ionization of the weak acid (HA) and the protonation of the weak base (A). Then taking equation 1.1 where HA is carbonic acid and bicarbonate is A, then dQ/dt might look like

$$\frac{dQ}{dt} = \rho((1-\alpha)J_{HA} - \alpha J_A) \tag{1.6}$$

where α=$C_{H^+} / (C_{H^+} + K)$, and ρ is the area to volume ratio, t is time and J_{HA} and

J_A are the fluxes of the weak acid and weak base, respectively, defined by the proper model. If the intrinsic buffering capacity is defined by the rate of change of proton divided by the rate of change of pH, then the rate of change of H^+ can be expressed by:

$$\frac{dC_{H^+}}{dt} = \frac{-2.3C_{H^+}}{\beta} dQ \tag{1.7}$$

where β is the intrinsic buffering capacity [mM] and dQ is defined by equation 1.6.

The system of equations 1.1 to 1.7 show that a mathematical model of pH regulation can be constructed where the effects of different variables can be tested so a quantitative understanding of the dynamics of pH_i can be obtained. A similar model for pH_i regulation is implemented in this document, but we defer the details for future chapters where the pertinence of these expressions is more apparent. Here, we present only these ideas as general background and for contextualization.

The ubiquitous lack of pH_i regulation in respiratory centers in the brainstem raises a question: What are the differences in these brainstem neurons that impede them from regulating pH_i? The answer has to be that the β_{int} is different and/or that the pH_i regulating mechanisms (the acid loaders and extruders) are different or not present. There is some evidence, though, that the β_{int} is the same in chemosensitive and non-chemosensitive neurons (121). As far as the transporters, most of the studies have postulated that NHE would be the perfect candidate for explaining differences in pH_i regulation, since the isoform 1 (NHE1) is ubiquitous in the body and is perhaps the most important acid recovery mechanism. The presence of another NHE isoform with different kinetics is a very appealing solution to the pH_i regulation puzzle. Ritucci and colleagues (121) provided evidence that chemosensitive neurons from the NTS and VLM have an NHE that is far more sensitive to changes in pH_o (inhibited at pH ~7) than that found in non-chemosensitive neurons from the IO and Hyp (where it was inhibited ~6.7), supporting the idea that a different NHE isoform (in particular NHE3) could possibly explain the the difference in pH_i regulation during HA between CO_2 chemosensitive and non-chemosensitive cells. On the other hand, the AE, which is very important for recovery from alkalinization, has been less well studied and could play an important role in pH_i regulation during HA. In the same experiments, the researchers found that the AE was not present in NTS neurons, but the observation was not conclusive for all chemosensitive neurons since VLM cells do have the AE.

Signal transduction

Experimental data suggest a few candidates as the cellular targets that translate the signal into changes in FR. The most common are the TASK channels (25), L-type Ca^{++} channel (25), and TEA-sensitive K^+ channels (25).

Also, ATP levels have been linked to the chemosensitive response (136). They are all pH sensitive, but the change in pH_i has to be persistent to stimulate the channels and elicit a change in FR (110). That is why we postulate that the lack of pH_i recovery is a fundamental element in the response to HA. A chemosensitive neuron would then have the ability to closely track pH_o by means of maintaining a reduced pH_i as long as the stimulus lasts (i.e., increase in CO_2).

Inward rectifier K^+ channels (K_{ir}) help set resting membrane potential and control interspike duration thereby affecting cell excitability. The pH-sensitive K_{ir} channels are composed by four families: $K_{ir}1$, $K_{ir}2$, $K_{ir}4$, and $K_{ir}5$, and it is believed that pH exerts effects on the configuration of the channel (110). There is also evidence that pH_i inhibits large conductance (BK) and small conductance (SK) Ca^{++}-gated K^+ channels (IK_{Ca}) (27). Inhibition of IK_{Ca} channels depolarizes the cell and increases excitability, suggesting that IK_{Ca} channels may participate in central CO_2/H^+ chemoreception. Another candidate for signal transduction in chemosensitive neurons are the voltage-sensitive K^+ channels, which includes the fast inactivating A-type K^+ (K_A) current and the delayed rectifier K_{DR} current. The proven sensitivity of these channels to both pH_i and pH_o makes them possible signal molecules (12). These channels affect the shape of the action potential (AP), in particular during the repolarization phase, giving them the ability to modulate spike frequency by changes in rates of repolarization. Another candidate is the TWIK family, which is a group of K^+ channels that are voltage-insensitive and generate a “leak” current that contributes to resting membrane potential, excitability, and AP duration. Inside the TWIK family, there is an acid-sensitive group known as the TASK channels that are expressed in the brain and are unaffected by pH_i but are inhibited by a decrease in pH_o (8). Finally Ca^{++} channels are common candidates since typically HA results in increase of intracellular Ca^{++}. It has been suggested that activation of the L-type Ca^{++} channel during HA in chemosensitive neurons occurs via an indirect pathway that involves activation of cAMP by adenyl cyclase, due to an increase in HCO_3^- during HA. (110)

1.3 Description of the study

Up to this point, we have presented a brief summary of what is known about central CO_2/H^+ chemoreception. More importantly, we have briefly noted many of the existing controversies and the lack of understanding of important points that certainly contribute to respiratory control. We want to reiterate here some of these issues and introduce our approach to study them, with the hope of helping advance the field and contribute to the current debate.

The signal in CO_2/H^+ chemoreception seems to be a matter of much debate. We stated that while pH_i seems to be the strongest candidate, it does not always produces an increase in ventilation. Other variables seem to play a role or, at least, be connected to changes in pH_i and as such, cannot be totally taken out of the equation. These signals include pH_o, CO_2, and HCO_3^+. A detailed model of pH_i regulation would be a powerful tool to asses the effects of variables like β_{int},

permeability of weak acids and bases, and the expression of acid/base regulation mechanisms. Chapter 2 introduces a cell-level mathematical model that was developed to answer some of these questions, and it is validated by comparing simulations of HA, IH, and an ammonium prepulse to experimental data in a qualitative manner.

We also mentioned that even though blunted pH_i regulation during HA may not be a sensitive marker for chemosensitive neurons, it is a widespread response in respiratory areas of the brainstem, and therefore has been a matter of much debate. It was postulated that chemosensitive neurons lack pH_i regulatory mechanisms, but it turns out that they do have "house keeping" machinery for pH_i regulation (73). Therefore, to achieve the delicate balance between acid extrusion and acid loading, they must have different pH_i regulatory elements. In chapter 3, we explore the effects of different NHE isoforms on pH_i regulation using our mathematical model developed in chapter 2. We also validate the model by comparing the response to HA and IH of neurons from different chemosensitive regions were some cellular level information regarding differences in pH_i regulation is available in the literature.

In chapter 4, we explore the link between cell excitability and pH in chemosensitive and non-chemosensitive neurons by adjusting our pH model to include action potential capabilities. Rather than assuming targets (i.e., pH-sensitive currents), we wanted to first to test the effects that HA can have on cell excitability via changes in the Nernst equilibrium potential of the ions. We consider this to be a preliminary step since signal transduction can be achieved by many different processes, and also because of the observation that pH_i does not always correlate with changes in FR. In particular, lack of correlation is observed during the recovery process (after the acid challenge) or when pH_i recovers in chemosensitive neurons (like during IH) (110), suggesting that pH-sensitive currents might not be enough to explain changes in excitability in chemosensitive neurons.

Finally, in chapter 5, we list some of the multiple issues that we consider important to validate in future experiments/simulations and suggest possible experimental set-ups to answer some of the hypotheses that we present throughout the document. An appendix is provided at the end for easy reference to mathematical equations, assumptions, model parameters, and units employed in our model and simulations.

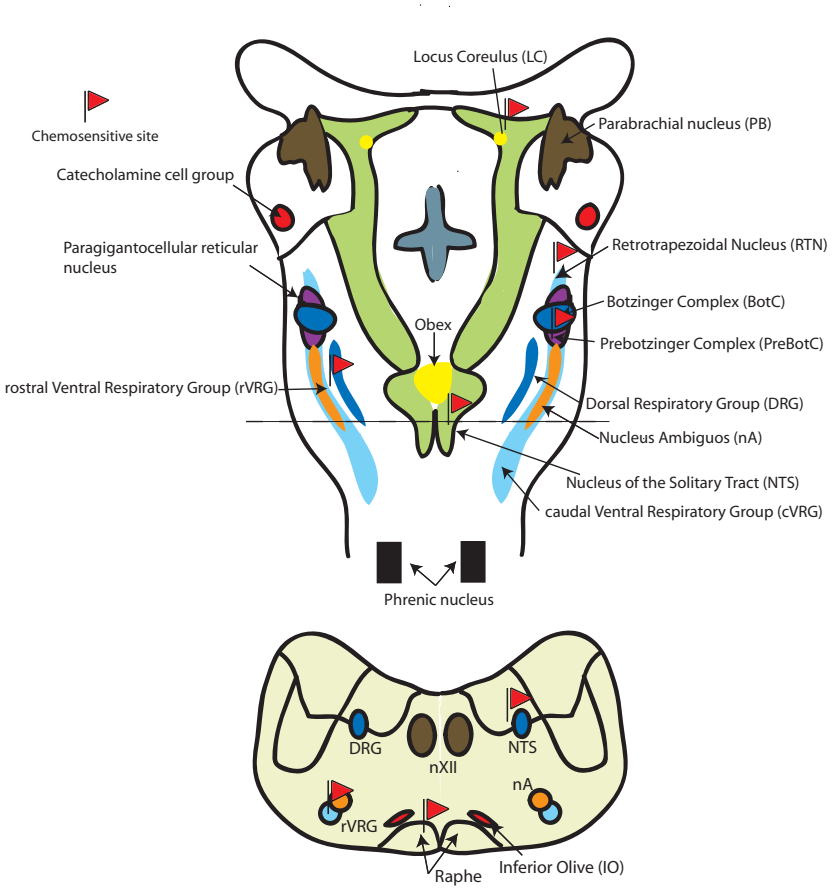

Figure 1.1. Respiratory neuroanatomy of the rat brainstem.

Main chemoreceptors sites and their locations in the rat brainstem. Adapted from Feldman(1988) and Duffin (2005).

Table 1.1 Chemosensitivity Index (CI) of some regions in the brainstem.

Region	CI
RTN	300
Medullary Raphé	250
VLM	150
NTS	140
LC	125

Chapter 2 - Development of a transport model to study pH regulation

2.1 Introduction

Central chemosensitivity is critical for appropriate control of breathing in reptiles, birds and mammals, and some evidence suggests that also air breathing fishes have central control of breathing (92). Central chemoreceptors have functions that range from breathing, rhythm generation, cardiovascular control, swallowing, eating, taste, and the arousal response to body homeostasis (45). Central chemoreceptors are also known as CO_2/H^+ chemoreceptors to reflect the fact that they respond to increased levels of CO_2 (that ultimately exert the strongest effect on ventilation) and also to acidic conditions (low pH), but the signal, whether it is CO_2 itself or any of the molecules derived from the reaction of CO_2 and water that happens virtually in every single cell, is unknown.

Not surprisingly, all animals cells that have been examined, aside from non-nucleated erythrocytes, regulate intracellular pH (pH_i). pH_i regulation is extremely important for cell homeostasis as pH dictates the ionization state of weak acids including proteins (17, 18). Another exception to the common, vigorous pH_i regulation by most cells is central CO_2/H^+ chemoreceptors. As opposed to the vast majority of cells, CO_2/H^+ chemoreceptors do not actively regulate pH_i during hypercapnic acidosis (HA) -an increase in CO_2 that causes a decrease in pH_i and extracellular pH (pH_o). Nevertheless, they do show pH_i regulation during isohydric hypercapnia (IH) - a concurrent increase in CO_2 and bicarbonate in the extracellular compartment that leads to a decrease in pH_i but not pH_o. This suggests that these chemosensitive neurons do have pH regulation mechanisms but are “sensing” a “signal” that is eventually translated into a change in ventilation (121).

Therefore, almost all of the molecules involved in the reaction of CO_2 with water and the pH related species have been proposed as the necessary and sufficient stimuli to increase ventilation during respiratory acidosis (110). Despite tremendous scientific effort, however, no single molecule seems to meet the requirements to be named as the primary signal of the CO_2/H^+ chemoreceptor response. For example, HA elicits a strong ventilatory response, suggesting that CO_2, pH_i, and pH_o are all possible signals while IH, which also increases ventilation, suggests that CO_2 and pH_i but not pH_o may be the signals. Metabolic (isocapnic) acidosis, which results in decreased pH_i and pH_o without changes in CO_2, also alters ventilation, suggesting that pH_i and pH_o but not CO_2 may act as the signals. Based on these observations, pH_i has been proposed to be the primary stimulus; however, hypoxia-induced acidification (to the same extent of HA) does not stimulate ventilation, suggesting that pH_i alone is not sufficient. Thus, the precise role of these candidate signals in central CO_2/H^+ chemoreception and the processes by which these signals are transduced (translated) into changes in firing rate (FR) remain unclear.

To complicate things even further, pH_i regulation of medullary neurons during HA seems to be tied to development. In young neonatal rats, neurons from chemosensitive regions, such as the solitary complex (nucleus tractus solitarius and dorsal vagal motor nuclei) and retrotrapezoidal nucleus (RTN), acidify in response to HA (10% CO_2) and stay acidic (without recovery) for the duration of the insult while neurons from non-chemosensitive regions (i.e., hypoglossal motor nuclei, inferior olivary nuclei) show pH_i recovery when subjected to the same acid challenge (104, 121). In contrast, in adult rats, neurons from non-chemosensitive regions show no pH_i regulation (104), suggesting that the lack of pH_i recovery during HA may be a common response of neurons in respiratory-related medullary regions in the adult rat brainstem. Whether a similar loss of pH_i regulation occurs developmentally in other species remains to be explored. Regardless, the lack of pH_i recovery during HA is proposed to be part of the mechanism by which chemosensitive cells sense changes in CO_2/H^+ (19, 71, 124). After all, if pH_i is the signal for CO_2/H^+ chemosensitivity, it makes sense from a theoretical perspective that the signal is maintained as long as the sensed molecule is present.

Exposure to CO_2, NH_4^+, and inhibition of acid-base regulation mechanisms causes a change in pH_i. In order to achieve a quantitative understanding of the events underlying the changes in pH_i, we developed a mathematical model. The model is designed to evaluate the role of different cellular mechanisms proposed to participate in pH_i regulation during HA and other acid-base challenges, and to set the foundation for a molecular explanation responsible for the differences in pH_i regulation in CO_2/H^+ chemosensitive and non-chemosensitive neonatal rat neurons. The model is a single compartment model that takes into account simultaneous passive fluxes of major ion species across the cell membrane, and it includes conjugate pairs of three different buffers. Several parameters, including the dissociation constants, permeability of the membrane to the ions considered, and activity of transport mechanisms were balanced and used in calculating the net fluxes of the chemical species. The model incorporates a voltage-sensitive description of the Na^+-K^+-ATPase that compensate for the differences in permeabilities for these ions (differences that set the cell's membrane potential). In addition, the model includes Cl^- sensitive cotransporters that help maintain cell volume, the sodium-potassium-chloride cotransporter (NKCC) and the potassium-chloride cotransporter (KCC). Finally, the model contains an acid-base regulation component that includes an acid loader, the chloride-bicarbonate exchanger or anion exchanger (AE), and an acid extruder, the sodium hydrogen exchanger (NHE). A complete description of the model can be found in Appendix A.

Based on previous observations and following a common assumption in modelling of transport phenomena, we decided to use the Goldman-Hodgkin-Katz (GHK) equation (28, 52, 65) for the description of ionic fluxes. Other options for transport models include those based on ionic conductance, where the amount of current carried by an ion is given by $I = g(V - E)$ where g is ionic

conductance (mS), *V* is membrane potential (mV) and *E* is the reversal potential for the ion (mV). However, two disadvantages to the later approach are that: 1) ion flow generally does *not* adhere to the linear *I-V* relation implied by the equation describing ionic current when the difference between the intracellular and extracellular concentrations is large and 2) conductance is proportional to permeability, but it is also a function of membrane potential and the intracellular and extracellular ion concentrations. For a comparison of a conductance-based model and a permeability-based model, see Cordovez et al., 2008 (34).

Two experimental perturbations of acid-base regulation mechanisms that are commonly used include HA and an ammonium (NH_4^+) prepulse (which consists of a short duration, large magnitude increase in C^o_{NH4}). These perturbations evoke responses of cellular homeostatic systems involved in the movement of ions across the cell membrane, causing not only a significant change in ion concentration but also changes in cell volume. In our initial studies using our model, we noticed significant changes in cell volume during simulated HA and NH_4^+ prepulse experiments. We therefore decided to include a component for cell volume regulation. This part of the model was carefully tuned (details can be found in Appendix A) so that reasonable levels of compensation would be achieved for the necessary elements. Some of the figures in this manuscript demonstrate the results of our simulations with and without volume regulation in order to provide a better understanding of the effects of these model components on state variables and overall dynamics.

From the initial simulations using the model, we also noticed that an instantaneous change in the measured variables was produced by a change of the parameters. For example, upon exposure to increased levels of CO_2, we noticed an immediate drop in pH_i (i.e., a step response) rather than a smooth transition. In order to reconcile the model output with experimental data, we added a differential equation to reflect the presence of a 10-second (time constant) diffusion delay, which corresponds to a 150 µm unstirred layer for diffusion. The differential equation used to incorporate this delay into the model is included in Appendix C. Figure 2.1 shows a HA simulation with and without the diffusion delay to illustrate this point; all other figures in the document were generated using the delay. The most dramatic change observed by incorporating the delay can be seen in the pH_i trace where the fast permeation of CO_2 cause an “instantaneous” drop in pH_i when no delay is considered while the model with delay allows for a smooth response that better resembles experimental recordings.

2.2 Methods

The model incorporates conservation of mass and electroneutrality constraints, kinetic models of the Na^+/K^+-ATPase, anion exchanger (AE), sodium-hydrogen exchanger (NHE), sodium-potassium-chloride cotransporter (NKCC), potassium-chloride cotransporter (KCC), passive permeation pathways for solute

species and water, and hydration/dehydration rates for CO_2 catalysed by carbonic anhydrase (CA). The elements of the model are shown in Figure 2.2 and the mathematical description of the state equations and membrane transport mechanisms can be found in Appendix A and Appendix B. The numerical methods employed to find the membrane potential, integrate the state variables and compute the concentration of H^+ are described in Appendix C.

2.3 Results

Model behavior

Table 2.2 shows the steady-state values of the state variables, intracellular concentrations, volume, and membrane potential, after solving the equations numerically using the parameters listed in Table 2.1. Figure 2.3 shows the fluxes for each of the ions and membrane transporters also at steady-state. Note that the water flux is equal to zero, indicating that the model achieves steady-state in terms of osmolarity (300 mOsm in both the intracellular and extracellular compartments) and electroneutrality. The permeability of K^+ is set to be 20 times higher than the permeability of Na^+, and the permeability for Na^+ is set to be 20 times higher than the permeability of Cl^-. This set of values along with the intracellular and extracellular concentrations gives a resting membrane potential of –65 mV, which is reasonable for neurons in the respiratory regions of the brainstem (132).

Although, NH_4^+/NH_3 are not believed to be physiologically relevant in these neurons, we included a very high P_{NH3} coupled with a P_{NH4} comparable to P_K in the model. This configuration allows for simulation of the NH_4^+ prepulse experiment and accommodates the observations that NH_4^+ can cross the membrane through K^+ channels (18) and that the permeability of NH_3, which is a gas, is very high.

Cell volume regulation

Figures 2.4, 2.5, and 2.6 show the results of simulation experiments corresponding to HA, NH_4^+ prepulse, and IH, respectively, with (panel A) and without (panel B) volume regulation. Implementation of volume regulation mechanisms results in small changes in cell volume, which are at the expense of larger changes in ion concentrations and membrane potential. A minimal change in the pH_i response is observed when the model incorporates volume regulation, indicating that pH_i regulation is not very sensitive to the activities of the NKCC and KCC with the acid-base challenges tested.

Response of the model to simulated Hypercapnic Acidosis

Hypercapnia is the natural respiratory stimulus to which chemosensitive neurons respond. Increased levels of CO_2, which typically lead to a rapid drop in pH_i in all cells is captured by the model. The speed of the reaction depends on the presence of CA, and the formation of H^+ and HCO_3^-. Increased levels of CO_2 result in a fall in both pH_i and pH_o, but most cells partially offset the drop in pH_i by

intracellular buffering capacity and transmembrane extrusion of H^+. The typical mechanisms that help cells recover from acid disturbances are the NHE and the sodium-driven chloride-bicarbonate exchanger (NDCBE) (14).

Figure 2.4 shows the time course of the response to simulated HA using our model. The simulation starts with a short baseline followed by an increase in CO_2 from 40 mmHg to 80 mmHg for 400 s, and then the system is returned to normocapnic conditions. As soon as the CO_2 concentration rises, there is a chemical flux of carbonic acid, caused by the freely permeable CO_2; this increases intracellular HCO_3^- and H^+, resulting in a drop in pH_i. The rate of pH_i drop is maximum at the beginning of the CO_2 challenge, and then it decreases as the concentration of carbonic acid increases and the hydration of CO_2 slows; this rate is affected primarily by the presence of CA. After the initial drop in pH_i, a fast recovery that eventually plateaus (approximately after around 5 minutes) is observed, and a new state is reached at a lower pH_i (the bigger the increase in CO_2 the lower the pH_i at which the response plateaus). This response is the consequence of a delicate balance between the addition and extrusion of protons (H^+). In the model, protons are generated during HA only by the hydration of CO_2, but extrusion is the result of two components: 1) the activity of the NHE (which also extrudes NH_4^+ generated by the consumption of NH_3 and H^+ due to competitive binding for the intracellular site) and 2) buffering of H^+ by phosphate. Indirectly, however, HCO_3^- is moved out of the cell through the AE exchanger in exchange for Cl^-; this is the only pathway for HCO_3^- extrusion since $P_{HCO3} = 0$. Bicarbonate accumulation (i.e., inhibition of the AE) compromises pH_i recovery via slowing down the conversion of CO_2 into H_2CO_3. Changes of these elements could lead to impaired fluxes through the NHE and to blunted pH_i regulation. Reducing the activity of the NHE causes the slope of the pH_i recovery to diminish or to become negative depending of the level of inhibition (not shown in Figure 2.3). Removing the acid load causes an alkalotic overshoot followed by acidification and recovery to steady-state baseline pH_i. The alkalotic overshoot is the result of the increased NHE activity that upon CO_2 removal, causes a fast increase in pH_i; the recovery to baseline is mediated by the AE.

Response of the model to simulated ammonium prepulse:

Exposure to ammonia is a good method to first alkalize and then reversibly acidify cells (146). It provides the means for testing experimentally the effects on pH_i in the chemosensitive response independently of those caused by CO_2, and the basic response to the NH_4^+ prepulse stimulus consists of three phases: intracellular alkalinization, intracellular acidification, and pH_i recovery. The mechanism proposed for the alkalinization process appear to be related to the rapid influx of the neutral NH_3, which then binds to H^+ in the cell to induce intracellular alkalosis that is partially offset by the slow influx of NH_4^+ that appears be dependent on potassium channels, as reported in the kidney (75); this slow influx of NH_4^+ leads to the slight acidification that is seen at the peak of the NH_4^+ prepulse stimulus. With removal of the stimulus, a rapid intracellular acidification occurs due to accumulation of protons since NH_4^+ is converted back to NH_3 (by

giving off a H^+), which rapidly leaves the cell. This acidification results in an overshoot of the baseline pH_i due to acid-base regulatory mechanisms (146), which along with intracellular buffering capacity are also responsible for the subsequent recovery phase. If NH_4^+ is highly permeable, the initial alkalinization tends to disappear (16). We wanted to test whether our model can reproduce the NH_4^+ prepulse experiment.

Figure 2.5 shows the time course of the response to a simulated NH_4^+ prepulse. The simulation starts with a short baseline followed by an increase in extracellular NH_4^+ from 0.01 to 39 mM during 100 s, and then the system is returned to the normal extracellular NH_4^+ concentration. We found that adding NH_4^+ and subsequently removing it resulted in a rapid rise in pH_i followed by an acidification. The initial rise in pH_i was mediated by an instantaneous influx of NH_3 that followed the increase in extracellular NH_4^+ (prepulse stimulus) in a manner similar to that previously reported in *in vitro* experiments. In the model, this rapid influx of base that caused the pH_i to rise was compensated by the reversal of the NHE, which started pumping H^+ inside the cell using the NH_4^+ gradient in exchange for Na^+ against its concentration gradient, and the AE that removes HCO_3^- (formed due to the change in pH) from the intracellular compartment. With removal of the NH_4^+ prepulse stimulus, a further acidification was observed. This acidification was caused by the rapid efflux of NH_3, which was followed by pH_i recovery mediated by the NHE. After 600 s, pH_i returned to baseline conditions.

Not shown in Figure 2.5 is the interesting fact that when pH_i recovery starts after removal of extracellular NH_4^+, inhibition of the NHE (simulating amiloride effect) halts the recovery phase completely and exacerbates the acidification; removing the inhibition restores the pH_i recovery process. In the model, inhibition of the NHE impairs the ability of the cell to recover from acidification because there are no other mechanisms for H^+ extrusion and the balance between addition and removal of protons becomes altered. This has been observed in experiments, and an imbalance of acid extrusion/loading has been proposed (126).

Response of the model to simulated isohydric hypercapnia

Increased levels of CO_2 at a constant pH_o is an experimental tool used to explore the cellular mechanisms responsible for pH_i regulation. The decreased pH_i, relative to the normal pH_o, generates a steeper pH gradient across the cell membrane compared to one generated during HA. It has been suggested that it is the gradient rather than the decrease in pH_i alone, that is responsible for different responses to acid load observed in respiratory neurons from the ventrolateral medulla (110).

Figure 2.6 shows the time course of the response to simulated IH. The simulation starts with a short baseline followed by and increase in CO_2 from 40 mmHg to 80 mmHg for 400 s with a simultaneous increase in extracellular HCO_3^- from 24 to 48 mM; thus, pH_o remains unchanged during the CO_2 challenge. The

system is then returned to normocapnic conditions and the bicarbonate level reduced to normal. We observed that IH leads to a decrease in pH_i that is partially offset by intracellular buffering capacity and transmembrane extrusion of H^+, similar to what we described for HA. As soon as the CO_2 concentration rises, there is a chemical flux of carbonic acid that increases intracellular HCO_3^- and H^+; this rate is maximum at the beginning and then decreases as the concentration of carbonic acid increases and the hydration of CO_2 slows. The pH_i recovery is coordinated primarily by the extrusion of protons by the NHE and also buffered by phosphate.

The pH_i recovery seen during IH differs from the one observed during HA in that IH evokes a more pronounced pH_i recovery (i.e., the pH of the plateau phase is less acidic). The reason for this enhanced pH_i regulation is that during IH, the NHE is pumping H^+ out of the cell with a chemical gradient that is more favorable. Inhibition of the AE would also impair pH_i recovery during IH by the same means described in the HA challenge. Removing the acid load causes an alkalotic overshoot followed by acidification and recovery to steady-state baseline pH_i as described for the HA simulation. The alkalotic overshoot is caused by the increased activity of the NHE that, upon CO_2 removal, causes a fast increase in pH_i; the recovery to baseline is also aided by the AE. Note that in Figure 2.6 during IH, the membrane potential hyperpolarizes and stays more negative compared to baseline; this response is also different than the small hyperpolarization followed by depolarization seen during HA. These observations suggest small but potentially important effects of pH_i on cell excitability.

Role of the NHE during acid recovery

Cells have to extrude protons permanently to maintain pH_i constant, and this extrusion occurs typically via the NHE and/or by the NDCBE (17). Previous work has reported that inhibition of the NDCBE results in no acidification of steady-state pH_i and no impairment in pH_i recovery in chemosensitive neurons (146), an effect opposite to what happens upon inhibition of NHE, suggesting no important role of the NDCBE on pH_i regulation in chemosensitive neurons. Out of the more than six NHE subtypes (isoforms), the ubiquitous NHE1 is the hypothesized housekeeping enzyme for pH_i regulation in nearly all tissues. In chemosensitive neurons, pH_i regulation during HA has been suggested to be primarily mediated by NHE (121). Amiloride, an inhibitor of multiple isoforms of the NHE, including the NHE1 isoform, has been used widely to test the role of this transporter in pH_i regulation (121). We wanted to test if our model captures the dynamics of such an experiment.

Figure 2.7 shows the time course of the response to simulated HA during NHE inhibition using our model. The simulation starts with a short baseline followed by an increase in CO_2 from 40 mmHg to 80 mmHg during 400 s with simultaneous inhibition of the NHE produced by reducing the amount of the enzyme in the model (90% inhibition, $E_{NHE} = 0.05$, see Table 2.1); the system is then returned to normocapnic conditions and normal NHE expression levels. We observed the same magnitude initial drop in pH_i during HA when NHE is

inhibited, but it is followed by a continued acidification (i.e., no recovery), which is caused by the inability of the NHE to extrude the newly formed H^+ as was expected due to the simulated presence of amiloride. Removing the acid load and the inhibition returns the cell back to steady-state with no pH_i overshoot.

Role of the AE during Alkali load

In addition to acid extruders, which are important for acid challenges, acid loaders give cells the ability to recover from alkalotic conditions. However, because baseline and changing pH_i is the result of the balance between acid loading and extrusion, inhibition of either one of these mechanisms can alter the typical response to acid-base perturbations. Hypocapnic alkalosis (a decrease in CO_2 that causes pH_i increase) is used as a way to further enhance the difference between pH_i and pH_o in experiments studying CO_2/H^+ chemoreception. The reduction in the CO_2 concentration right after HA or IH has the effect of increasing pH_o above the level observed under normal HA or IH allowing for separation of pH_i-pH_o effects in FR. Decreased levels of CO_2 without AE inhibition causes a rapid dehydration of H_2CO_3 that consumes H^+ and HCO_3^- and results in an increase in pH_i. This alkalinization is partially offset by intracellular buffering capacity and transmembrane loading of H^+.

The main transporter involved on this recovery from alkalization is the AE. The process is mediated by the extrusion of HCO_3^- in exchange for Cl^-. Bicarbonate leaving the cell not only decreases the rate at which H_2CO_3 is being generated, but also decreases the amount of buffer and therefore causes a decrease in pH_i (recovery). Removal of decreased levels of CO_2 causes an under-shoot in pH_i mediated by AE. After a few minutes, the cell returns back to steady-state at the pH_i observed before the hypocapnic challenge.

Figure 2.8 shows the time course of the response to simulated hypocapnic alkalosis using our model when the AE is simultaneously inhibited. The simulation starts with a short baseline followed by and decrease in CO_2 from 40 mmHg to 20 mmHg during 400 s with simultaneous inhibition of the AE (simulating DIDS) produced by reducing the amount of the enzyme in the model (90% inhibition, $E_{AE} = 1x10^{-9}$); the system is then returned to normocapnic conditions and normal AE expression levels. During hypocapnic alkalosis with AE inhibition, the initial the increase in pH_i is observed, but in contrast to what would be expected without inhibition, an alkalinization drift is seen. This drift is caused by the inability of the AE to extrude the HCO_3^-, as would be expected in the presence of DIDS. Removing the alkali load and the inhibition returns the cell back to steady-state at the pH_i with no under-shoot.

2.4 Discussion

The model is capable of producing a large number of behaviors that are seen experimentally. The model allows separation of the contribution of each one of the membrane transporters to pH_i regulation under HA, and gives insight into the potential mechanisms responsible for different responses to acid or alkali loads.

However, the model has multiple limitations and some of them deserve to be addressed here.

Most of our model parameters come from tissues different than the region of interest, or they are the result of fine tuning exercises, generating a collage of kinetics that might not represent well the neurons that we intended to study. We are currently investigating ways to generate a more reliable set of data from the regions of interest and recalculate these values for the model. In addition, it has been reported that bicarbonate withdrawal from the extracellular compartment (and substituted by equimolar amounts of HEPES at normal pH) causes a slow intracellular acidification, probably as the result of passive efflux of HCO_3^- favored by the electrochemical gradient (146), suggesting a finite permeability for HCO_3^- that is not included in our model, but might play a role in pH_i regulation and chemosensitivity. The way we designed the model makes it very easy to account for this observation, and we will investigate this point later.

In applying this model to the pH_i changes obtained with exposure to CO_2, we observed that the initial rate of drop in pH_i is approximately proportional to the permeability of the membrane to CO_2, which in the model is related to the activity of CA. Further, the extent of the change is proportional to the buffering power, and the rate of change during the plateau phase is determined by the extent to which proton pumping via NHE exceeds proton entry via CO_2 dissociation or Cl^-/HCO_3^- exchange. After the removal of CO_2, the overshoot in pH_i is caused by the NHE. With reduced or no NHE activity, we noticed that both the positive slope during the plateau phase and the overshoot disappear from the pH_i trace. Further, almost all the influx of H^+ ions due to the chemical flux of carbonic acid is balanced by the NHE, and the tiny fraction of the H^+ left is buffered by phosphate, making the other two buffers secondary in terms of pH_i regulation when only CO_2 levels are varied.

In the simulation of the NH_4^+ prepulse experiment, we noted that the initial rate of pH_i increase is determined by P_{NH3}, and the extent of change in pH_i by the intrinsic buffering capacity and the slope of the plateau phase is determined by P_{NH4} and the NHE. The finite permeability of NH_4^+ causes a delayed acidification after the rapid influx of NH_3 that causes an intracellular alkalinization. Upon removal of NH_4^+ from the medium, the system undergoes an acidification owing to the NH_4^+ permeability and favorable electrochemical gradient for NH_4^+ entry. The result is that less NH_4^+ leaves the cell. pH_i is finally normalized by NH_4^+ extrusion by the NHE.

Both of the time courses described above reflect changes observed experimentally in neurons. However, the lack of additional pathways for acid load/extrusion prevents us from making strong claims about the role of our acid-base elements (NHE and AE) and their role in pH_i regulation, since they are the only acid extruder and acid loader, respectively, present in the model. A few things that we want to consider in the future are 1) adding a finite permeability for HCO_3^- so proton shuttling is allowed during exposure to CO_2 and 2) inclusion of the Na^+ driven Cl^--HCO_3^- exchanger (17) and/or H^+-ATPase, as they will provide

additional pathways and result in a more robust configuration for the role the acid-base elements in pH_i regulation.

Despite the aforementioned limitations, our model seems to be a powerful tool to study processes in which pH_i regulation is part of the puzzle, and this is certainly the case in studies of central CO_2/H^+ chemoreception. For example, the almost ubiquitous lack of pH_i regulation observed in respiratory centers in the brainstem posed the question: what are the differences in these brainstem neurons that impede them from regulating pH? Most of the studies have postulated that the NHE would be the perfect candidate for explaining differences in pH_i regulation (121, 146). On the other hand the Cl^--HCO_3^- exchanger, which is very important for recovery from alkalinization, has been less well studied and could also play an important role in pH_i regulation during HA. One study reported that the AE is not present in NTS neurons, but the observation was not conclusive for chemosensitive neurons since VLM cells do have the exchanger (121). At the same time, CA has been postulated to play a role in central CO_2/H^+ chemosensitivity based on studies demonstrating a role for CA in the regulation extracellular pH (119); however, another study using the CA inhibitor acetazolamide concluded that chemoreception does not involve CA (102). We intend to use our model to address some of these questions from a theoretical perspective and help validate or refute current hypotheses as well as to test novel mechanisms that may potentially be involved in CO_2/H^+ chemoreception.

Finally, central CO_2/H^+ chemoreceptors involved in respiration are excitable neurons (124) that change their membrane potential dynamics (i.e., firing rate) in response to changes in the level of CO_2. Even though our current model has only passive properties and no excitable capabilities, our simulations demonstrated that HA is capable of eliciting considerable changes in ionic composition albeit these changes were not enough to elicit substantial changes in membrane potential. In other words, an increase in CO_2 may not be sufficient to explain depolarization to a level that can move a neuron from quiescent to spiking behavior or to a significant change in firing rate, but could potentially modulate the firing rate of an already excited neuron via the Nernst equilibrium potential of the ions. A few studies have addressed the issue of CO_2/H^+ sensing and the changes in cell excitability from a mathematical perspective. In general, cell excitability is approached by assuming constant ionic composition and currents described by conductance. We will address this issue by coupling our permeability-based transport model with an excitable component that incorporates voltage-gated channels and/or pH or Ca^{++} sensitive channels. This approach will allow us to study CO_2/H^+ chemosensitivity in a neuron capable of showing changes in firing rate and to address questions regarding the role of acid-base elements in modulating cell excitability responses to HA.

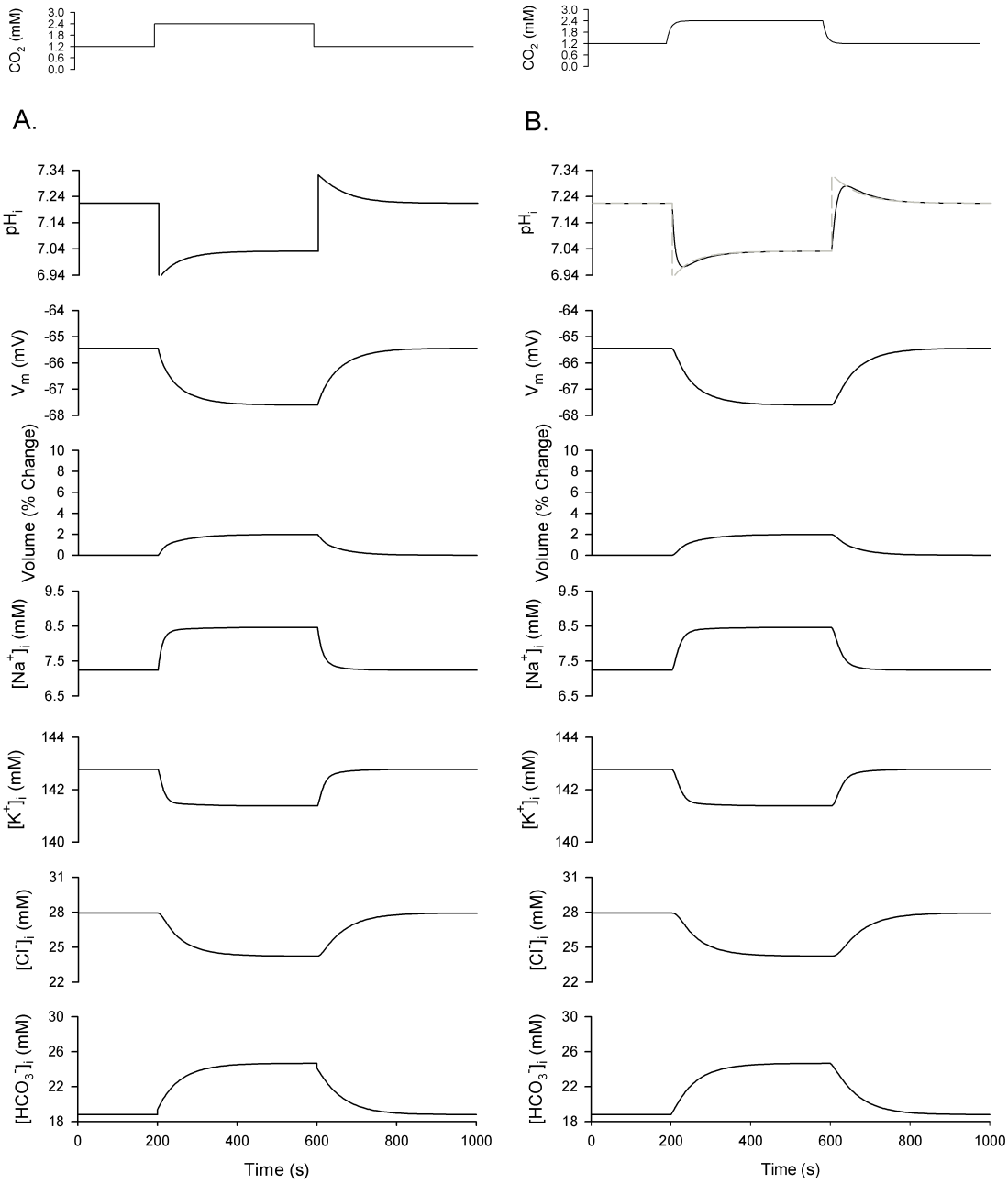

Figure 2.1 Diffusion delay.

Incorporation of a diffusion delay to better capture experimental observations. **A**. Hypercapnic acidosis without delay. Acidification of the intracellular compartment by instantaneously increasing the concentration of CO_2 causes a sharp change in pH and also of the other variables in the model. **B** HA with delay**.** A more realistic approach is an incorporation of diffusion delay (10 seconds time constant diffusion delay or an equivalent 150 µm unstirred layer) that accounts for equilibration of species in perfusion solutions or transport phenomena. The pH response (the second graph on panel B) shows a dashed line that corresponds to the pH trace with out diffusion delay for comparison.

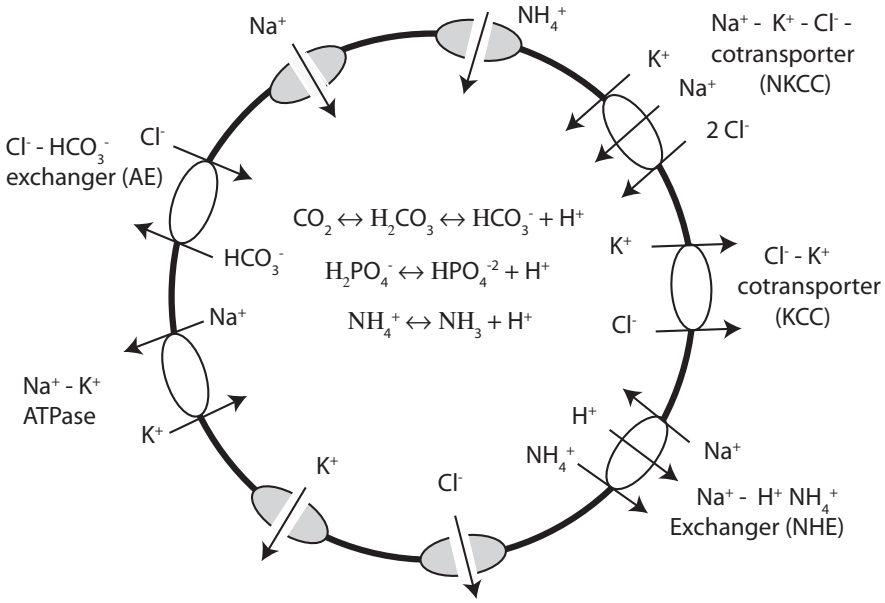

Figure 2.2 Description of the model.

The model incorporates passive diffusion, kinetic models for the Na^+ - K^+ pump, the anion exchanger (AE) the sodium hydrogen exchanger (NHE) the Na^+ - K^+ -Cl^- cotransporter (NKCC) and K^+- Cl^- cotransporter (KCC). Three buffers in equilibrium and catalytic effects of carbonic anhydrase (CA).

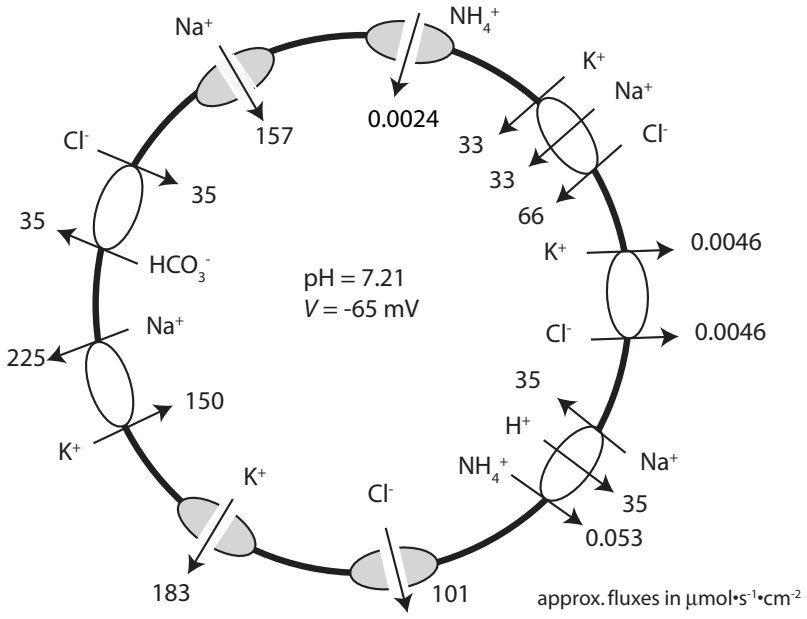

Figure 2.3 Steady State fluxes.

When equations 2.1 and 2.3 are integrated numerically using the parameters listed in Table 2.1, a steady-state is achieved. Note that the membrane potential that results for a zero accumulation of charge is -65 mV, consistent with values reported for neurons in the VLM (132), but hyperpolarized for values reported for CO_2/H^+ chemosensitive neurons (46). The arrows denote the direction of the fluxes for the given intracellular and extracellular solutes and membrane potential.

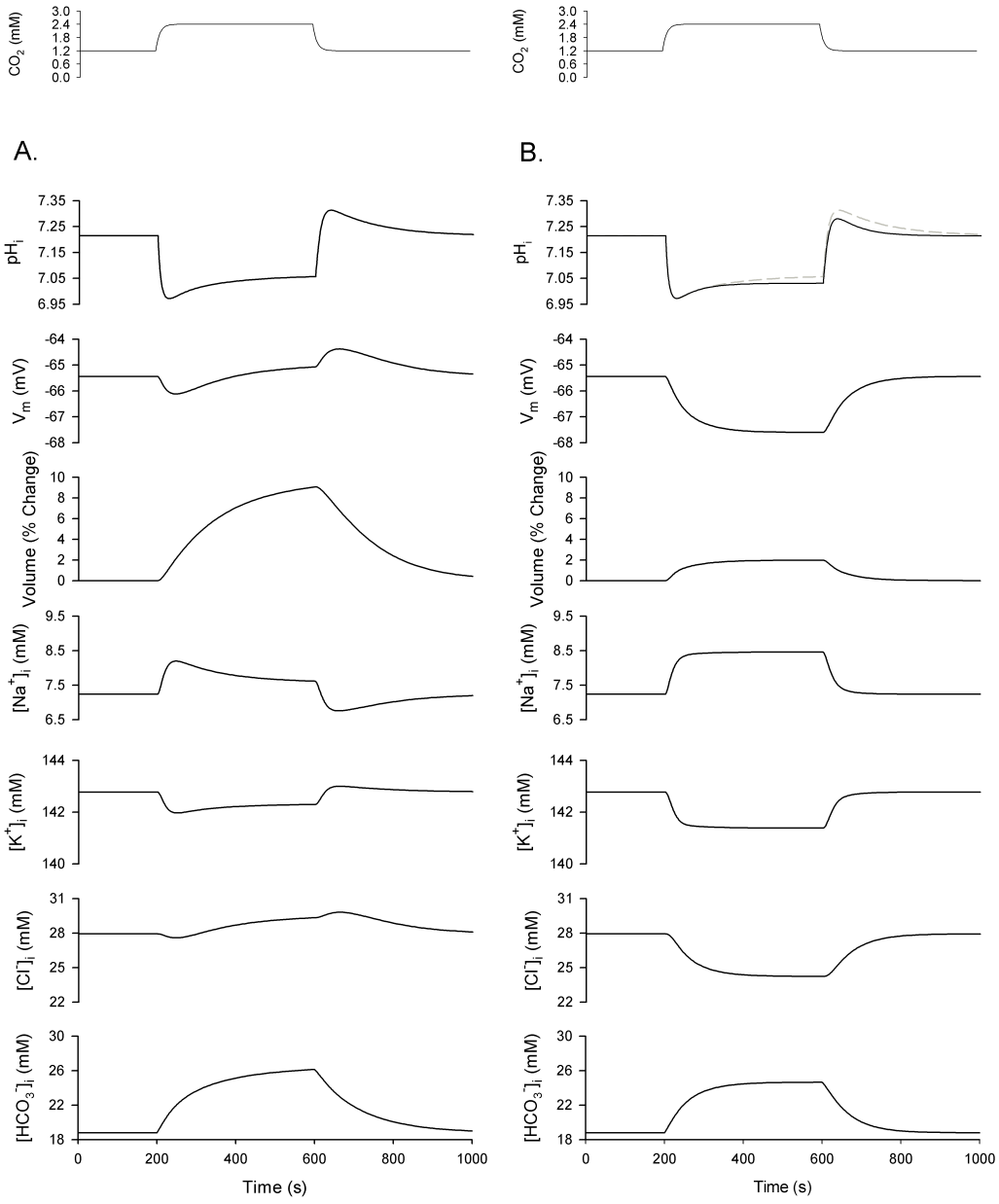

Figure 2.4 Hypercapnic acidosis.

Responses to HA, which were produced by increasing the concentration of CO_2 from 1.2 mM (40 mmHg) to 2.4 mM (80 mmHg) (indicated by the top plot) from the 200 s time point to the 600 s time point. **A**. HA without volume regulation. During HA, the fall in pH_i was accompanied by a relatively large increase in cell volume. Also plotted on the graph are membrane potential and the concentrations of Na^+, K^+, Cl^-, HCO_3^-. **B**. HA with volume regulation. Following modification of the activities of the NKCC and KCC cotransporters to achieve volume regulation, the fall in pH_i was accompanied by only a small increase in cell volume. Note the differences from panel A in which a 10% volume change was predicted compared to 2% in panel B. This volume regulation occurs at the expense of larger changes in ionic composition. The pH_i response (the first plot in panel B) shows a dashed line that corresponds to the pH_i trace without volume regulation for comparison. The simulations include the diffusion delay described above.

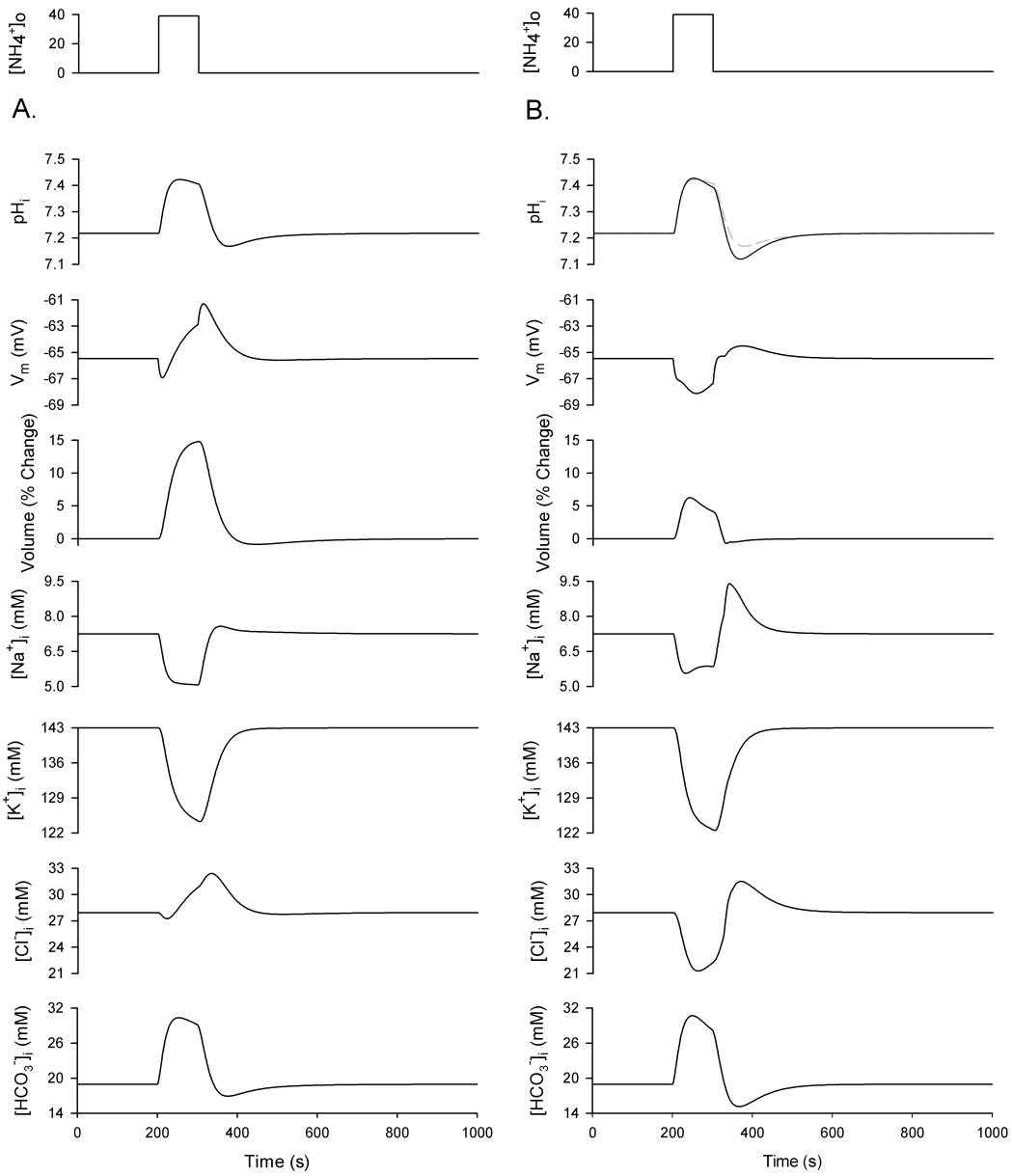

Figure 2.5 Ammonium pre-pulse

Responses to an NH_4^+ prepulse produced by increasing the outside concentration of the relatively impermeable NH_4^+ from 0.01 to 39 mM for 100 s. **A**. Ammonium prepulse experiment without volume regulation. During the NH_4^+ prepulse stimulus, the rapid rise in pH_i is accompanied by a large increase in cell volume. With removal of the NH_4^+ prepulse stimulus, pH_i rapidly acidifies, followed by pH_i recovery. Also plotted on the graph are membrane potential and concentrations Na^+, K^+, Cl^-, and HCO_3^-. **B**. Ammonium prepulse experiment with volume regulation. With implementation of volume regulation mechanisms, the rise in pH_i was accompanied by a markedly attenuated increase in cell volume. The pH_i response (the first plot on panel B) shows a dashed line that corresponds to the pH_i trace without volume regulation for comparison. The simulations include the diffusion delay.

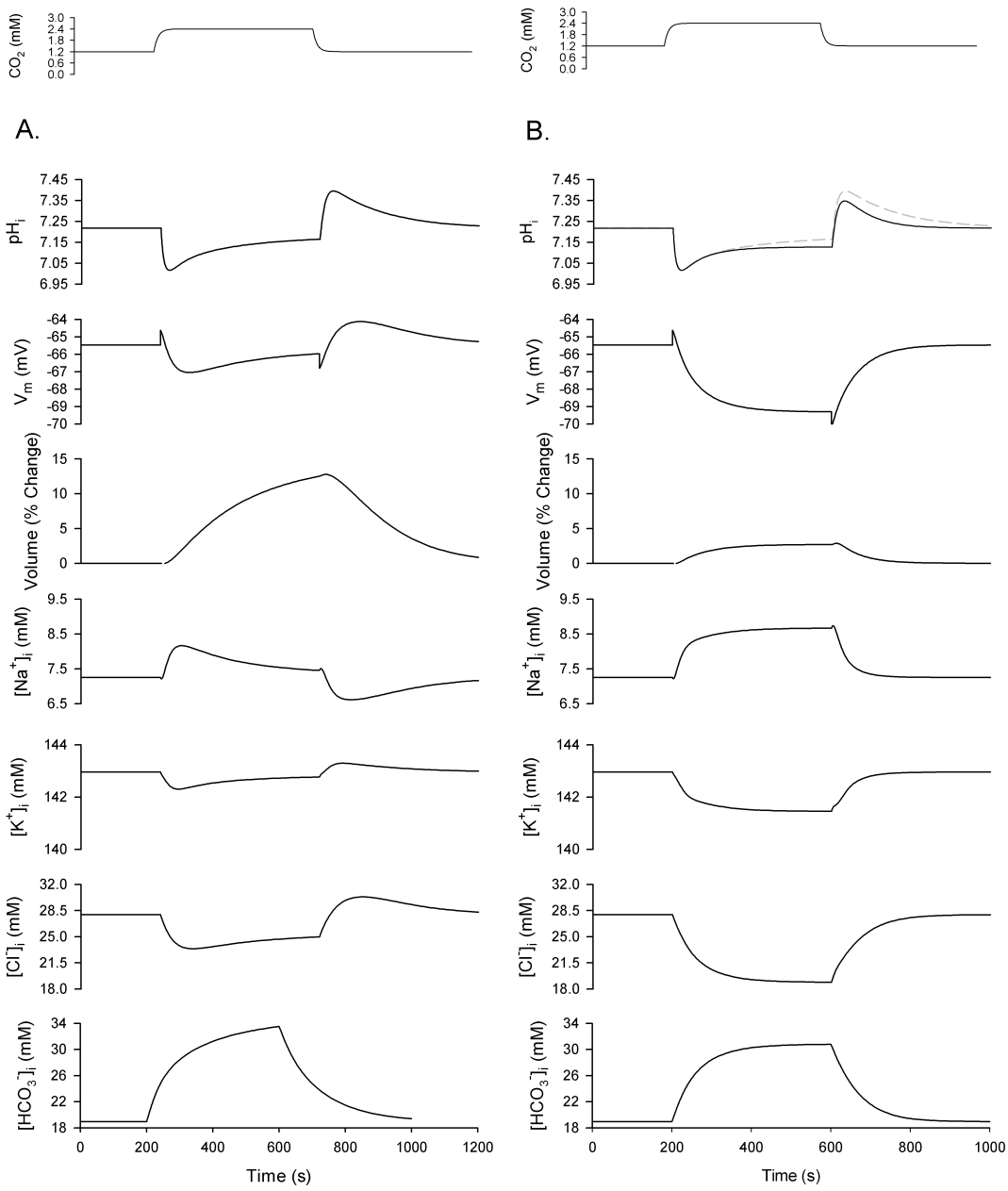

Figure 2.6 Isohydric Hypercapnia

Responses to IH, which were produced by increasing the concentration of CO_2 from 1.2 mM (40 mmHg) to 2.4 mM (80 mmHg) (indicated by the top plot) and the concentration of bicarbonate from 24 mM to 48 mM (to hold pH_o constant) from the 200 s time point to the 600 s time point. **A**. IH without volume regulation. During IH, the fall in pH_i was accompanied by a relatively large increase in cell volume. Also plotted on the graph are membrane potential and the concentrations of Na^+, K^+, Cl^-, HCO_3^-. **B**. IH with volume regulation. With implementation of volume regulation mechanisms, the fall in pH_i was accompanied by only a small increase in cell volume. The pH_i response (the first plot in panel B) shows a dashed line that corresponds to the pH_i trace without volume regulation for comparison. The simulations include the diffusion delay described above.

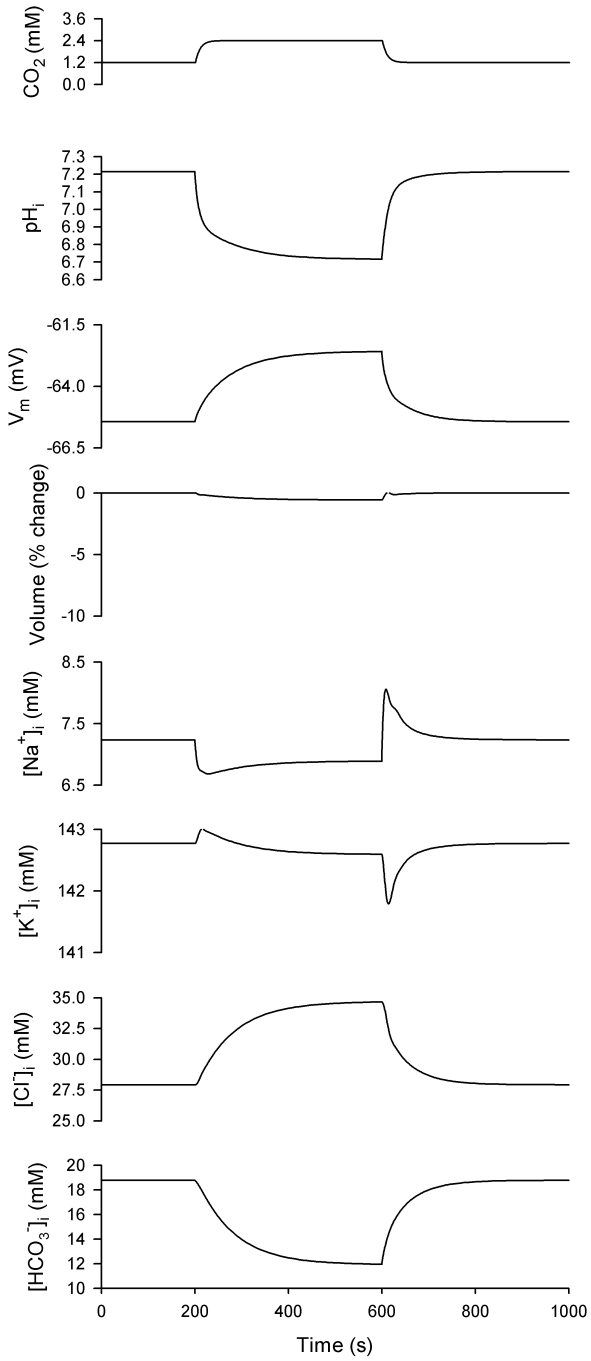

Figure 2.7 Hypercapnic acidosis and the role of the NHE.

As in Figure 2.4, HA was produced by increasing the concentration of CO_2 from 1.2 mM (40 mmHg) to 2.4 mM (80 mmHg) from the 200 s time point to the 600 s time point while at the same time, the expression of NHE was inhibited by reducing the amount of enzyme by 90% from 0.5 to 0.05 (i.e., amiloride inhibition). Under these conditions, HA acidified the intracellular compartment, but the pH_i recovery response was eliminated. Also plotted on the graph are cell volume, membrane potential, and the concentrations of Na^+, K^+, Cl^-, and HCO_3^-. The simulation includes volume regulation mechanisms and the diffusion delay.

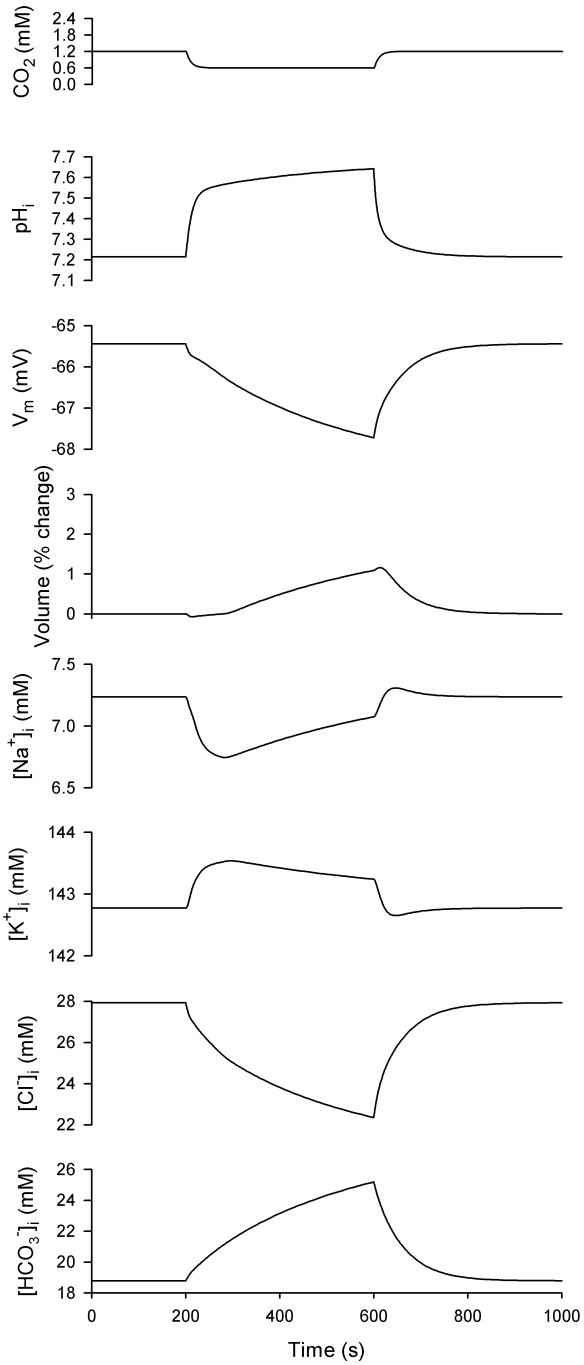

Figure 2.8 Hypocapnic alkalosis and the role of the AE.

Alkalinization of the intracellular compartment was produced by decreasing the concentration of CO_2 from 1.2 mM (40 mmHg) to 0.6 mM (20 mmHg) from the 200 s time point to the 600 s time point while at the same time, the expression of AE was inhibited by reducing the amount of enzyme by 90% (E_{AE} was changed from 1×10^{-8} to 1×10^{-9}) (i.e., DIDS inhibition). Lowering the concentration of CO_2 during AE inhibition produced a continuous rise in pH_i, with no under-shoot being observed with return to baseline conditions. Also plotted on the graph are cell volume, membrane potential, and the concentrations of Na^+, K^+, Cl^-, and HCO_3^-. The simulation includes volume regulation mechanisms and the diffusion delay.

Table 2.1 Model Parameters

Parameter [Units]	Value	Note / Reference
Passive Ionic Permeabilities		
P_{Na} [cm·s^{-1}]	4 x 10^{-7}	Tunable parameter (43)
P_{K} [cm·s^{-1}]	8 x 10^{-6}	Tunable parameter (43)
P_{cl} [cm·s^{-1}]	2 x 10^{-8}	Tunable parameter (43)
P_{X} [cm·s^{-1}]	0	Assumed to be impermeable
P_{Y} [cm·s^{-1}]	0	Assumed to be impermeable
P_{H2CO3} [cm·s^{-1}]		assumed to be generated by CO_2 which is freely permeable
P_{HCO3} [cm·s^{-1}]	0	Assumed to be impermeable
P_{H} [cm·s^{-1}]	0	Assumed to be impermeable
P_{H2PO4} [cm·s^{-1}]	0	Assumed to be impermeable
P_{HPO4} [cm·s^{-1}]	0	Assumed to be impermeable
P_{NH4} [cm·s^{-1}]	1 × 10^{-7}	Tunable parameter (126)
P_{NH3} [cm·s^{-1}]	1 × 10^{-3}	Tunable parameter (126)
Acid-base regulation		
C_{CO2} [mM]	varies	Normal levels are 40 mmHg or 2.4 mM
k_h [s^{-1}]	0.18	*
k_d [s^{-1}]	64	*
K_{HCO3} [mM]	0.34	(11)
K_{H2PO4} [mM]	1.5 × 10^{-4}	(11)
K_{HCO3} [mM]	6.62 × 10^{-7}	(11)
Na^+-H^+ Exchanger (NHE)		
E_{NHE}	0.5	Tunable parameter (144)

Table 2.1 Model Parameters - continue

Parameter [Units]	Value	Note/Reference
k [mM]	1.78×10^{-4}	Tunable parameter (135)
Na^+-K^+ ATPase		
i_{max} [μA/μF]	40	(87)
Cl^--HCO_3^- Exchanger (AE)		
E_{AE}	1×10^{-8}	Tunable parameter (24)
Na^+ - K^+ - Cl^- Cotransporter (NKCC)		
E_{NKCC}^{MAX}	1×10^{-3}	Tunable parameter (90)
E_{NKCC}^{MIN}	1.9×10^{-5}	Tunable parameter (90)
K^+ - Cl^- Cotransporter (KCC)		
E_{KCC}^{MAX}	5×10^{-6}	Tunable parameter (90)
E_{KCC}^{MIN}	5×10^{-11}	Tunable parameter (90)

* hydration and dehydration rates can be affected by the presence of carbonic anhydrase. The rates can be increased by a factor of a thousand with the catalyzed reaction. (11)

Table 2.2 Intracellular and Extracellular Concentrations – Steady-state

Intracellular concentrations [mM]	Extracellular Concentrations [mM]
$C^{i}_{Na} = 7.23$	$C^{o}_{Na} = 140$
$C^{i}_{K} = 142.77$	$C^{o}_{K} = 4$
$C^{i}_{Cl} = 27.93$	$C^{o}_{Cl} = 105$
$C^{i}_{X} = 97.29$	$C^{o}_{X} = 9.74$
$C^{i}_{Y} = 2.24$	$C^{o}_{Y} = 14.26$
$C^{i}_{H} = 6.09 \times 10^{-5}$ (pH_i =7.21)	$C^{o}_{H} = 3.72 \times 10^{-5}$ (pH_o = 7.43)
$C^{i}_{H2CO3} = 0.0042$	$C^{o}_{H2CO3} = 0.0033$
$C^{i}_{HCO3} = 18.78$	$C^{o}_{HCO3} = 23.99$
$C^{i}_{H2PO4} = 1.08$	$C^{o}_{H2PO4} = 0.59$
$C^{i}_{HPO4} = 2.65$	$C^{o}_{HPO4} = 2.4$
$C^{i}_{NH4} = 0.0084$	$C^{o}_{NH4} = 0.0098$
$C^{i}_{NH3} = 7.76 \times 10^{-5}$	$C^{o}_{NH3} = 0.00015$
Cell Volume (W): 0.00033791 L (for an Area of 1 cm^2)	
Membrane Potential (V): -65.44 mV	

Note: The distribution of ion species inside and outside the cell is the result of steady state concentrations at which the inward and outward fluxes balance and no change ion concentrations is observed over time. This values are used as initial conditions and for baseline values for all the simulations described on the results section. Values shown in this table were obtained using the parameters listed in Table 2.1. Note that the values obtained at steady-state meet the electroneutrality (zero net charge) and osmolarity (300 mOsm) constrains.

Chapter 3 - Cellular mechanism involved in CO_2/H^+ chemoreception

3.1 Introduction

Central respiratory chemoreceptors (CRC) are fundamental for the control of breathing. Presumably, they adjust ventilation by intrinsically sensing CO_2/H^+ and by changing (e.g., increasing or decreasing) their firing rate (FR) to maintain whole body pH homeostasis. Chemosensitive regions include: the ventral medullary surface –VLM- including the retrotrapezoidal nucleus –RTN- (95, 135), the nucleus of solitary tract –NTS- (48, 93), the locus coeruleus –LC- (46), the rostral aspect of the ventral respiratory group –rVRG- (116), the fastigal nucleus of the cerebellum, the pre-Bötzinger complex (129), and the medullary raphé nuclei (118).

The signal involved in CO_2/H^+ chemosensitivity has been the object of much debate and mechanisms for transduction of this signal remain largely unknown. In theory, these sensory components of ventilatory control could be responding to changes in O_2, CO_2, pH, and HCO_3^-. The main argument for a role of CO_2 is the large response to hypercapnic acidosis (HA) – a decrease in pH_i and pH_o as CO_2 rises- compared to metabolic acidosis (110). Exposure to HA, isocapnic acidosis (IA) –a decrease in pH_o at constant CO_2 - and isohydric hypercapnia (IH) – an increase of CO_2 at constant pH_o- induce increases in firing rate, suggesting a strong role for pH_i but also some role for pH_o (140). Nevertheless, there is also evidence against pH_o (61, 86, 110) and pH_i (the hypoxia-paradox (110)), as the primary signals in central CO_2/H^+ chemoreceptors.

Early studies began by asking the question of whether CO_2/H^+ neurons could be identified by the way they respond to acid challenges. To begin to address this issue, experiments measuring pH_i using the pH sensitive dye BCECF were conducted in neonatal rat transverse medullary slices. These experiments demonstrated that neurons from putative chemosensitive areas of the medulla (VLM and NTS) acidified and remained acidified during exposure to HA while neurons from non-chemosensitive areas (IO and hypoglossal motor nucleus) showed substantial pH_i recovery from acidification during HA (122). However, in older (>P15) rats, neurons in non-chemosensitive areas also lacked pH_i recovery when exposed to HA (104), suggesting that the response may not be unique to chemosensitive neurons. In addition, experiments on brainstems from the invertebrate *Helix aspersa* suggested that identification of neurons as chemosensitive based on pH regulatory profiles is an insensitive marker of chemosensitivity (53).

The lack of pH_i regulation observed in respiratory centers in the brainstem suggests, at least from a theoretical point of view, two possible scenarios: 1) the intrinsic buffering capacity in chemosensitive neurons is different compared to non-chemosensitive neurons and/or 2) the pH_i regulating mechanisms (the acid

loader and extruders) are different or not present in chemosensitive neurons. With respect to the first possibility, previous observations have shown that the intrinsic buffering capacity is the same in chemosensitive and non-chemosensitive neurons (121). This is not surprising because differences in intrinsic buffering capacity would affect primarily the initial drop of pH_i during HA, but this does not appear to different between these two kinds of neurons. On the other hand, the mechanisms involved in pH_i regulation seem to be differently expressed in these neurons. For example, removal of extracellular chloride at steady-state pH has been shown to produce intracellular alkalization in all Hyp, IO, and VLM neurons, but results in acidification in NTS neurons (121). This suggests that the Cl^-/HCO_3^- exchanger (AE) is present in Hyp, IO, and VLM neurons, but not in NTS neurons (121). This experiment also reported that the pH_o-pH_i relationship has a steeper slope in chemosensitive neurons; for a given change in pH_o, pH_i exhibits a larger change in chemosensitive neurons compared to non-chemosensitive neurons (121). There is also evidence that chemosensitive neurons from the NTS and VLM have a NHE that is far more sensitive to changes in pH_o (inhibited at pH ~7) than non-chemosensitive neurons from the IO and Hyp (where it was inhibited at pH ~6.7). This supports the idea that a different Na^+/H^+ exchanger (NHE) isoform (in particular NHE3) could be a possible mechanism (121).

In addition, the blunted pH_i response of CO_2/H^+ chemoreceptors seems to be part of an intricate set of signals that include CO_2, pH_o, and HCO_3^-, each of which has been postulated to play a role in the CO_2/H^+ chemosensitive response. We think that this problem is very amenable to mathematical modeling and, to our knowledge, there is only one study that uses this approach to characterize CO_2 chemosensitivity in *Helix aspersa* (25). However, this model is only applicable to invertebrates and uses empirical functions to simulate pH_i regulation. Thus, with the aim of expanding these ideas to a more mammalian-relevant framework, and using our robust pH regulation approach, we used our previously-developed single-compartment mathematical model to study possible mechanisms involved in central chemoreception. The model takes into account the simultaneous passive fluxes of major ion species across the membrane, including conjugate pairs of three different buffers. The model also incorporates mechanisms for acid-base regulation and cell volume regulation. The model was able to mimic responses to acid-based perturbations observed in experimental environments, like HA, ammonium pre-pulse experiments, and IH, and we were able to asses the relative importance of the NHE and AE under these challenges.

Here, we want to use our model to test three hypothesis related to CO_2/H^+ chemosensitivity: 1) Besides the ubiquitous NHE1, could a different NHE isoform explain the lack pH_i recovery during HA in CO_2/H^+ chemoreceptors? 2) Could the lack of pH_i recovery in CO_2/H^+ chemoreceptors be explained by a low NHE activity? 3) Could the differences between chemosensitive and non-chemosensitive neurons be explained by a NHE that is less sensitive to pH_i? In addition, we wanted to used the model to 1) quantify the extent to which pH_i

recovery is dependent upon NHE and AE activities and 2) examine the responses to IH in chemosensitive and non-chemosenstive neurons and compare the predicted responses with experimental results.

3.2 Methods

Model description and model parameters

A complete description of the model can be found in Appendix A. Briefly, the mathematical model evaluates the roles of intrinsic buffering capacity, Na^+/H^+ exchange (NHE), and HCO_3^-/Cl^- exchange (AE) on pH_i regulation in response to simulated acid or alkali challenges. The cell model incorporates conservation of mass and electroneutrality constraints, kinetic models of the Na^+/K^+-ATPase, AE, NHE, carbonic anhydrase (CA), Cl^- currents (NKCC1 and KCC2), and passive permeation pathways for ions, non-electrolytes, and H_2O. H^+ buffering (both inside and out) is handled by multiple buffers species all subject to the isohydric principle. For a description of the numerical methods implemented to compute membrane potential, integrate state variables, compute the concentration of H^+, and the diffusion delay, see Appendix C.

We consider the model parameters defined in the previous chapter as the non-chemosensitive configuration since they capture the typical response of "regular" cells (i.e., as opposed to chemoreceptors) to acid-base challenges. To help with our investigations about the cellular mechanisms present in chemosensitive neurons, we modified some of the parameters in the model to represent this population. The criteria for our definition of a chemosensitive neuron was a neuron that shows a blunted pH_i recovery response to HA. The process of finding the parameters that give the "best" qualitative response is described later. Table 3.1 shows the parameters that were adjusted to produce the chemosensitive neuron, and our results are compared to those from the non-chemosensitive neuron. Figure 3.6 shows the response to HA obtained with this set of parameters.

Three different NHE isoforms

Besides the ubiquitous NHE1 isoform found in nearly all tissues, expression of the NHE2, NHE3, and NHE4 isoforms has been reported in the rat brain (89). More recently, the NHE5 isoform has been found to be abundant in the brain (133). Functionally, NHE3 expression in the medulla of conscious rabbits has been shown to contribute to the control of breathing, presumably via pH_i regulation (147). Further support for a role of the NHE3 isoform comes from a previous study demonstrating that inhibition of NHE3 activity reduces steady-state pH_i in ventrolateral medullary neurons and inhibits pH_i regulation after an ammonium prepulse (146), suggesting that NHE3 participates in CO_2/H^+ chemoreception. While experimental evidence for the precise roles of NHE3 and NHE5 is still pending, we decided that our model could be used to test the possible roles of the NHE1, NHE3, and NHE5 in CO_2/H^+ chemoreception.

Our approach to find appropriate kinetic representations of these transporters was to use the mathematical models by Weinstein (144) and Aronson (6) for the typical NHE1 and adjust the parameters to qualitatively match published data. We noticed that the addition of the internal modifier that enhances the transport in response to a fall in pH_i (an experimental finding in renal microvillus vesicles (6)) fit the data well for all three isoforms. Thus, we adjusted the amount of flux of each NHE isoform as a function of different levels of pH_i, as reported in the experimental data. Figure 3.1 shows the H^+ (acid) flux and pKa values for each of the different NHE isoforms. For a given pH, each isoform exhibits a different amount of H^+ flux. At reduced pH, the NHE3 seems to be less active; thus, this isoform appears to be a viable candidate to explain differences in pH_i recovery between chemosensitive and non-chemosensitive neurons.

To estimate the *pKa* for the NHE1, we used the kinetic properties defined by Aronson (6) and also the elegant comparison of NHE isoforms by Attaphitaya and colleagues (7). In the case of NHE3, the pH response was estimated from experiments comparing the pH sensitivity in three different isoforms of the NHE transfected into AP-1 chinese hamster ovary cells (1) and also from studies using NHE-deficient PS120 brain rat cells (7). Finally, the *pKa* for the NHE5 was fitted from studies using NHE-deficient PS120 brain rat cells (7). The parameters used in the model for the different isoforms are shown in Table 3.2

Two different chemosensitive neurons

Experiments by Ritucci and colleagues (121) suggest that chemosensitive neurons from different medullary regions may not exhibit the same level of expression of pH regulation mechanisms. Specifically, their experiments revealed that the Cl^-/HCO_3^- exchanger (AE) is present in chemosensitive VLM neurons as well as in non-chemosensitive hypoglossal and IO neurons, but is not present in chemosensitive NTS neurons (121). On the other hand, the NHE seems to be more sensitive to pH in neurons from both of these chemosensitive regions. We modeled the behavior of neurons that reflect these observations to common experimental perturbations. Table 3.4 shows the parameter selection for the two distinct chemosensitive neuron types. Both sets of neurons have a NHE with reduced affinity for H^+_i (internal modifier off) defined in Table 3.3. VLM neurons have normal levels of AE and NTS neurons show significant reduction (70% inhibition) of AE levels. The levels of expression of the NHE were adjusted so baseline pH_i was the same in both populations.

Simulation of experimental perturbations

Experimental perturbations were performed on a non-chemosensitive configuration as well as on a chemosensitive neuron for comparison. The chemosensitive neuron has all of the acid-base regulation machinery but includes the NHE1 configuration coupled to a reduced pH_i sensitivity (as VLM neurons above). Table 3.3 summarizes the experiments and the values for the different elements in the model. The perturbations used in this study were defined as follows:

1. NHE less sensitive to pH_i: The model incorporates an internal modifier that enhances the transport (increases the permeation coefficient for each one of ions P_{Na}, P_H, and P_{NH4}; see equations A.20 - A.22 and A.24) in response to a rise in C_H^i. To mathematically remove this effect, we set $f_M = 1$ and $k = 0$ in equation B. 26. The parameter configuration for a chemosensitive neuron is shown in Table 3.1 for comparison with a non-chemosensitive neuron, and again in Table 3.3 to summarize the perturbation.

2. Amiloride: Inhibition of NHE1 was simulated in the model by reducing the expression of the transporter (E_{NHE}) by 80%. Table 3.3 shows the three different levels of NHE expression (first column) used for Figure 3.3 and the level of NHE for the amiloride experiment (second column) depicted in Figure 3.4.

3. DIDS: 4,4'-diisothiocyanatostilbene-2,2′-disulfonic acid (DIDS) is an inhibitor of the AE. To simulate the effect of this drug, we reduced the amount of expression of the AE by 70% (70% inhibition). This change is reported in Table 3.3 and was used to test the role of the AE during hypocapnic alkalosis shown in Figure 3.5.

3.3 Results & Discussion

NHE isoform and hypercapnic acidosis

To test the hypothesis that the difference in pH_i regulation during HA between CO_2 chemosensitive and non-chemosensitive cells is due to different NHE isoforms, we examined the pH_i response to simulated HA using the model with the kinetics for the NHE1, NHE3, and NHE5 isoforms, as summarized in Figure 3.1. Figure 3.2 shows the results of these simulations. Each simulation starts with a baseline of 200 s followed by three step-wise progressive increases in CO_2: from 1.2 mM (baseline) to 2.4 mM, then to 3.6 mM, and then to 4.8 mM CO_2, (duration of 400 s each). The system is then returned to normocapnic conditions. Regardless of the NHE isoform tested, at each step, the typical drop in pH_i caused by the dissociation of CO_2 that increases intracellular HCO_3^- and H^+ is observed. After the initial drop in pH_i, a fast recovery that eventually plateaus occurs, and a new state is reached at a lower pH_i (the larger the increase in CO_2, the lower the pH_i at which the response plateaus). The recovery, as explained in chapter 2, is the consequence of the balance between the addition and extrusion of protons, mainly mediated by NHE and AE. Removing the acid load causes an alkalotic overshoot followed by acidification and recovery to steady-state baseline pH_i. The pH_i response curves for each of the three NHE isoforms virtually overlap, with all isoforms showing pH_i recovery from acidic conditions at each level of CO_2 tested and the same magnitude of overshoot after remove of CO_2. These results suggest that the difference in pH_i regulation during HA between CO_2 chemosensitive and non-chemosensitive cells is not due to expression of different NHE isoforms.

The NHE and the AE are important for pH_i recovery

To test the hypothesis that lack of pH_i recovery during HA in CO_2 chemosensitive cells is due to low NHE activity, we examined the effects of HA in combination with reducing NHE activity (*i.e.*, 0%, 25%, and 50% blockade of NHE) on pH_i recovery. Figure 3.3 shows the results of these simulations, which were performed using the model with the kinetics of each of the three NHE isoforms (NHE1,NHE3, and NHE5) described above. Each simulation starts with a short baseline followed by an increase in CO_2 from 40 mmHg to 80 mmHg for 400 s while simultaneously inhibiting the amount of the NHE by 0%, 25%, and 50%. For each NHE isoform, the same simulation was run, and the results of each run are displayed superimposed in Figure 3.3. After the CO_2 challenge, the system is returned to normocapnic conditions. These simulations revealed that regardless of the NHE isoform tested, pH_i recovery is seen during low NHE activity (e.g., 25%), but is markedly impaired with greater NHE inhibition, which demonstrates that pH_i recovery is blunted in a dose-dependent manner. These simulations also demonstrated that reduced NHE activity is sufficient to decrease pH_i in the absence of increased CO_2 and that the fall in pH_i during simulated hypercapnia is exacerbated (not shown in Figure 3.3), suggesting that NHE activity plays an important role in maintaining basal levels of pH_i and that the transporter should be present in chemosensitive neurons. Therefore, other mechanisms have to be responsible for the blunted pH_i response seen during HA in chemosensitive neurons. In addition, it should be noted that the three levels of inhibition exert practically the same effect for each of the three different NHE isoforms, suggesting, once again, that differential levels of expression of different NHE isoforms cannot explain the difference in pH_i regulation during HA between CO_2 chemosensitive and non-chemosensitive neurons.

Previous reports have also examined potential mechanisms for pH_i regulation during IH (increased CO_2 at constant levels of pH_o) in different populations of CO_2 chemosensitive neurons. These experiments have demonstrated that pH_i recovery during IH was completely inhibited in NTS and VLM neurons upon exposure to amiloride (an inhibitor of the NHE) but not when the neurons were exposed to DIDS (an inhibitor of the AE) (122). Neurons from non-chemosensitive areas subjected to HA also exhibit this behavior (i.e., inhibition of pH_i recovery during exposure to amiloride and not to DIDS) (122), suggesting that NHE may be the only acid regulation mechanism present in these neurons. Therefore, we wanted to test if the model could capture the effect of amiloride during HA in non-chemosensitive neurons; the results of this simulation are shown in Figure 3.4. The simulation starts with a short baseline followed by an increase in CO_2 from 1.2 mM to 2.4 mM for 50 seconds, at which point inhibition of NHE by 80% is added concurrent with the HA challenge for an additional 150 s. The NHE is then restored to normal levels for an additional 200 s, after which, the system is returned to normocapnic conditions. With removal of CO_2, the traditional overshoot is observed before restoration of baseline pH_i. Results from a simulation without NHE inhibition are also shown in Figure 3.4 (dotted line) for

comparison. This simulation demonstrates that NHE inhibition causes a halt in pH_i recovery during HA that is reversible upon NHE disinhibition. Thus, the model captures the effects of amiloride on the NHE, and demonstrates that NHE activity is fundamental for pH_i recovery during HA.

To test the hypothesis that pH_i recovery is dependent upon AE activity, we examined the effects of simulated blockade of the AE on pH_i recovery. For this simulation, we implemented the model using a non-chemosensitive neuron and hypocapnic alkalosis (a decrease in CO_2 that causes an increase in pH_i) as the acid-base disturbance. Figure 3.5 shows the results of this simulation. The simulation starts with a short baseline followed by a decrease in CO_2 from 1.2 mM to 0.6 mM for 50 s, at which point inhibition of the AE by 70% (simulating the effect of DIDS) is added concurrent with hypocapnic alkalosis for an additional 150 s. The AE is then restored to normal levels for an additional 200 s, after which, the system is returned to normocapnic conditions. Results from a simulation without AE inhibition are also shown in Figure 3.5 (dotted line) for comparison. This simulation demonstrates that pH_i recovery from alkalinization is impaired by inhibition of AE activity, supporting a role for AE in pH_i regulation.

Effect of the NHE internal modifier on pH regulation

In our previous simulations, we found that expression of different isoforms of the NHE (one of the possible hypotheses to explain the the difference in the pH_i response during HA in chemosensitive neurons) is not sufficient to explain the behavior seen in chemosensitive neurons. However, at the same time, experimental observations and our model show that the NHE is fundamental for maintaining baseline pH_i and for pH_i recovery from acid loads. To reconcile this finding, we hypothesized that the lack of pH_i recovery in CO_2 chemosensitive neurons could be due to a shift in the activation point of the NHE. Thus, we examined the effects of removing the internal modifier that enhances the transport (increases the permeation coefficient for each one of ions that goes through the exchanger: P_{Na}, $P_{H,\ and}$ P_{NH4}) in response to a decrease in pH_i. Figure 3.7 shows the pH_i responses to simulated HA (as defined before) for a neuron with the internal modifier “on” and a neuron with the internal modifier “off” (see methods sections and the appendix for an explanation of the on/off condition of the internal modifier). This simulation reveals that the neuron with the internal modifier “off” exhibits a significantly blunted pH_i response during the HA compared to the neuron with the internal modifier “on”. Based on this observation, we consider these configurations to best represent the chemosensitive and non-chemosensitive neurons, respectively.

As mentioned before, chemosensitive neurons that do not show pH_i recovery during HA do show pH_i recovery during IH. This observation lead to the hypothesis that chemosensitive neurons respond to the pH_i-pH_o gradient rather than to pH_i alone (46). To see if the above configuration for a chemosensitive neuron matches the experimental observations during IH, we compared the results to those obtained with the non-chemosensitive configuration. Figure 3.7 shows that both chemosensitive and non-chemosensitive neurons show pH_i

recovery during IH, suggesting that a constant level of pH_o compensates for the decreased NHE activity and restores the ability of the chemosensitive neuron to recover during IH. This supports the hypothesis that the pH_i-pH_o gradient may be a signal in CO_2/H^+ chemoreception, or points to a possible role or pH_o buffering by glia.

Differences between neurons from the NTS and the VLM

The NTS and the VLM have been proposed as CO_2/H^+ chemosensitive regions (31, 95, 121), and neurons form both regions have been shown to have a poor pH_i regulatory response during HA (121). When examined for transport mechanisms involved in their responses to acid-base perturbations, it was found that neurons from the NTS and the VLM have a NHE that seems to be less sensitive to pH_o compared to the NHE of neurons from non-chemosensitive regions. Further, neurons from the NTS seem to lack the AE which was present in neurons from the VLM (121). Using as a starting point our configuration for a chemosensitive neuron (i.e., VLM), we progressively inhibited the AE until we were able to capture the lack of pH_i recovery during hypocapnic alkalosis, in which VLM neurons recover but NTS neurons stay alkalotic. Figure 3.8 shows a HA simulation for 400 s followed by 400 s recovery followed by 400 s of hypocapnic alkalosis. The condition necessary to obtain a response similar to that observed in NTS neurons experimentally was a 70% inhibition of the AE. The lack of AE in NTS neurons has been postulated to be part of the reason for their increased degree of chemosensitivity, as it generates a more pronounced pH_i-pH_o gradient during HA.

3.4 Perspectives

Previous work has suggested that expression of a different NHE isoform may explain the lack of pH_i recovery in chemosensitive neurons; however, results from our mathematical model suggest that the difference in pH_i regulation during HA between CO_2 chemosensitive and non-chemosensitive neurons cannot be explained by expression of different NHE isoforms. This observation is based on our model simulations demonstrating that pH_i recovery is seen during HA regardless of the NHE isoform incorporated. For our simulations, we used the previously described kinetics for the NHE1, NHE3, and NHE5 isoforms; however, incorporating the NHE3 or the NHE5 instead of the ubiquitously expressed NHE1 in these simulations could not explain the differences between chemosensitive and non-chemosensitive neurons. Although our simulations suggest that a different NHE isoform is not responsible for the behavior seen in chemosensitive neurons, there remains a possibility that the kinetics used in the model differ from those in chemosensitive neurons. Alternatively, all of these NHE isoforms may be expressed at very low levels in chemosensitive neurons so that baseline pH_i is maintained but pH_i recovery during HA is impaired. However, this possibility doesn't seem plausible since the neurons have been shown to recover during IH. One final possibility is the existence of an unknown isoform that shows sensitivity

to pH_i. Here, we investigated this possibility with our model by incorporating a NHE that is less sensitive to pH_i, which is supposed to be the main signal in CO_2/H^+ chemoreception. This simulation showed that a NHE that lacks such sensitivity produces a blunted pH_i recovery response to HA that is very similar to that seen experimentally in chemosensitive neurons. Nevertheless, experimental evidence suggests that the NHE sensitive to pH_o, and we did not test this possibility since our kinetic model for the NHE was not designed to be sensitive to external H^+ aside from the effect of pH_o on the chemical gradient. We plan to do this in future experiments.

We showed with the model that both the NHE and the AE are fundamental for pH_i recovery from acidosis and alkalosis, respectively. However, experiments that used the AE inhibitor DIDS to evaluate the role of the acid loader during recovery from acidosis(induced with an NH_4^+ prepulse) showed that there was no effect on pH_i recovery after AE inhibition, and therefore concluded that the AE did not play a role during acid recovery (122). With our model, we observed the opposite: we found that increased expression of the AE can produce a flat pH_i response to HA. Based on the fluxes produced by the model, we concluded that AE affects pH_i recovery from acid loads mainly by increased rates of bicarbonate removal. These contradictory observations could be the result of regional differences, for example, the NHE was also the only active pH_i regulation transporter in cultivated rat cortical and sympathetic neurons (110), but in cultured hippocampal neurons, both the NHE and AE were active (148).

One problem in testing inhibition of acid-base elements with our model is that reducing the levels of a given transporter (e.g., NHE) changes the baseline pH_i. So, in order to compare simulations with and without inhibition requires that the other pH_i regulation mechanism (in the case of our model, AE) be adjusted so the same baseline pH_i is obtained. This makes comparisons difficult because two parameters have been varied instead of just the mechanism of interest. Thus, it is difficult to rule out the possibility of combined effects. To overcome this limitation, additional H^+ pathways should be incorporated in the model for future simulations. In addition, model parameters have to come ideally from regions of interests, and currently there is not enough experimental data to generate a model based on neurons from chemosensitive and non-chemosensitive regions. As more data become available, we plan to update the model accordingly.

We found that CA affects the initial rate of change of pH_i during HA although its role during pH_i recovery is very limited. Some experiments have suggested that chemoreceptors require CA to speed up the hydration of CO_2 so that the chemosensing elements can detect the signal, presumably pH_i (102, 103). However, the model suggests that the time scale for the acid-base regulation mechanisms is too slow compared to the hydration of CO_2 to actually change the response of these cells during acid challenges. An imbalance of these processes has been suggested in the chemosensitive response in intrapulmonary chemoreceptors in birds (60).

We believe that differences between chemosensitive and non-chemosensitive neurons are an important aspect in elucidating the signals involved in central CO_2/H^+ chemoreception. We speculate that these differences could be due to an imbalance of the acid-base regulation machinery of the cell, and not necessarily to one single element. But whatever the differences, we think they should be incorporated in models that study the electrical response of chemosensitive neurons to increased levels of CO_2. As we showed in the previous chapter and revisited in this one, HA affects cell volume. If HA is "handled" differently by chemosensitive and non-chemosensitive neurons, then the changes in intracellular concentrations of the ions involved are going to be different, and perhaps this could be involved in the sensation process. Furthermore, these changes could influence excitability and may help explain the final ventilation response coordinated by the chemoreceptors. This is the topic of the next chapter.

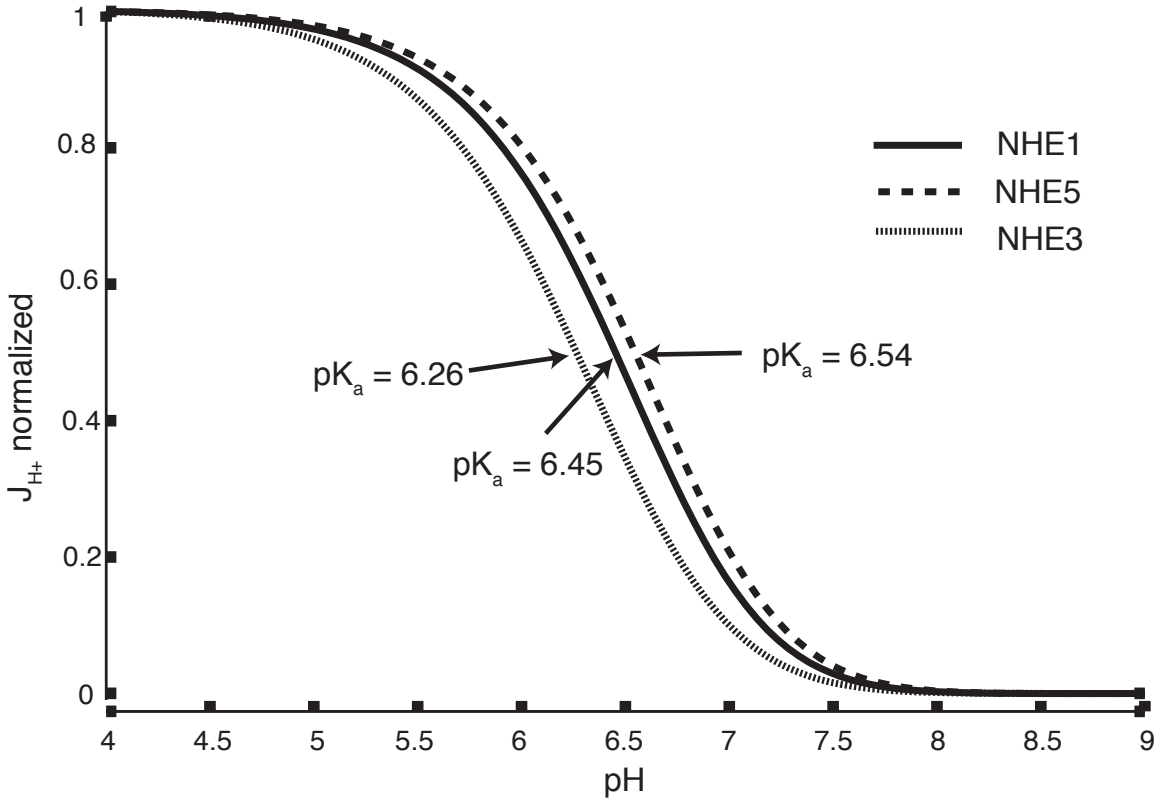

Figure 3.1 Kinetics of NHE1, NHE3, and NHE5 isoforms.

Normalized H^+ flux at different pH levels for three different NHE isoforms. For each isoform, the pK_a is provided. NHE1, solid line (pK_a = 6.45); NHE3, dotted line (pK_a = 6.26); NHE5, dashed line (pK_a = 6.54). Fluxes are normalized for comparison.

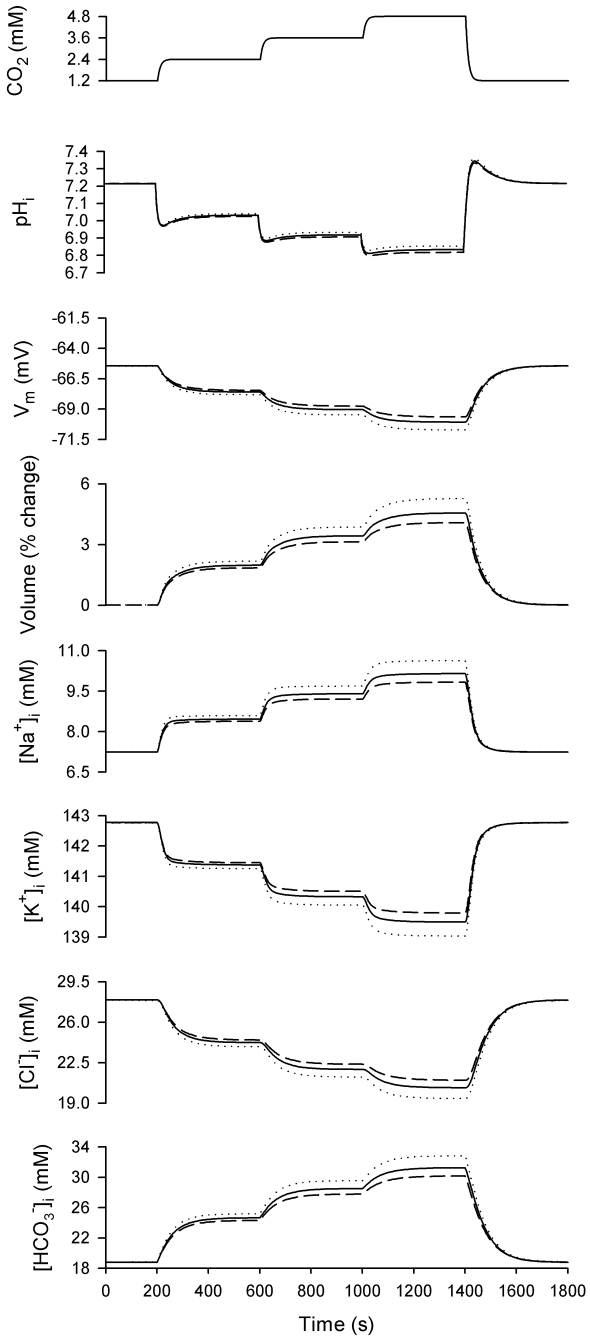

Figure 3.2. NHE isoform and HA.

Influence of NHE isoform on pH_i responses to a series of progressive increases in the concentration of CO_2 from normal levels of 1.2 mM (5%) to 2.4 (10%) to 3.6 (20%) and to 4.8mM (40%). Regardless of the NHE isoform used in the model, progressive increases in CO_2 caused a progressive series of drops in pH_i followed by partial pH_i recovery. Note that differences in the pH_i traces from the different NHE isoforms are minimal, suggesting that differential expression of the three different NHE isoforms is not a sufficient mechanism to explain the difference in pH_i recovery between chemosensitive and non-chemosensitive neurons. Also plotted on the figure are cell volume, membrane potential, and concentrations of Na^+, K^+, Cl^-, and HCO_3^-. NHE1, solid line; NHE3, dotted line; NHE5, dashed line.

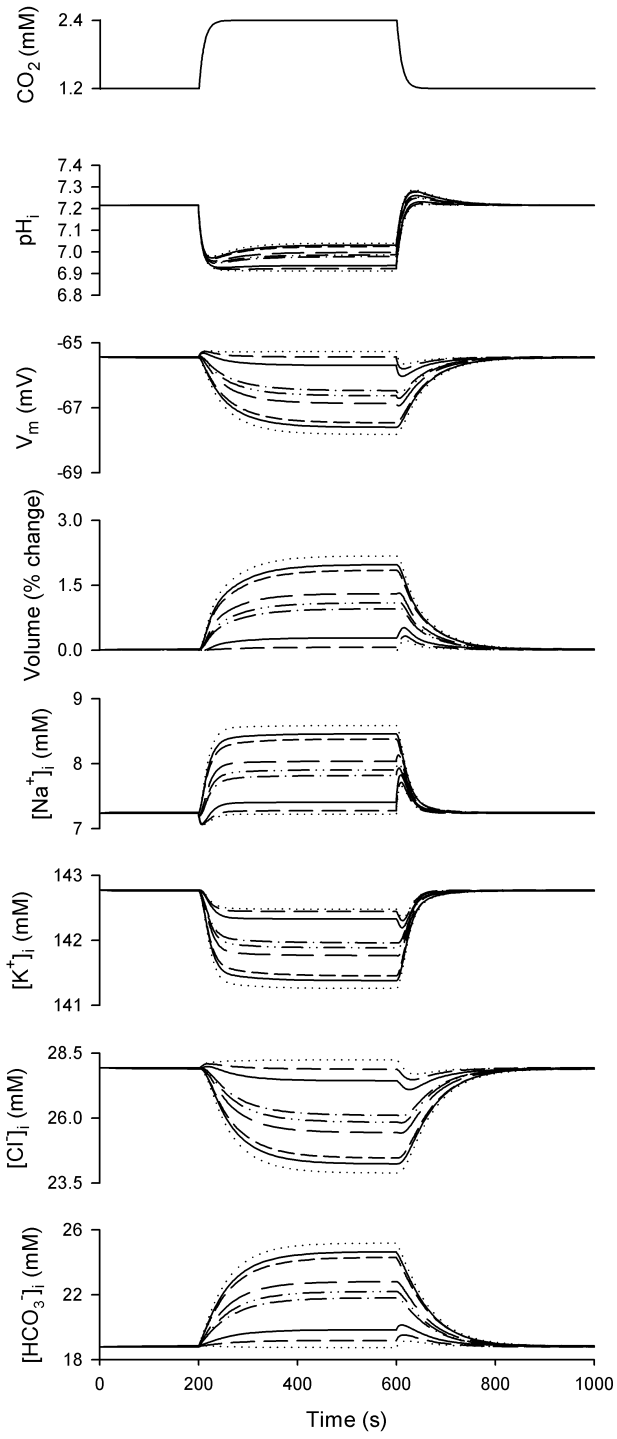

Figure 3.3 NHE is important for pH_i recovery.

Effects of inhibition of NHE activity on pH_i responses to HA for three different NHE isoforms. An increase in CO_2 concentration from 5% to 10% with simultaneous inhibition of NHE (reduction of E_t by 0%, 25%, and 50%) demonstrates the importance of the transporter for pH_i recovery. The results obtained with each one of the isoforms (NHE1, NHE3, and NHE5) are qualitatively the same. Also plotted on the figure are cell volume, membrane potential, and concentrations of Na^+, K^+, Cl^-, and HCO_3^-. NHE1, solid line; NHE3, dotted line; NHE5, dashed line.

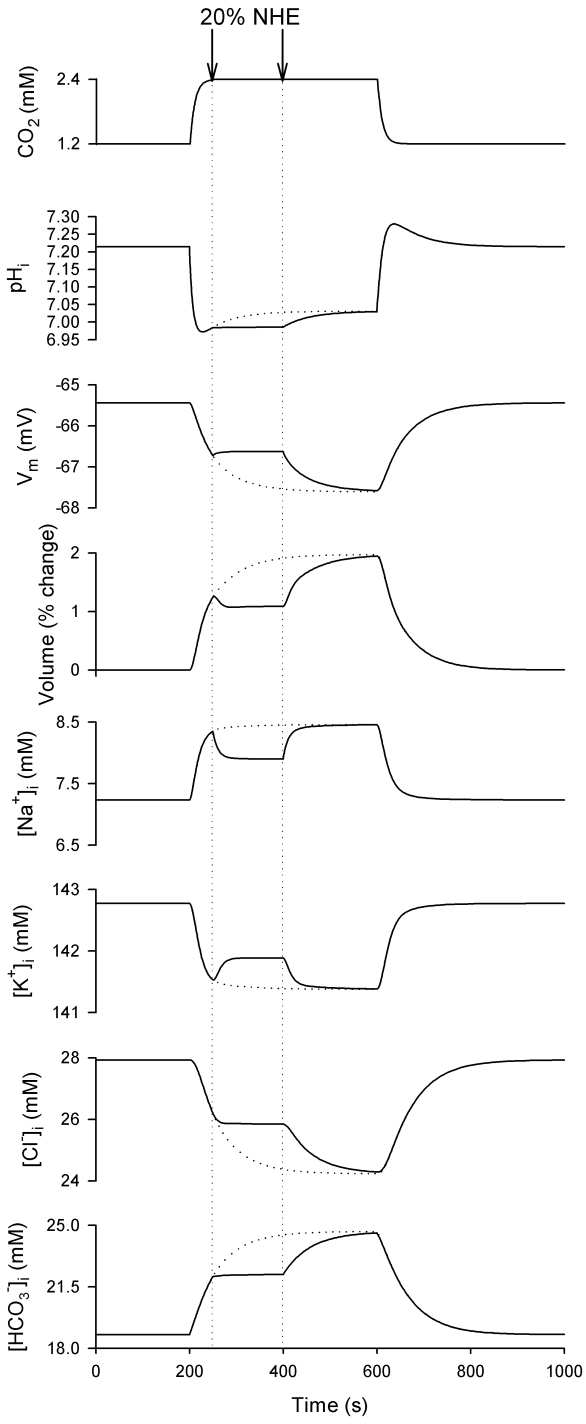

Figure 3.4 Inhibition of the NHE halts the pH recovery process.

Amiloride is commonly used to inhibit the NHE and determine its importance in pH_i regulation. The model captures the effects of applying amiloride (80% inhibition of the NHE) and shows an abrupt change in the recovery slope under HA. Removal of the inhibition brings pH_i back to the predicted trace without inhibition (solid line). Also plotted on the figure are cell volume, membrane potential, and concentrations of Na^+, K^+, Cl^-, and HCO_3^-.

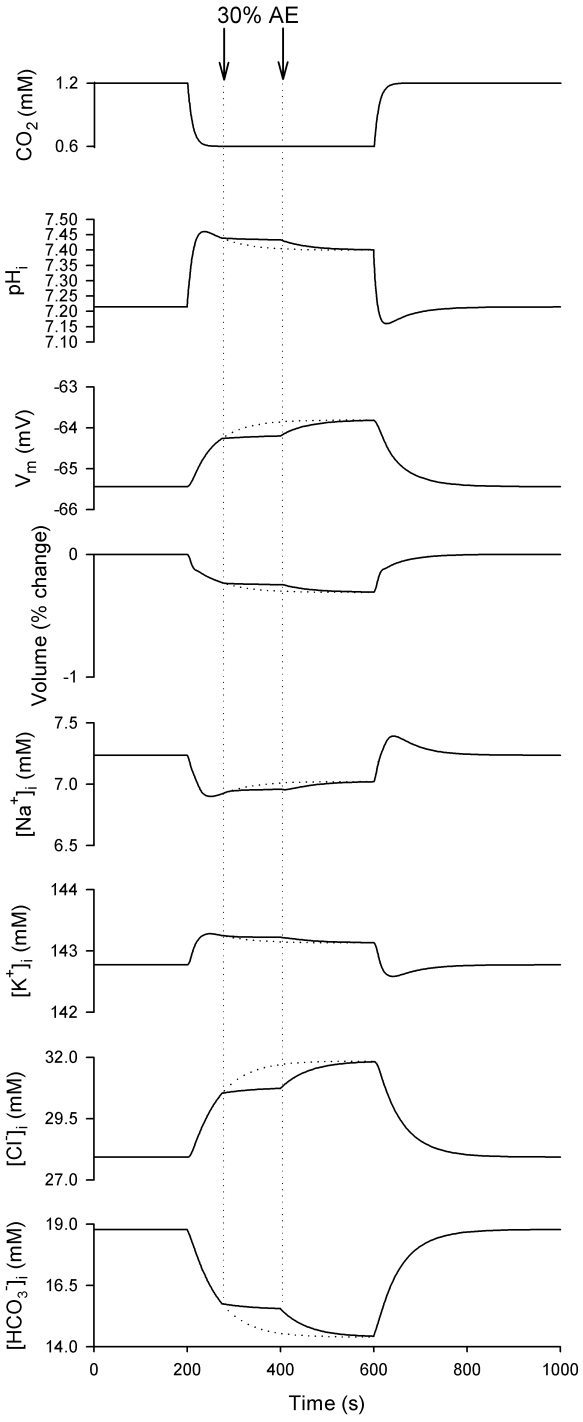

Figure 3.5 Inhibition of the AE halts the pH recovery process.

DIDS is commonly used to inhibit the AE and determine its importance in pH_i regulation. The model captures the effects of applying DIDS (70% inhibition of the AE) and shows an abrupt change in the recovery slope under hypocapnic alkalosis (2.5% CO_2). Removal of the inhibition brings pH_i back to the predicted trace without inhibition (solid line). Also plotted on the figure are cell volume, membrane potential, and concentrations of Na^+, K^+, Cl^-, and HCO_3^-.

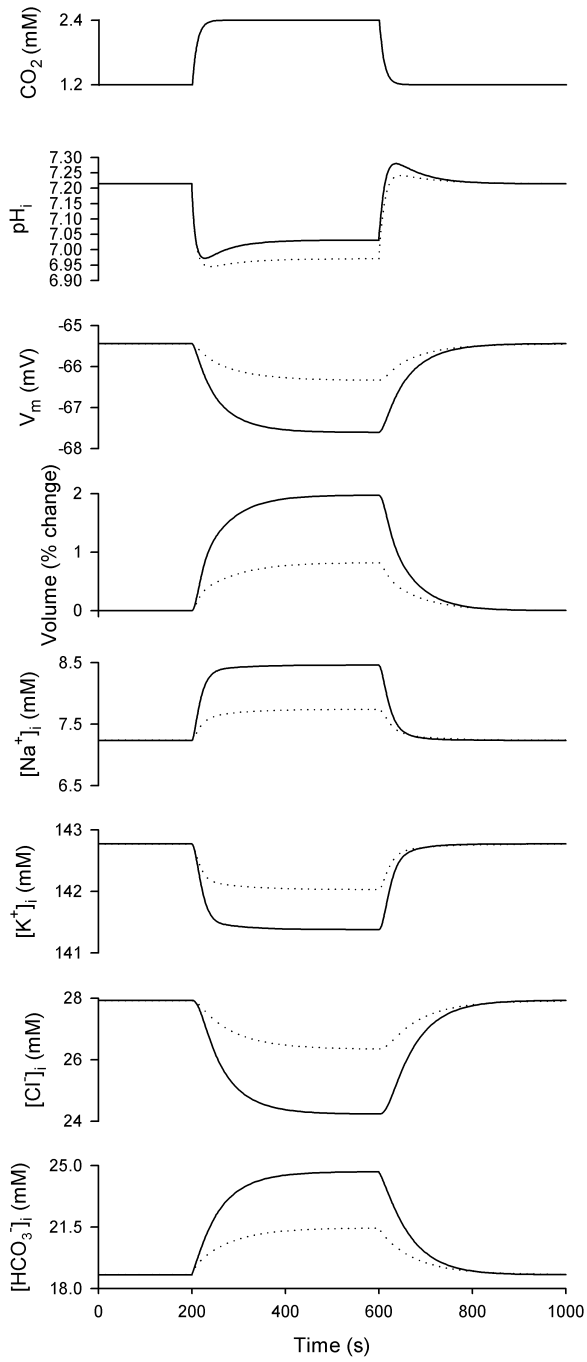

Figure 3.6 pH recovery during HA in Chemosensitive and Non-chemosensitive neurons.

Influence of internal pH sensitivity of the NHE on the pH_i recovery response to HA. To test the possibility that the behavior of chemosensitive neurons to HA results from a NHE that is less sensitive to internal pH, the affinity of the enzyme to H^+ inside was set to a low level (dotted line - chemosensitive neuron). This maneuver yields pH_i recovery during HA that is less steep than that observed in neurons with normal sensitivity levels (solid line - non-chemosensitive neuron). Also plotted on the figure are cell volume, membrane potential, and concentrations of Na^+, K^+, Cl^-, and HCO_3^-.

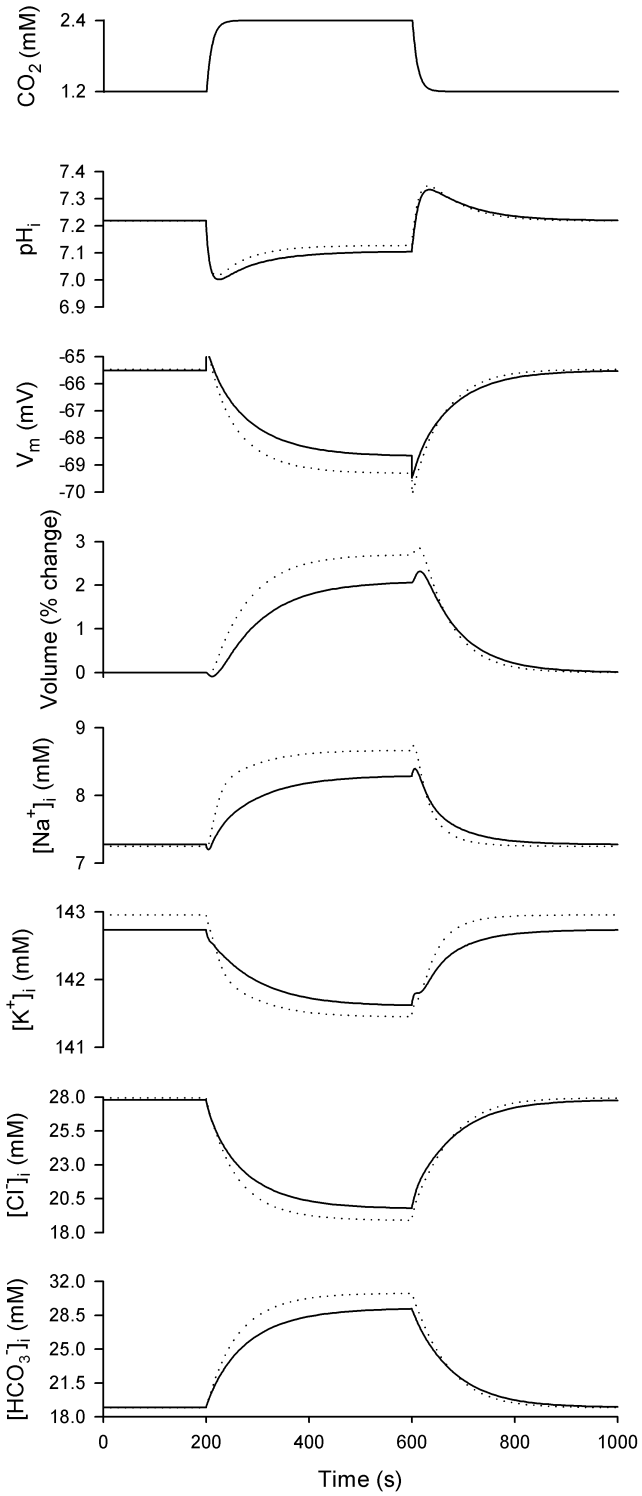

Figure 3.7 pH recovery during IH in Chemosensitive and Non-chemosensitive neurons.

In contrast to the simulation with HA, isohydric hypercapnia (10% increase in CO_2 with pH_o constant) causes both chemosensitive (dotted line) and non-chemosensitive neurons (solid line) to recover from an acid load. Also plotted on the figure are cell volume, membrane potential, and concentrations of Na^+, K^+, Cl^-, and HCO_3^-.

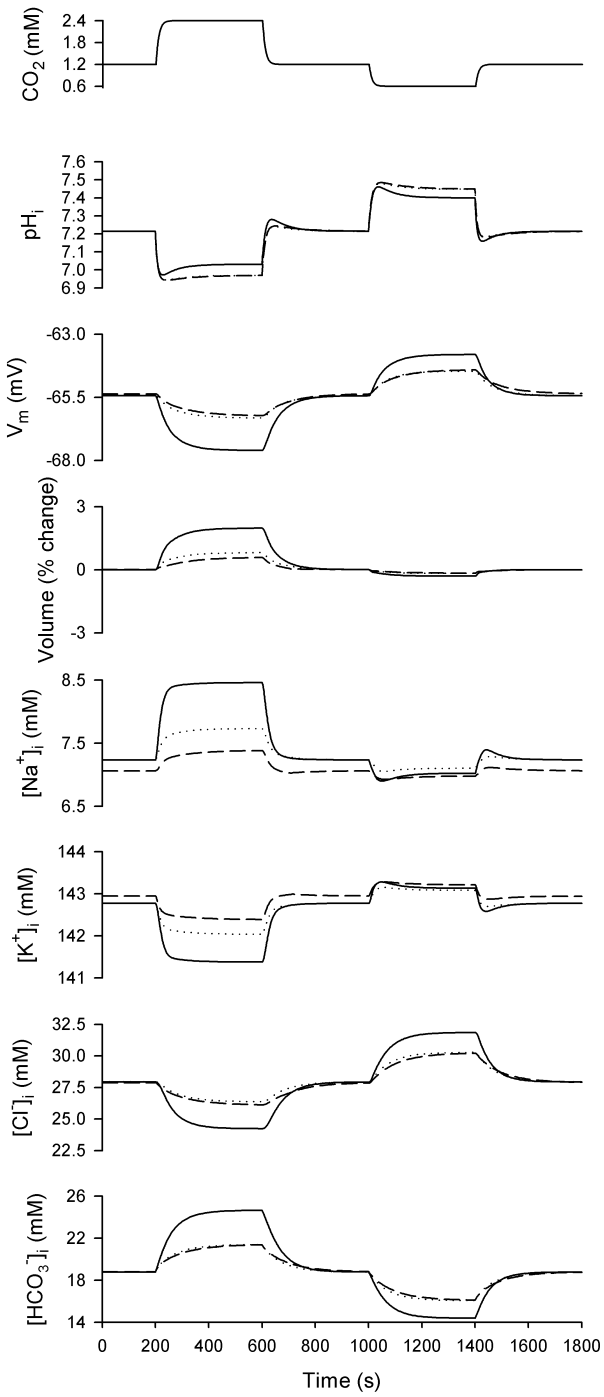

Figure 3.8 pH recovery during HA in Chemosensitive (VLM vs. NTS) and Non-chemosensitive neurons.

The behavior of chemosensitive NTS neurons (AE inhibited 70%) and VLM neurons (no inhibition of AE) to HA and hypocapnic alkalosis was compared to that of non-chemosensitive neurons (solid line). Both NTS (dashed line) and VLM neurons (dotted line) show the same blunted pH_i recovery response during HA, but VLM neurons show a slightly faster and larger recovery from hypocapnic alkalosis. Also plotted on the figure are cell volume, membrane potential, and concentrations of Na^+, K^+, Cl^-, and HCO_3^-.

Table 3.1 Model Parameters

Parameters	Non-chemosensitive neuron	Chemosensitive neuron
Sodium Hydrogen Exchanger (NHE1)		
E_{NHE} (Total amount of transporter)	0.5	0.25
p_H (sensitivity to pH_i)	High ($f_M = 2$ and $k = 1.78\times10^{-4}$)	Low ($f_M = 1$ and $k = 0$)
Sodium Bicarbonate Exchanger (AE)		
E_{AE} (Total amount of transporter)	1×10^{-8}	1×10^{-8}
Na^+ - K^+ ATPase		
Maximum pump rate	40	40
Carbonic Anhydrase		
k_h/k_d	180/64000	180/64000
Cl^- currents		
$E_{NKCC}(E^{MIN}_{NKCC} - E^{MAX}_{NKCC})$	1.9×10^{-5} - 1×10^{-3}	1.9×10^{-5} - 1×10^{-3}
$E_{KCC}(E^{MIN}_{KCC} - E^{MAX}_{KCC})$	5×10^{-11} - 5×10^{-6}	5×10^{-11} - 5×10^{-6}
Concentrations		
C^i_{Na} mM	7	7
C^i_K mM	142	142
C^i_{Cl} mM	27	27
pH_i - pH_0	7.2 –7.4	7.19 –7.4

Table 3.2 Parameters for the NHE isoforms

Model Component	NHE1	NHE3	NHE5
Sodium Hydrogen Exchanger (NHE)			
E_{NHE} (Total amount of transporter)	0.5	0.88	0.375
p_H (sensitivity to pH_i)	High	High	High
pK_a	6.45	6.26	6.54

Table 3.3 Parameters used to simulate experimental perturbations

Parameter	NHE Inhibition (0% 25% - 50%)	Amiloride (80% Inhibition)	DIDS (70% Inhibition)	NHE sensitivity to pH_i
E_{NHE}	0.5 – 0.375 – 0.25	0.1*	---------	---------
E_{AE}	---------	---------	3×10^{-9}	---------
f_M and k (NHE)	---------	---------	---------	(f_M=1 and k= 0)

*value for non-chemosensitive neuron, the chemosensitive neuron is adjusted by the same amount.

Table 3.4 Parameters for VLM an NTS neurons

Model Component	VLM	NTS
Sodium Hydrogen Exchanger (NHE)		
E_{NHE} (Total amount of transporter)	0.245	0.075
p_H (sensitivity to pH_i)	Low (f_M=1 and k= 0)	Low (f_M=1 and k= 0)
Chloride Bicarbonate Exchanger (AE)		
E_{AE}(Total amount of transporter)	1×10^{-8}	3×10^{-9}

Chapter 4 - The transport-excitable model

4.1 Introduction

The constant movement of air in and out our bodies is without doubt what defines us to be alive. This movement, known as respiration, is important to maintain constant levels of CO_2/H^+ that guarantee that biological processes take place at the cellular level. A variety of cells in our body respond to changes in CO_2/H^+, known as chemosensitive cells, like renal proximal tubule cells involved in acid base regulation (156), taste receptors cells that sense acid on our tongue (130), and nociceptors for pain reception (143), just to mention a few. But specialized sensors that detect changes in CO_2/H^+ and are involved in respiration are known as respiratory chemoreceptors, and they are a primary component of the ventilatory response. Two sets of respiratory chemoreceptors have been identified in mammals, glomus cells in the carotid body (peripheral chemoreceptors) (53) and neurons localized within various regions of the brainstem (central chemoreceptors) (97).

For a neuron to be classified as a putative central respiratory chemoreceptors (CRC), it needs to meet three criteria: 1) they have to intrinsically respond to changes in CO_2/H^+, 2) they have to project to neurons involved in breathing, and 3) they have to ultimately modulate breathing (110). Surprisingly, despite an extensive amount of research, we have only candidate neurons to be CRC, but not a single one has been proven to meet all three requirements in mammals (110). Regardless, considerable progress has been made in characterizing the cellular mechanisms involved in central CO_2/H^+ chemoreception (topic 1), which has benefited from reduced preparations while the remaining two topics require more intact preparations.

The response to an increase in CO_2/H^+ or hypercapnic acidosis (HA) can be an alteration of a cellular transport process, like seen in the renal proximal tubule cell that increases HCO_3^- in response to HA (156), or changes in firing rate (FR) that are only possible in excitable cells. Both peripheral and central respiratory chemoreceptors are excitable cells, and they respond to HA by increasing or decreasing their firing rate, which allows them via synaptic connections to alter ventilation (117). In response to HA, these excitable cells presumably alter cellular transport processes, but no specific transport mechanism has been identified for mediating thier responses, thus far. Central CO_2/H^+ sensitive neurons have been demonstrated in the nucleus tractus solitarius (NTS) (35), medullary raphé (116), locus coeruleus (LC) (105), nucleus ambiguus (125), and the ventrolateral medulla (VLM) (13) in synaptically isolated preparations exposed to high levels of CO_2.

The first main theme in studies of central CO_2 chemoreception is the identification of the signal(s) responsible for the changes in FR and subsequent modulation of ventilation. An increase in CO_2 produces a decrease in intracellular

pH (pH_i), a decrease in extracellular pH (pH_o), an increase in intracellular bicarbonate ($HCO_3^-{}_i$), and an increase in extracellular bicarbonate ($HCO_3^-{}_o$), and therefore, each one of these signals or a combination of them (i.e., pH_i - pH_o gradient) is a potential candidate to be the primary stimulus. In fact, to date, all of these elements have been proposed as important players for CO_2/H^+ sensitivity (110). For example, Filosa and colleagues measured changes in pH_i, CO_2, HCO_3^-, and pH_i - pH_o gradient using a technique to measure pH_i and membrane potential simultaneously in neurons from the LC, and found that only the magnitude of the increase in pH_i correlates well with the magnitude of increase in FR (46). Thus, despite the lack of unanimous agreement there is accumulating evidence in favor of pH_i as the primary stimulus (25).

The second theme in central CO_2 chemoreception is the poor regulation of pH_i in response to HA in neurons from chemosensitive areas. The first demonstration of this behavior was obtained by Ritucci and colleagues when they studied the pH_i response to HA in neurons from two chemosensitive areas (the NTS and the VLM) and two non-chemosensitive regions (the inferior olive (IO) and the hypoglossal motor nucleus) in medullary slices from neonatal rats (122). They found that neurons from the chemosensitive regions acidified and remained acidic for the duration of the CO_2 stimulus while neurons from the non-chemosensitive regions showed pH_i recovery during HA (122). Accordingly, they suggested that neurons from chemosensitive areas have a Na^+-H^+ exchanger (NHE) that is far more sensitive to changes in pH_o than the NHE found in neurons from non-chemosensitive regions (122). A subsequent study by Nottingham and colleagues, however, demonstrated that the lack of pH_i recovery during HA may be a function of development since neurons in non-chemosensitive medullary regions show no pH_i recovery during HA in slices taken from from older animals (104).

The final theme in central CO_2 chemoreception is the transduction of the signal into a change in FR, or the sensory process. Different regions of the brainstem exhibit different patterns of response to increased CO_2/H^+. While some putative chemosensitive regions contain a large percentage of neurons that increase FR when exposed to HA, other regions contain a small proportion of excited neurons, and in some cases, even inhibited neurons. For example, in the LC greater than 80% of the neurons studied respond to HA, and all of them increase their FR (109). In contrast, in the dorsal medulla, only 50% of the neurons studied respond to HA, and half of them increase their FR while the other half decrease their FR (110). Additional studies have reported that 1) neurons from the medial caudal retrotrapezoidal nucleus (mcRTN), which exhibit tonic spiking at rates of ~1 Hz, increase their firing rate to 4 Hz during HA *in vitro* (123), 2) neurons in organotipic cultures of the medulla from the level of the obex exhibit enhanced bursting during hypercapnia compared to normal levels (146), and 3) some populations of neurons from chemosensitive areas decrease FR or show no change during HA (124).

In summary, is not only the kind of response (increase, decrease, or no change in FR) but also the type of activity (spiking or bursting) that is spatially variable. Some reports suggested that the increase in FR is probably modulated by the inhibition of a positive current that causes the depolarization and subsequent increase in FR. The most common alternatives that support this hypothesis include inward rectifying K^+ channels (K^+_{ir}), Ca^{++}-sensitive K^+ channels (K_{Ca}), and pH-sensitive K^+ channels (TASK). But other options include voltage-sensitive Ca^{++} and voltage-sensitive K^+ (35, 47, 107).

Based on these observations, one might notice that the three themes are not independent from each other. These themes represent areas of ongoing investigation and a number of hypotheses that have been put forth. Yet, there is no consensus in the field regarding what signal is being sensed and how the signal is converted into a excitable cell response. In fact, one possibility suggested by the data is that chemosensitive neurons rely on pH_o to maintain the primary stimulus -pH_i- at a low level so pH-sensitive channels become activated and the neuron increases its FR. However, the level of pH_i does not always seem to be correlated with changes in FR. For example, hypoxia-induced intracellular acidification does not cause an increase in ventilation (155). Additionally, in an experiment in which the pH_i was clamped by simultaneously adding the weak base trimethylamina (TMA) with an increase in CO_2, a dramatic increase in FR but only a small change in pH_i was noted (110). The authors concluded that TMA caused the depolarization, and therefore, the treatment could not be used to asses the effects on FR. These controversies prompted the formulation of a multiple factor model for central CO_2 chemoreception that includes multiple signals, multiple targets (transduction elements), and the response (110).

A multifactor model lends itself to mathematical modeling.Surprisingly however, to our knowledge, only the work of Chernov and colleagues has used a mathematical model to investigate CO_2 chemoreception (25). The model is based on a Hodgkin and Huxley (HH) single compartment formalism, and it includes estimates of acid-base regulation fluxes to investigate CO_2 chemoreception in the snail *Helix aspersa*. The model focuses on the signals involved in CO_2 chemoreception and assumes that the transduction mechanisms are pH-sensitive K^+ currents. Such a model, however, does not incorporate the differences observed in chemosensitive neurons (i.e., their poor pH_i regulation) or kinetic descriptions of acid-base regulation components, and it incorporates formulations for the different channels that have been identified in the snail, from a variety of sources that do not necessarily participate in CO_2 chemosensitivity in mammals, and therefore, may only be applicable to invertebrates.

We decided to expand these ideas and investigate the problem of CO_2 chemoreception also using a mathematical model that approaches the problem from a unified perspective. In other words, we wanted to build a model that incorporates the main signals, the lack of pH_i regulation in chemosensitive neurons, and cell excitability in one single unit. We envisioned this model as a combination of a transport model (already introduced in chapter 2 and validated

in chapter 3), and an excitable cell model (as the one used by Chernov and colleagues (25). However, before assuming a complicated set of currents involved in the process, and based on our preliminary results using the transport model, we decided to investigate first the possibility that the response of central CO_2 chemoreceptors is the result of a delicate modulation of the neuron firing properties by the slow and transient changes produced by transport phenomena involved in pH_i regulation during HA. This means that we reduced the repertoire of currents postulated to be involved in CO_2 chemosensitive neurons to just two, fast sodium (I_{Na}) and the delayed rectifier potassium (I_K). Both of these currents are pH insensitive in our model, and provide the minimum ability for generation of spiking behavior and no direct link between changes in pH and conductance. Using this approach would mean that we would have to defer the addition of inward rectifying K^+ channels, Ca^{++}-sensitive K^+ channels, and TASK channels to a future version of the model, as we believe these channels may participate in central CO_2 chemoreception.

The first challenge that we had was that our transport model relies on the Goldman-Hodgkin-Katz (GHK) equation (28, 52, 65) to compute ionic flux, and the typical excitable HH model (66) relies on conductance to describe ionic current. Instead of mixing these two approaches (i.e., having a transport compartment based on permeabilities and an excitable compartment based on conductance), we decided to convert a HH model into an excitable cell model based on the GHK formalism. This decision was mainly based on the idea that the GHK normalization of I_K and I_{Na} was carried before by several authors (28, 94) under the notion that the expression accounts for non-linearities in the I-V relation and that this is a better description of fully activated currents when the difference in ionic composition is significant across the cell membrane.

To accomplish this, we used a conductance-based HH model with parameters for I_{Na} and I_K taken from published models from brainstem neurons (22, 36) to generate simulated voltage clamp experiments that were fitted using a similar model that implemented the GHK normalization. In addition, dynamical systems analysis was used to corroborate that both models are topologically equivalent (e.g., have the same dynamic response to a comparable perturbation) and that they reflect the dynamics observed experimentally in real neurons.

The next step was to integrate the transport and the excitable cell models. To accomplish this, we decided to use a sequential approach. Instead of adding all of the elements already described in our transport model (chapter 2) at once, we decided to add the elements one at a time so we could better understand the effect that each one of the components had on the excitability response. We started by adding passive diffusion for Na^+, K^+, and Cl^- and a voltage-sensitive kinetic description of the Na^+/K^+-ATPase (87). At this stage, we evaluated the role of the Na^+/K^+-ATPase in maintaining normal levels of Na^+ and K^+ during tonic spiking and the role of Cl^- in generating steady-state spiking behavior.

Also based on our previous observations, we noted that cell volume due to Cl^- accumulation is a common problem in models studying an osmotically active

perturbation like HA. Therefore, we used our previous descriptions of the two Cl^- sensitive cell volume regulation cotransporters to amend the model. For this, we added kinetic descriptions of the Na^+-K^+-Cl^- cotransporter (NKCC) (90) and K^+-Cl^- cotransporter (KCC) (90).

Finally, we added an acid-base regulation component that uses HCO_3^- as the main player for pH_i buffering. The pH component includes passive diffusion for HCO_3^-, catalytic properties of carbonic anhydrase (CA), which are reflected in the hydration/dehydration rate of CO_2, and the kinetics of the NHE as an acid extruder and the Cl^-/HCO_3^- exchanger (AE) as an acid loader. We used this more comprehensive configuration of the model to compare the response in FR of chemosensitive and non-chemosensitive neurons as defined by their pH_i regulation response to HA while different elements of the acid-base regulation component were varied.

Within the model, we tried to address the following issues: 1) the optimal permeability of each channel to support excitability; 2) the optimal levels of transport activity that support cellular homeostasis and excitability; 3) the role of Cl^- in steady-state firing; 4) the role of voltage-gated and passive currents in the response to HA; and 5) the role of acid-base regulation in modulating the FR response to HA.

4.2 Implementation of a permeability-based Hodgkin and Huxley formalism

More than 40 years ago, Hodgkin and Huxley developed their model for squid axon excitability, and since then, the model has been used as a framework for virtually every quantitative description of neuronal excitability. The model itself is a remarkable tool, but care must be taken when using the model outside of the context that it was developed for. The model captures the main features of the squid axon action potential, and its validity has been widely accepted; however, two disadvantages to this approach are that ionic flow generally does *not* adhere to the linear I/V relation implied by the equation describing ionic current, and that conductance is proportional to permeability but also a function of membrane potential as well as the intracellular and extracellular ion concentrations. In addition, incongruences between model predictions and electrophysiological features of the squid axon membrane have been reported (29). Moreover, the model is less suitable for non-invertebrate electrophysiology due to differences in membrane composition (29). These considerations prompted us to reformulate the model in the same terms that we formulated our transport model (see chapter 1 and the appendix). In the permeability-based formulation, the fluxes are described by ion permeability (*P*) *not* conductance; therefore, we have a more realistic nonlinear flux relationship. Also, the new formulation provides a means to simulate experimental perturbation where concentrations change significantly (e.g., NH_4^+ substitution, elevated K^+). In addition, it has been observed experimentally that the fully activated current-voltage (I-V) relationship of the Na^+

(I_{Na}) and K^+ (I_K) currents have a nonlinear dependency on the driving force (V-E), an observation that is well represented by the GHK equation (30). Here, we describe our method to transform a HH conductance-based model into a GHK permeability-based excitable cell model (permeability-based model) that retains the same geometrical features as the original. As a result of this approach, the model has the same overall behavior, but adheres better to fully activated I-V relations and overcomes the limitation imposed by using conductance and the range of ionic gradients that can be tested.

4.2.1 *Model description*

Our models, like a typical HH formalism, include a Na^+ voltage-dependent current (I_{Na}) with activation and inactivation kinetics, where the activation component is described by the cubic function $m^3(V)$ where m is the activation gate; similarly, the inactivation component is described by a function $h(V)$, where h is the inactivation gate. The model also includes a K^+ voltage-sensitive current (I_K) that has only an activation component, described fourth power function n^4(V), where n is the activation gate. In addition, the model implements a voltage-insensitive leak current dominated by K^+. However, our version departs from more typical HH formalism in that first the activation gate (m) is assumed to be instantaneous and described by the steady-state activation function m_∞ , and the time course of the inactivation gate (h) is assumed to be a linear function of activation gate for K^+ (n) and described by $h = 1\text{-}n$. (120). In addition, the leak current has been partitioned into two components, one carried by K^+ ($I_{K,l}$) and one carried by Na^+ ($I_{Na,l}$). Figure 4.1 shows the elements of the model, and Appendix A.2 gives presents the model equations.

The assumptions described before are the minimal configuration for realistic spiking behavior but they reduce the complexity of the model allowing for easier variable manipulation while giving reasonable voltage membrane dynamics. Additional voltage- and Ca^{++}-gated currents are the subject of future studies (see discussion section), and we restrict our analysis here to this minimum formulation knowing that this surely is an over simplification of the cellular mechanisms for central CO_2 chemoreception, but it constitutes the first attempt to dissect the effects of the transport component of the neuron's membrane dynamics and we preferred simplicity as a first approximation.

4.2.3 *Model parameters*

The parameters for the HH model are listed in Table 4.1, and they were taken from Butera and colleagues (1999) and Del Negro and colleagues (2001) and reflect typical membrane currents for brainstem neurons. For the permeability-based model, however, there are no reports of voltage-gating activation kinetics and permeabilities of the different ionic species. Therefore we had to develop a technique to identify appropriate parameters and test them to corroborate that both models have similar dynamic behavior and adhere to experimental observations. To evaluate the dynamic behavior, we implemented two

techniques, the first one uses currents generated with the HH model in a manner similar to a voltage-clamp experiment to find the set of parameters appropriate for the same current in the permeability-based model via minimization algorithms. The second technique involves dynamical systems analysis of the two models to further adjust parameters when all of the individually fitted currents were put together back in the permeability-based model.

4.4.4 Fitting simulated voltage clamp experiments

Our initial approach was to fit simulated voltage-clamp experiments using the HH model as the data and the permeability-based model as the fitting function. Permeability and the (in)activation parameters for m and n (τ_m, $\theta_{m,}$ τ_n, θ_n and $\tilde{\tau}_n$), need to be determined for each current in the permeability-based model, and we assumed physiologically reasonable values for intracellular and extracellular concentrations for each ion (the values can be seen in Table 4.5) without restraining the solutions for reasonable dynamical behavior (but we test this later in the dynamical systems approach section). We fitted each current separately, assuming the voltage gating behaves as described in model assumptions for both the generation of the data points and the posterior fitting using the GHK version of the gated current. The Nelder-Mead algorithm was used to find the best fitting set of parameters; relative and absolute tolerance was set $1x10^{-4}$.

We start by finding the parameters for the fast Na^+ current. The initial step was to generate a series of simulations in which we held the membrane potential constant at a hyperpolarized level so all of the activation gates are closed. We then increased V in steps to a greater value and held it until the current reached its steady-state. By repeating the step for various potentials one can determine the parameters by applying the optimization algorithm. Figure 4.3 shows the results of the fitting routine and Table 4.2 shows the initial guess values for the parameters and their final results after the optimization. The same process was repeated for the delay rectifier K^+ current (Figure 4.4 and Table 4.3) and the leak currents (Figure 4.5 and Table 4.4)

As can be seen from Tables 4.2, 4.3, and 4.4, the changes in the parameters for the voltage-gated particles, m and n are small compared to the initial values which are the original parameters. In fact leaving the same numbers and doing the fitting just for permeability produces similar results as the ones shown on Figures 4.3 and 4.4 (same over-all error). Therefore, the critical value is the permeability. We proceed with our model using the original parameters for the gating variables so we do not have to assume the existence of channels with new voltage gating kinetics; this is attractive not only for simplicity but it also reduces the number of parameters that have to be estimated to get physiological behavior. Table 4.5 shows the selection of the parameters for the permeability-based model after the voltage-clamp simulations.

4.2.5 Testing the validity of the model parameters

The question that remains to be answered is whether the values that we obtained for the permeabilities produce a model that has the same dynamical response as the HH model, and the answer is no. When we integrate the models under no applied current (I_{app} = 0), both models exhibit a steady-state characterized by quiescence. However, there is a big difference in resting membrane potential, the HH model is resting at -62 mV while the permeability-based model is resting at -47 mV (see results in Table 4.6). The permeability-based model has a depolarized level probably as a result of an imbalance of the leak currents. In addition, when an equivalent applied current (48 pA for the HH model with total cell capacitance of 21pF and 1 $nC \cdot cm^{-2} \cdot ms^{-1}$ for the permeability-based model with a capacitance per unit are of $1 \mu F \cdot cm^{-2}$) is present in both models, the permeability-based model exhibits higher firing rates and smaller spike amplitudes compared to the HH model. These results suggested that the $P_{Na,l}$ was set to high and $P_{K,l}$ too low, and the opposite for P_{Na} and P_K. So additional adjustments are needed to have an equivalent model from a dynamical perspective. Before we attempt to modify the model parameters; however, we briefly cover some of the basic theory for studying dynamical systems, and use this approaches to revise the permeability-based model.

Dynamical systems approach to fine tune parameters

To adjust the behavior of the permeability-based model, to be as similar as possible to that of the HH model, we implemented geometrical analysis. We used the fact that both models are two-dimensional (2D) systems, which are amenable for some techniques commonly used in dynamical systems analysis. The first step is to construct the phase-portrait of the system for both models and modify the parameters so they exhibit a topological equivalent phase portrait (this concept is defined by (55)). The second step is to modify the parameters so both systems can exhibit the same kind of bifurcation from steady-state, the same kind of overall stability (bistable or monostable), and the same class of neural excitability (69). Briefly, the phase portrait contains the nullclines for the two state variables *V* and *n,* and they represent the set of points where the vector field changes its direction. Each point of intersection of the nullclines is an equilibrium point (3 in the phase portraits shown in Figure 4.6), and the vector field (arrows) provide information about the joint evolution of the state variables. The equilibrium points can be stable or unstable; their stability determines whether a trajectory (a solution of the 2D system starting with some initial conditions) will approach or diverge to/from the equilibrium point.

The Hartman-Grobman theorem states that the dynamics of a nonlinear system can be approximated by the dynamics of the system that results after linearization of the original system near an equilibrium point (provided that the equilibrium point is hyperbolic, see Izhikevich (2007) for a detail discussion of linearization equilibria of dynamical systems). The linearization of the system close to the equilibrium produces a matrix, known as the Jacobian of the system

at that particular point. The Jacobian matrix at the equilibrium provides all the information necessary to classify the stability of the system at the equilibrium point. Thus, to understand and classify the geometry of the vector field of the linear system will allow for understanding and classification of the geometry of the nonlinear system close to the hyperbolic equilibrium.

The eigenvalues of the Jacobian matrix at the equilibrium are sufficient to classify the kind of point and its stability: **Node**, when the eigenvalues are real and with the same sign; the point is stable if the eigenvalues are negative and unstable if they are positive. **Saddle**, when the eigenvalues are real and with opposite sign, saddles are always unstable. **Focus**, when the eigenvalues are complex-conjugate, foci are stable when the real part of the complex are negative and unstable when they are positive. A zero eigenvalue makes the equilibrium non-hyperbolic and the linearization is no longer a good approximation of the nonlinear system. Usually dynamical systems have zero eigenvalues at their equilibrium when they are undergoing a bifurcation.

A bifurcation or a transition from resting to periodic spiking usually involves the disappearance or loss of stability of the stable equilibrium. Codimension-1 bifurcation (one that can be observed by changing one parameter in the model) can be grouped into four classes: 1) **saddle-node**, 2) **saddle node on invariant circle**, 3) **subcritical Andronov-Hopf,** and 4) **supercritical Andronov-Hopf**. The saddle node and saddle node on invariant circle involve the coalition of saddle and node and the existence of a limit cycle; in both types, the equilibrium disappears. In the first one, the node and the limit cycle coexist making the system bistable. In the second an heteroclinic trajectory (one that connects the saddle with the node) precedes the formation of an homoclinic trajectory (originates and ends at the saddle-node) that turns into a limit cycle when the saddle-node disappears. The Andronov-Hopf bifurcations involve the loss of stability of the equilibrium but not its disappearance. The loss of stability is accompanied either by the appearance of a stable limit cycle (supercritical Andronov-Hopf) or by the disappearance of an unstable limit cycle (subcritical Andronov-Hopf).

The systems can also be classified as *bistable* and *monostable* based on the coexistence of a stable equilibrium and a stable limit cycle. Only systems of the saddle-node and subcritical Andronov-Hopf bifurcation exhibit coexistence of a stable equilibrium and a stable limit cycle; therefore, they are bistable. Systems of the type saddle node on invariant circle and supercritical Andronov-Hopf are monostable. In addition, only systems that belong to the Andronov-Hopf bifurcation family exhibit damped oscillations of the membrane potential, whereas systems near saddle-node bifurcations, whether on or off an invariant circle, do not. Neurons with damped oscillations are called *resonators* and those that do not have this property are called *integrators.* (69)

Finally, we can classify the neuron based on its excitability, Hodgkin was the first to suggest a classification criteria based on the type of response to diverse stimulus pulses (65). *Class 1 neuronal excitability* represents neurons that can

vary their FR according to the strength of the stimulus (only saddle node on invariant circle). *Class 2 neuronal excitability* represents neurons that have a relatively narrow FR response to a wide amplitude of stimuli. Class 3 neuronal excitability represents neurons that fire once or not at all under arbitrary current strengths.

4.2.6 Putting it all together and defining the permeability-based excitable cell model

We know based on the dynamics of model 1 and experimental data that we are looking for a system that bifurcates via saddle node on invariant circle (that guarantees class 1 neuronal excitability). This has the consequence that the system has to be monostable, have a non-monotonic I-V relation, and that at rest has to have a stable node and saddle. The process of adjustment, that is to adjust the permeability-based model parameters to exhibit these characteristics, was simple since both models share the same voltage gating kinetics, and therefore, their steady state I-V relationship was fairly close (which is good predictor of dynamical properties).

To get resting membrane potential close to -62 mV in the permeability-based model and to get similar FR during spiking conditions, it was sufficient to modify the proportion of the leak currents (see Table 4.5 for the parameters). Not surprisingly, the permeability-based model retained the dynamical properties identified in the HH model; we confirmed this by comparing their geometrical properties and by corroborating that their phase-portrait is topologically equivalent. Figure 4.6 compares their phase-portraits under no applied current and under an equivalent depolarizing stimulus after the change in the leak permeabilities (the intermediate steps to get to the finals values are not shown for brevity). In addition, the time course of the membrane potential of two different levels are shown to compare their dynamical responses (FR) and to corroborate class 1 neuronal excitability. Figure 4.7 compares the steady-state I-V relation of both models before and after geometrical analysis to show the improved agreement after changing the aforementioned parameters.

Both models now have the same overall behavior under applied currents, but the permeability-based model accommodates for non-linearities in the I-V relation. Experimental simulations that show the effect of the different formulations are out of scope for this manuscript and they include some drastic dynamical divergences. For a better understanding of the effects in excitability that this normalization produces, see Clay (28), and for a brief comparison between conductance and the GHK expression to compute ionic flux see Cordovez et al. (34).

4.3 Adding transport mechanisms to the permeability-based model

The permeability-based excitable cell model developed in the previous section is dynamically equivalent, at least for the perturbations tested so far, to the HH model, but the permeability-based model implementing the GHK equation for ionic currents is more amenable for integration with transport phenomena that is also described by the GHK equation. Our goal for this section is to expand the permeability-based model and incorporate transport mechanisms already defined in previous chapters to arrive to a comprehensive and fully integrated transport-excitable cell model. We divided this process into 3 main steps, for clarity, and to have more control over the parameters and their relative importance for model stability and to qualitatively describe the effects of the newly added components on cell excitability. Each step will add to the previously defined and tuned up revision of the permeability-based model described in each step. The three steps are:

1. addition of main ionic species, Na^+, K^+, and Cl^- and the Na^+/K^+ ATPase.

2. addition of Cl^- pathways for stable tonic spiking and volume regulation.

3. addition of pH regulation component (transport-excitable cell model).

For simplicity and clarity, we ask the reader to refer to previous equations and tables as we only include in the following pages newly introduced variables or parameters and the parameters that needed to be adjusted.

4.3.1 Step 1: passive diffusion of major ions

Many mathematical models that study cell excitability consider passive diffusion of the ions. Among them, cardiac models are particularly complete and typically include an extensive list of voltage-gated channels and active transport (87), that typically includes Na^+, K^+, Cl^-, and Ca^{++}. However, models that study neuronal activity usually rely in the assumption that no significant ion changes are observed during excitation and that is why the Nerst equilibrium potentials are treated as a constant in these models. This is certainly close to the reality for some situations; however, there are perturbations that are not necessarily well fitted by this assumption. For example, HA is an osmotically active perturbation that significantly changes concentration gradients, which need to be taken into consideration (as we repeatedly mentioned in this document). Here, in this model, we decided to include Na^+, K^+, and Cl^- as the active ionic species.

Model description

The first revision of the model included, in addition to membrane potential and activation gate for the K^+ delay rectifier, mechanisms to keep track of intracellular Na^+, K^+, and Cl^-, and the kinetic description of the Na^+/K^+ ATPase. In addition, to maintain intracellular osmolarity (300 mOsm) and electroneutrality, addition of a

non-permeable negatively charged species was necessary; we called this ion X^- (negative charge of -1) and it was included in both the intracellular and extracellular compartments in the model. The elements of the model are shown in Figure 4.8.

The differential equation describing changes in membrane potential was amended to include the current generated by the movement of Cl^- (I_{Cl}) and also the net current of the Na+/K+ ATPase (i_p). I_{Cl} is described by the GHK equation and i_p uses the same model introduced in chapter 2 and described in the appendix.

Changes in cell volume and intracellular ionic composition follow the same analysis presented in previous chapters. Note that changes in intracellular concentration account for movement of ions through all membrane channels whether they are voltage-sensitive or not.

The model is 7-D system of nonlinear differential equations, one for membrante potential, one for the activation gate of fast K^+ channels, one for cell volume, and four that describe changes in intracellular concentration of Na^+, K^+, Cl^-, and X^-.

Model parameters

The addition of passive diffusion and the Na^+/K^+ ATPase requires 7 new parameters and the adjustment of the concentration of Na^+ outside the cell. Cl^- permeability was guessed to be somewhere in between $P_{Na,l}$ and $P_{K,l}$ and one that gives reasonable concentrations of the ion. C^o_{Na} was increased to 145 mM, so in addition to C^o_K they match the concentrations of the negatively charged particles and generate and electroneutral environment. The maximum amount of current through the Na^+/K^+ ATPase was set so the intracellular concentrations of Na^+ and K^+ stay at a normal level, the half saturation concentrations for Na^+ and K^+ in the pump were used as defined by the original implementation by Luo and Rudy (87). The parameters are shown in Table 4.8.

Numerical integration of model and fine tuning of the parameters

Table 4.9 shows the results of numerically integrating the model with two sets of parameters. The first simulation, simulation 1 on first column of Table 4.9 was run with the parameters listed in Table 4.8. The results show that the addition of Cl^- has two effects: 1) the resting membrane potential becomes the Nernst equilibrium potential for Cl^- and 2) the intracellular concentrations deviate slightly from what one might consider ideal for the kind of neurons that we are studying. Therefore, we adjusted the permeabilities to find a more depolarized resting membrane potential and to balance the concentration of ions towards the levels that we defined before. The adjusted permeabilities are shown in the last column of Table 4.9 and the results of numerically integrating the model with these parameters are shown in the second column of Table 4.9 (Simulation 2). Note that the permeabilities are given in units of $(C \cdot cm \cdot sec^{-1} \cdot mol^{-1})$, which is the result

of multiplying the permeability times Faraday's constant; we adopt this notation in the rest of this document for simplicity.

The changes listed in Table 4.9 included an increase in $P_{Na,l}$ and P_{Na}, that combined brought the resting membrane potential to a more depolarized level. To compensate for the increase in P_{Na} (fast Na^+ current) and consequent imbalance during depolarized states (i.e., spiking), we increased the permeability of the delayed rectifier (P_K) to keep the same ratio, and therefore, the same AP dynamics. Cl^- permeability was left the same and, as before, X^- is considered to be impermeable.

The model can become exited via two main mechanisms: 1) a change in ionic composition (Nernst equilibrium potential) and 2) via an applied current (I_{app}). All of the simulations in this document use an applied current. In this respect, we decided to simulate our applied current via an increase in Na^+ current in a manner similar to that seen in a nonspecific cation channel activated by a neurotransmitter (i.e., serotonin). The rationale for this is that this models keeps track of ionic composition and an unidentified current (not being carried by a particular ion) generates violation of electroneutrality. As consequence steady-states are not possible under spiking conditions; different scenarios (i.e., a current carried by K^+) gave similar results (not shown).

The model was tested for excitability using an applied current carried by Na^+, see Figure 4.9. We found that stable spiking conditions are not possible in this model formulation. The reason for this is simple: Cl^- has only one way to diffuse across the cell membrane and that is through passive Cl^- channels, and Cl^- fluxes can only be zero when the resting potential equals the equilibrium potential for Cl^-. Under spiking conditions every spike generates a gradient for Cl^- that diffuses inside the cell (down its electrochemical gradient) this leads to accumulation of Cl^- (Cl^- extrusion is not possible because the membrane potential doesn't get more negative than the Cl^- equilibrium potential), and after a series of spikes the accumulation of Cl^- reduces excitability due to hyperpolarization, and spiking stops. Higher amounts of external current lead to more and more depolarized states and higher intracellular concentrations of Cl^- and Na^+ and low intracellular concentrations for K^+, but spiking is not maintained by higher input drive.

In Figure 4.9 (left) we show the results of a simulation with an applied external current of 2.45 $\mu A \cdot cm^2$ that causes spiking for around 8 seconds and then the cell reaches a quiescent steady state at $V = E_{Cl}$. If on the other hand, Cl^- permeability is set to zero, the same applied current generates spiking behavior that is stable, Figure 4.9 (right). Long integration of the model however shows steady changes in the concentrations of Na^+ and K^+ that eventually equilibrate as well as volume and a steady state firing rate is attained after a few minutes (this changes are not shown in Figure 4.9). Note in Figure 4.9 that Cl^- accumulation leads to rapid changes in cell volume, which, in the current version of the model, can not be compensated by any means, but this is the topic of the next section.

4.3.2 Step 2: Cl^- and volume regulation mechanisms

Accumulation of Cl^- causes cell swelling, if unregulated, the increases in cell volume not only affect cell excitability, by changing the ionic gradients, but also has consequences on pH regulation. In our consideration of Cl^- pathways and cell volume regulation we chose to include two known mechanisms that were introduced in chapter 2 and we reintroduce them here and study their effect in cell excitability.

First, we consider the Potassium-Chloride (KCC) cotransporter a transmembrane protein that mediates electroneutral, Cl^- dependent, Na^+ independent, secondary active coupled transport that removes K^+ and Cl^- across the plasma membrane (under most physiological conditions), the driving force for this process derives mainly from the action of the Na^+/K^+ ATPase (82). The kinetic model was developed inspired in the published model for NKCC by (90) (see below) but the parameters were fitted with experimental data measuring Rb^+ uptake in KCC1 transfected *Xenopus* oocytes (91). A more complete mathematical description and the value for rate constants used in this model can be found in the appendix.

Second, we added the kinetics of the Sodium-Potassium-Chloride cotransporter (NKCC) a membrane transport protein that moves Na^+, K^+ and Cl^- across the cell membrane(an influx under most physiological conditions). NKCC maintains electroneutrality by moving Na^+ and K^+ alongside with $2Cl^-$. The kinetics of the NKCC2 cotransporter are described by the early model of (88) and more recently by (90). The rate constants and binding constants were taken form published data collected from experiments measuring Rb^+ uptake in transfected *Xenopus* oocytes (108), and the values are thermodynamically consistent. A mathematical description of the model and the rate constants can be found in the appendix.

Model description

The elements of model are shown in Figure 4.10. The model includes in addition to the already defined variables (membrane potential, cell volume, intracellular concentration of Na^+, K^+, Cl^- and X^- and the activation gate for the K^+ delay rectifier) mechanisms to move Cl^- across the cell membrane that use energy produced by the already present Na^+/K^+ ATPase and help maintain cell volume.

The NKCC and KCC cotransporters do not change the expression that defines the time course of the membrane potential since they are electroneutral. However, the individual ionic fluxes for Na^+, K^+ and Cl^- have to be affected by the new fluxes through the NKCC and KCC, and this expressions were incorporated in the differential equations that represent changes in ionic composition for each one of these ions. The Model is still a 7-D system that couples mechanisms for action potential generation with passive ionic movement, but this revision provides also Cl^- transport processes.

Model parameters

Addition of the NKCC and KCC cotransporters involves 26 new parameters, 24 of of them define the binding rates and the translocation coefficients that defined the kinetics of the cotransporters, and they are described in the appendix. Therefore, in addition to the parameters listed on Table 4.5 (initial permeability-based model), Table 4.7 (after geometrical analysis) and Table 4.8 (with passive diffusion), in this version of the model we needed only to fine tune the amount of expression for the NKCC (E_{NKCC})and KCC (E_{KCC}).

To estimate E for NKCC and KCC we assumed no volume regulation ($E^{MIN}_{NKCC} = E^{MAX}_{NKCC}$ & $E^{MIN}_{KCC} = E^{MAX}_{KCC}$), see appendix for details on how this can be done, and carefully adjusted the level of the enzyme for both cotransporters to achieve a Cl^- level around 6 mM and a volume of 9.2 x 10^{-8} mm^3, consistent with our cell geometry. The values listed on Table 4.10 give the values that we consider to be reasonable after simulations that quantify cell volume compensation and changes in Cl^- concentration.

Numerical integration of model and fine tuning of model parameters

Table 4.11 shows the state variables at steady-state (under no applied current) after numerical integration, and also shows the ones obtained before addition of the NKCC and KCC for comparison. Addition of NKCC and KCC effectively reduced Cl^- concentration with out altering the other variables (due to a relative stronger activity of the KCC). Notice that the resting membrane potential is less negative compared to the equilibrium potential for Cl^-(E_{Cl} = -86 mV), meaning that under resting conditions (no applied current) Cl^- leaks inside the cell through the passive channels and also via the NKCC. The KCC activity becomes the only means for Cl^- to be moved outside allowing for Cl^- equilibrium at membrane potentials different from E_{Cl}.

The model, not surprisingly, is still an excitable cell model and an external current can switch the state of the model. However, the two coupled subsystems: a fast spiking component and a slow transport component interact and shape the response of the model in new ways. The transition from one state to the other, for example from resting to spiking, involves the evolution of the fast system (V and n) and the slow component (cell volume and ionic concentrations) simultaneously with their own intrinsic time constants, so equilibrium can only be achieved after considerably long integration times, after ions have reached equilibrium, which can takes thousand of spikes. As soon as the model is subject to an applied current, spiking begins and gradually the changes in the slow variables accumulate until the slow system feedbacks on the fast component. Under certain circumstances, for example the changes in the slow variables can bring the model back to resting state, or a quiescent model could be turned on by changes on the variables in the slow subsystem. Therefore to find tonic spiking conditions one has to allow the whole system to reach steady states that are compatible with continuous changes in the membrane potential. The model with

out Cl^- pathways was not able to produce this kind of behavior due to chronic Cl^- accumulation. This instance of the model, on the other hand, exhibits stable spiking behavior for some combination of the parameters.

Figure 4.11 shows the evolution of the states variables as the model is switch from resting to spiking and the eventual achievement of steady state spiking conditions. For example, Na^+ concentrations increase from 8 mM to 18 mM due to the continuous influx of Na^+ during the the activation of the voltage gated Na^+ channels and the inability of the Na^+/K^+ ATPase to pump out the Na^+ at the current Na^+ levels, but eventually increased Na^+ levels are just adequate to match the influx via voltage gated channels, passive diffusion and Na^+/K^+ ATPase activity. Similarly, K^+ concentrations decrease due to the continuous efflux of K^+ during the the activation of the voltage gated K^+ channels and through passive diffusion. K^+ levels finally achieve equilibrium when the efflux via voltage gated channels and passive diffusion and KCC activity matches the Na^+/K^+ ATPase and the NKCC. Chloride levels are maintain by the influx caused by the NKCC and passive diffusion that equilibrates with the KCC activity.

From a dynamical point of view the model still retains all of the desirable features that we identified previously, namely class 1 excitability, monostable and non-monotonic I-V relation. For example, we wanted to test the response of the model in terms of its FR to an increase in the applied current. An increase in external current from 3.1 (shown in Figure 4.11) to 3.11 (not shown) cause and increase in FR of 1Hz to 2 Hz and a small increase in Na^+ (from 18.87 to 19.58) and Cl^- (from 6.18 to 6.22) accompanied by a small decrease in K^+ (from 132.18 to 131.47). This demonstrates that model has class 1 excitability.

In this instance of the model, as opposed to the model with no Cl^-pathways and volume regulation capabilities, no significant changes in cell volume are observed. After the long simulation shown on Figure 4.11, for example, a change in cell volume of less that 0.01% was observed after 510 seconds, and once steady state was achieved the volume remained constant (trace not shown in Figure 4.11). Compare this result with the 0.03% change after only 12 seconds shown on Figure 4.9 for the previous version of the model.

4.3.3 Step 3: pH regulation (transport-excitable model)

One of the primary features of CO_2/H^+ chemoreceptors is their ability to change their intrinsic membrane oscillations as a consequence of increased levels of CO_2, which are often accompanied by changes in intracellular pH. Any attempt to model cellular mechanisms involved in CO_2/H^+ chemoreception have to include acid-base regulation elements. Our approach to acid base regulation discussed in chapter two included three buffers in equilibrium, a Na^+-H^+ exchanger (NHE) and Cl^--HCO_3^- exchanger (AE). For the transport-excitable cell model we follow the same approach but choose to include only bicarbonate as the main buffer given that is the most active one at physiological pH, but retained the AE and the NHE as the acid loader and extruder respectively. The purpose of

this section then is to integrate the acid-base regulation component and asses its effects in excitability and model dynamics. This model is used later to compare chemosensitive vs. no chemosensitive neurons exposed to HA.

Model description

So far we have combined an excitable cell model and a transport cell model that incorporates passive diffusion of ions, kinetic descriptions of a Na^+/K^+ ATPase, $Na^+/K^+/Cl^-$ exchanger (NKCC) and K^+/Cl^- exchanger (KCC), and Na^+ and K^+ voltage gated membrane currents. The acid-base regulation component, the last addition, is divided in two parts: a buffer system and the exchangers.

Here we consider only the bicarbonate buffer system knowing that this buffer is the most relevant for respiratory perturbations (i.e., HA). Equations describing the fluxes for each one of the species and changes in pH are described in the appendix (B.2). To complete the pH regulation component we consider here two major acid/base regulation pathways that were already introduced in chapter 2 and are described in the appendix:

1. The Na^+/H^+ exchanger (NHE) which is a transmembrane protein that has one binding site that competes for Na^+, NH_4^+ and H^+ and can move hydrogen or ammonium out of the cell in exchange for sodium under most physiological conditions. The NHE model is based on the kinetics published by (144) and (5) and small variations of this model, as described in chapter 3 and the appendix, produce kinetics for three different isoforms: NHE1, NHE3 and NHE5 (only NHE1 present in this model). We refer the reader to chapter 3 for a more complete description of the different isoforms and their location within the brainstem.

2. A kinetic model of the Cl^-/HCO^-_3 exchanger (AE) which was developed by Chang and Fujita in 2001 and experimental data for the parameters came from human red blood cells experiments by (50). The transporter has a binding site for Cl^- and HCO_3^-, typically removes HCO^-_3 form the intracellular compartment in exchange of Cl^-.

At this point our pH regulation component is complete and can be added to model. Before doing that we note that the only pathway for H^+ is the NHE (passive diffusion of H^+ is not considered) and that the flux of bicarbonate is the balance of passive diffusion and the activity of AE.

The equation that describes the time course of the membrane potential is modified to account for the recently added bicarbonate flux, (carbonic acid has no charge and the permeability for H^+ was set to zero and both the NHE and the AE are non-electrogenic so they do not contribute to changes in membrane potential). Therefore, the currents considered are fast Na^+ and K^+, passive movement of Na^+, K^+, Cl^-, $HCO3^+$ and the Na^+-K^+ ATPase.

The change ion concentration now includes the expression for H^+ and AT (total amount of buffer) and the fluxes through the NHE and AE. These expressions can be found in appendix B.2

The transport-excitable cell model is a 9-D system of non-linear differential equations that describes a single compartment model with two components: 1) a fast excitable subsystem that includes membrane potential and the activation variable for I_K, and 2) a slow subsystem that includes changes in cell volume and changes in intracellular ionic composition (Na^+, K^+, Cl^-, X^-, H_T and A_T). Both systems drive each other in nontrivial ways and give birth to a family of interesting behaviors, some of which are the topic for the rest of this chapter.

Model parameters

In addition to the parameters listed on Table 4.5 (initial permeability-based model), Table 4.7 (after geometrical analysis) and Table 4.8 (with passive diffusion) and Table 4.10 (addition of Cl^- pathways); the transport-excitable model includes the parameters listed on Table 4.12. The new parameters on Table 4.12 were defined so a reasonable quiescent steady state was achieved with the model. Note that the transition from quiescent to dynamic spiking involves the change in almost all state variables, so a set of parameters that allow for this transition and produce reasonable values after steady state most be achieved.

For this purpose we started by studying the levels of Na^+ and K^+ during spiking and resting conditions and concluded that for a reasonable membrane potential the maximum pump current for the Na^+/K^+ ATPase was to be increased from 5 to 15 μA/μF to compensate for the new influx of Na^+ via the NHE. The Na^+ leak permeability ($P_{Na,l}$) was increased slightly from 0.009 to 0.01 ($C \cdot cm \cdot sec^{-1} \cdot mol^{-1}$) to get a baseline resting membrane potential around -65 mV.

Changes in the concentrations of the extracellular compartment were necessary to accommodate the newly defined elements. The model no longer needs an unidentified negatively charged particle outside (X^-) given that bicarbonate plays that role, note that the model still has the same osmolarity (300 mOsm) and it is electroneutral. The equilibrium constant for the bicarbonate buffer (0.34 mM) has been used in respiration models (41) and the hydration dehydration rates from CO_2 were assumed to be the un-catalyzed values. We generated an extracellular pH of 7.4 (typical extracellular pH) and assume that bicarbonate and carbonic acid concentrations are given by the Henderson-Hasselback equation. H^+ was assumed to be impermeable and bicarbonate permeability (P_{HCO3}) initially was chosen to be equal to P_{Cl}. Normal levels of CO_2 are 40 mmHg (1.2 mM) and hypercapnia, in this chapter, is assumed to be 80 mmHg (2.4 mM). HA, as before, is simulated by increasing the amount of CO_2 which causes a decrease in extracellular and intracellular pH.

Numerical Integration of the transport-excitable model

The steady state achieved with this set of permeabilities and the pH component, when there is no applied current, produces an interesting pattern of fluxes: bicarbonate leaks out of the cell via passive diffusion (E_{HCO3} = -13 mV) and through the AE, it is replaced by the formation of carbonic acid as a result of the hydration of CO_2 and subsequent dissociation in bicarbonate and protons (Carbonic acids forms inside the cell as a consequence of the difference between

pH_i and pH_o, in other words H_2CO_3 is more “abundant” outside). Intracellular H^+ equilibrium is govern by the generation of H^+ via the same mechanism (dissociation of carbonic acid in bicarbonate and protons) and proton extrusion via NHE. At resting membrane potentials Cl^- diffuses out of the cell (against its concentration gradient) but is replaced by a Cl^- influx through the AE (in exchange for HCO_3^-), and via NKCC (using the concentration gradient for Na^+). The other extrusion pathways for Cl^- is the KCC, that as before, helps maintain Cl^- levels during spiking conditions when Cl^- leaks into the cell. (E_{Cl} in this model is -57 mV).

4.4 Cellular mechanisms involved in CO_2/H^+ chemoreception

4.4.1 Response to HA of the transport-excitable model on resting mode

The non-chemosensitive neuron

HA was introduced back in chapter 2 when we were testing the responses of the transport model. HA has a very characteristic response in most neurons with the notable exception of some central CO_2/H^+ chemosensitive neurons. Simulation of HA produces the same overall behavior observed before with the transport model (chapter 2) when there is no external applied current. Note that different states of the model can result in radically different patterns and we will study some of them later in this chapter (i.e., HA could induce transition from resting to spiking), here we explore the response when the model is at a resting state and HA does not change the dynamical state of the model (simulation not shown).

With transport-excitable model we observed how elevated levels of CO_2 produce a rapid acidification (a drop around 0.3 pH units for and increase in 20 mmHg in CO_2) followed by a partial recovery to an acidified pH level. Upon removal of elevated levels of CO_2 a short alkalinization is observed , followed by baseline pH levels. The change in pH is mediated by the balance between the rapid hydration of CO_2 followed by the dissociation of H_2CO_3 into H^+ and HCO_3^-, that is offset very quickly by the activity of the NHE. We corroborated this by noticing that for the entire duration of the challenge the net H^+ flux is an efflux that continuously increases the low pH_i achieved at the very early stage of the challenge.

During HA the membrane potential shows an initial hyperpolarization followed by slow recovery towards more depolarized levels (close to baseline). This response can be explained in terms of currents: the rapid increase in positive current (hyperpolarization) is fundamentally mediated by the Na^+/K^+ ATPase, all other currents exert a depolarizing effect. As the challenge progresses the current decrease as the Na^+ accumulates inside the cell driving the membrane potential towards less negative conditions.

Na^+ dynamics during HA, are characterized by an rapid increase followed by a slow removal. The rapid increase is the result of the NHE activity and a very

minor role of passive diffusion (due to hyperpolarization that causes an increase in the driving force); the Na^+ accumulation is rapidly compensated by the Na^+/K^+ ATPase. By the end of the challenge very small outward flow is still present as the cell progress towards new equilibrium.

The changes in K^+ are quite surprising, contrary to other ions in the model, K^+ concentrations are subject to changes in cell volume. If one does not consider the apparent flux due to water movement (i.e., $K_i \times J_w$ in eq. A.3) the other fluxes together (leak, gated, NKCC and KCC) would predict K^+ accumulation during HA. The recovery from low levels of K^+ is mainly the work of Na^+/K^+ ATPase.

As for Cl^-, its dynamics are predominantly the consequence of the AE that brings Cl^- in as bicarbonate becomes readily available during HA. Cl^- leaks out of the cell through passive channels and comes in via NKCC (which doesn't play a big role with the amount of expression put in the model). KCC helps restore Cl^- levels leveling off the initial rate of accumulation after CO_2 was elevated. Finally, HCO_3^- accumulation is, analogous to what described for pH, the result of the dissociation of H_2CO_3 into H^+ and HCO_3^-. In the case of bicarbonate this accumulation is partially offset by the activity of AE and in a lesser proportion by the passive diffusion of HCO_3^- outside the cell.

The chemosensitive neuron

We characterized a chemosensitive neuron based in our studies on pH regulation (chapter 3), as a neuron with an NHE that is less sensitive to pH_i. This configuration allow us to generate a blunted pH_i recovery seen during HA for neurons that exhibit this phenotype. In terms of parameters, the chemosensitive neuron is represented by setting the internal modifier off for the NHE (mathematically this means $f_M = 1$ and $k = 0$, see appendix for details about those parameters) and adjusting the level of the expression of the enzyme to achieve a reasonable baseline pH (E_{NHE} was set to 0.29). When we tested this configuration and compare it to the response of non-chemosensitive neurons we observed the same blunted response produced by the transport model. Figure 4.13 compares the response of the non-chemosensitive neuron to that of the chemosensitive. The steady-state values for the variables of the chemosensitive configuration under no applied current are almost identical to those of the non-chemosensitive version and we omit to show them for brevity.

On the other hand, the membrane potential response of the chemosensitive neuron is somehow different, they both share the hyperpolarization and slow recovery back to baseline, but the extent of the depolarization on the chemosensitive neuron is reduced, which has profound impacts on model behavior under spiking conditions (see below). This response is just the result of a less active NHE that moves less Na^+ in exchange for H^+ and therefore the positive current generated by Na^+-K^+ ATPase responsible for the hyperpolarization is less pronounced (right panel in Figure 4.13).

4.4.2 Response to HA of the transport-excitable model on excited mode

The transport-excitable model is an excitable model

One might ask if the model after all the transformations performed in the previous sections is still an excitable cell model and how its response compares to the ones we observed earlier. As soon as the model is subject to an external applied current spiking begins and slowly the changes in the slow variables develop until the slow system feedbacks on the fast component. Therefore to find tonic spiking conditions one has to allow the whole system to reach steady states that are compatible with continuous changes in the membrane potential. the final values of such a simulation are shown in Table 4.14 where an applied current of 4.5 $\mu A \cdot cm^2$ results in FR of around 2.5 Hz. We compared the values of the state variables after reaching steady-state and compare them with the model under no applied current. We corroborated that the changes are small and are within physiologically meaningful range.

In Figure 4.14 we show the results of a numerical integration when a current of 4.5 $\mu A \cdot cm^{-2}$ is applied to the model using the parameters defined in Table 4.12. A magnification of one the multiple action potentials (right panel in Figure 4.14) shows the interaction between the currents that shape the AP. As expected voltage activated Na^+ and K^+ currents play the bigger role, due to their magnitude, in the final form of the AP, but in contrast to the resting state, when activated, the model exhibits a reversed pattern for Cl^- and HCO_3^-, both ions passively moved to the intracellular compartment, therefore increased activities of AE and KCC compensate to maintain normal level of the ions.

The non-chemosensitive neuron

We wanted to explore the response of the model to HA under tonic spiking, analogous to a neuron driven by synaptic input. Thus we used the model at the state shown in Figure 4.14 as the stable spiking state and increased CO_2 for 800 s. The result of this simulation (not shown) demonstrated that the baseline firing rate of around 2.5 Hz is maintained during baseline before the increase in CO_2, but once hypercapnic conditions appear, the model switch to quiescent mode for the entire duration of the acidic challenge, this transition can be explained in terms of the initial hyperpolarization observed during HA due to the Na^+-K^+ ATPase. After approximately thirteen minutes, when CO_2 is returned back to a normal level, the sudden depolarization caused by the Na^+-K^+ ATPase that decreases the amount of current because of a fall in Na^+, switches the model back to spiking at a faster rate (25 Hz) for a relative small depolarization (around 4mV). This demonstrates that the model still possesses class 1 neuronal dynamics, compatible with saddle node on invariant circle bifurcation and that small changes in membrane potential can elicit strong responses in a dynamical system that is close to the bifurcation point.

The changes in ionic species occur by the same reasons exposed before when the model is resting, with a few exceptions: 1) Na^+ and K^+ concentrations don't go back to resting levels, as rapidly as before (when the model was

quiescent) after CO_2 is removed due to a sudden re-initiation of a spiking regimen. 2) Cl^- moves into the cell during most of the time (although this pattern reverses for some time during HA, due to hyperpolarization and that E_{Cl} is -57 mV), 3) bicarbonates switches form inward flux to outward flux; HCO_3^- moves in passively for a brief period of time during spiking due to depolarized membrane potential and that E_{HCO3-} = -13.30 mV; and switches back to outward flux during hyperpolarized levels.

The chemosensitive neuron

The chemosensitive neuron has the same properties introduced before (no additional change in parameters are necessary to accommodate for excitation) and exhibits spiking behavior at a remarkable similar FR as the non-chemosensitive for the same depolarizing current of 4.5 $\mu A \cdot cm^{-2}$. Figure 4.15 compares the response of the non-chemosensitive neuron to the chemosensitive. The steady-state values for the variables of the chemosensitive configuration under applied current are almost identical to those of the non-chemosensitive version and we omit to show them here for simplicity.

In addition the membrane potential response of the chemosensitive neuron shows a lesser degree of hyperpolarization during HA, but it also switches from spiking to quiescent, the firing rates are comparable for the resting state but the chemosensitive neuron fires at low frequency compared to the non-chemosensitive after the HA challenge (Figure 4.15 right panel).

4.4.3 Effect of HCO_3^- permeability on the response to HA

Up to this point we found that small changes in ionic composition can switch the model from spiking to quiescent and vice-versa, this observation imposes a question on whether slight changes in ionic permeability could explain the differences in chemosensitive vs. non chemosensitive neurons. So far the difference in NHE affinity for intracellular H^+ used to differentiate between them, shows a promising trend in the sense that not only blunts the pH response but also produces a concurrent effect: a hyperpolarization followed by depolarization that is less severe that the one seen for the non-chemosensitive configuration on membrane potential during HA. This means that the enzyme affects both traits simultaneously. The down side, is that with this configuration our results deviate from those seen experimentally, where a non-chemosensitive neuron maintains an unaltered FR during HA (no change in membrane potential) and the chemosensitive neuron shows an increase in FR (depolarization). For a typical response of putative chemosensitive neurons from the raphé to HA see Figure 1 in (33).

From a strictly theoretical point of view, we approached the possibility of a parameter selection that could change the effect of HA, so an increase in FR is observed as opposed to inhibition and subsequent decrease in FR. The transport-excitable model has only two parameters that can change the voltage

response to HA with out significantly altering the resting state or AP dynamics, and they are P_{Cl} and P_{HCO3}. Because they both move out under resting conditions, increasing their permeability effectively increase the amount of negative current moving into the cell (depolarization). Under spiking conditions however, only HCO_3^- moves to the extracellular compartment (but not for the entire duration of the spike, but for most), because Cl^- with a reversal potential around -57 mV switches from efflux to an influx and becomes a hyperpolarizing current during tonic spiking. This makes bicarbonate an attractive possibility. The other currents involved that can alter the response to HA in terms of membrane potential have profound effects on ionic composition under resting conditions and to the pH response, thus being less attractive as potential candidates to be present in real cells.

Therefore, we decided to study the effects of bicarbonate permeability (P_{HCO3}) to the response during HA. To this, we increased P_{HCO3} to the level of P_K and adjust P_{Na} for a less depolarized baseline membrane potential and increased the amount of expression of the NHE (from 2 to 3 in non-chemosensitive neurons and from 0.29 to 0.39 in chemosensitive neurons) to obtain the same baseline pH used for previous simulations. Higher P_{HCO3} produces enough current during HA to depolarize the cell instead of the previous observed hyperpolarization. Therefore under HA the neuron doesn't transition from spiking to resting, but instead shows and increase in its firing rate during the perturbation that is reversible (see Figure 4.16) after CO_2 is returned to normal levels.

These results show that bicarbonate permeability changes the response of the model to HA but this change produces the same trend for chemosensitive and non-chemosensitive neurons. In fact they both increase FR and the change is actually bigger in non-chemosensitive neurons. Thus, increased bicarbonate permeability has to be an independent feature of chemosensitive neurons to be accounted as a mechanism in CO_2 chemoreception, suggesting that one single mechanism (i.e., NHE) is not enough to have a differential pH and excitable response to HA, at least as suggested by our mathematical model.

4.5 Discussion

A previous study using a mathematical model that used outward K^+ currents as the signal sensor suggested that "the poor pH regulation exhibited by CO_2 chemosensory neurons requires active regulation of intracellular and extracellular pH and active regulation of transporter [acid-base balance mechanisms] expression" (25). In this study the authors did not incorporate kinetic description of the acid-base balance and other transporters involved in neuronal homeostasis, but were able to conclude that the inclusion of these mechanisms was required for a better understanding of chemoreception function at the cellular level. The model that we developed intended to fill this gap and contribute to the understanding of the cellular components involved in chemoreception. We think

that the increased complexity of this model is wile-worth if a unified understanding of the process is to be achieved.

Before listing the virtues of the model we think is important to list some of its limitations: the model is less than a minimal model for central CO_2 chemoreception, there are plenty of currents described in the literature, that even if their participation hasn't been demonstrated yet in chemosensitivity, they should be included in a model that pretends to address questions of CO_2 sensitivity. Some of the channels that have been identified in chemosensitive areas and have been postulated to play a role in chemosensitivity are: the TEA sensitive K^+ channel (46), the TASK channel (46), the A type potassium current (I_{KA}) (25), a pH sensitive inward rectifier (I_{Kdir}) channel (25) and Ca^{++} sensitive K^+ current (I_{KCa}) (25), all inhibited by hypercapnia and more recently a cation channel (I_{CAN}) that is suggested to be present in raphé neurons (33).

Furthermore, we used a variety of sources for our parameters of the transporters and in some cases permeabilities were adjusted to qualitatively reflect known experimental behavior, ideally this parameters should come from neurons from chemosensitive and non-chemosensitive regions. In addition, we did not include in the model synaptic events or gap junctions that might alter the response to HA (128) and we did not attempted to model neuronal geometry, spatial distribution of ionic channels or the effect of the dendrites, which all might be important in the response to hypercapnia (123). We did not include Ca^{++} as an active ion in the model, knowing that future studies will require the presence of this ion and possibly Ca^{++} dependent exchangers for completeness and relevance in CO_2/H^+ chemosensitivity. We are currently revising the model to adjust for this features and integrate these factors into our analysis.

The GHK normalization of I_K and I_{Na} was carried before by several authors (28, 94) under the notion that the expression $I = g(V-E)$ can not be correct when the ionic difference across the cell membrane is too big (30). This is the case for Na^+, K^+ and Cl^- in mammalian neurons: $C^i_K >> C^o_K$, $C^o_{Na} >> C^i_{Na}$, $C^o_{Cl} >> C^i_{Cl}$. When the membrane potential (V) is greater than the equilibrium potential for the ion (E_i) ($V >> E_i$) or vice versa ($V << E_i$) the currents are mainly carried by the intracellular or the extracellular ions respectively. Therefore the slope conductance on both extremes can not be the same (64). This non-linearity is well captured by the GHK equation and in general is considered to be a good approximation for fully activated voltage gated currents (28). The applicability of this normalization is an active topic of research and remains to be fully understood, but based on preliminary data we consider a permeability based model that uses the GHK description of ionic movement to be a better approximation to study cell excitability in neurons and in particular when passive currents are being calculated that way. Other approaches like the multi step Markov chain model for the sodium channel (138) have been proposed for mammalian neurons, but we did not attempted to include or compare the effects

of using that kind of model, but we consider revising these possibilities in the future.

At least two different mechanisms that include Cl^- could be involved in pH sensitivity in vivo. First, Cl^- is being exchanged by the Cl^--HCO_3^- exchanger and second, by the Na^+ driven Cl^--HCO_3^- exchanger. Both of them are known to be present in neurons(73). Thus Cl^- not only plays a role in pH regulation but also is important for cell volume regulation, and these two variables, as we demonstrated here, could be potentially involved in CO_2 sensitivity. On the other hand, Cl^- mediated synaptic conductances have been suggested to play a role in other respiratory related neurons (37). For example the maturation of the Cl^- reversal potential in rat hypoglossal motor neurons has been proposed to shape the inspiratory burst (37), suggesting a possible role of Cl^- in cell excitability.

Another element that we found to be important in shaping the response to HA is the Na^+-K^+ ATPase, which surprisingly has not been proposed to play a role in CO_2 sensitivity. However, based on our simulations and with our current understanding of HA conditions and its consequences in cell excitability, we found that the Na^+-K^+ ATPase is in fact responsible for the hyperpolarization during HA. As the pump increases its tonic outward current, due to the influx of Na^+, the cell rapidly depolarizes. This current is compensated by inward currents that depending on their magnitudes might move the membrane potential below baseline levels. One might imagine an scenario in which a pH sensitive Na^+-K^+ ATPase is inhibited during HA causing a decrease in the amount of hyperpolarization and allowing the chemosensitive neuron to increase its firing rate. This idea, however, has not been suggest as a possible mechanism.

Contrary to popular understanding, the strict need for pH sensitive currents to mediate the response of increased CO_2 seems to be arguable, we found that modulation of membrane potential dynamics during changes in CO_2 is possible via small changes in ionic composition caused by the transport component of the cell and that these changes are linked to mechanisms that regulate pH. This, however, does not rule out the possibility that CO_2 sensitivity is carried out manly or only by pH sensitive currents, but it does suggest that the transporters that modulate the acid-base response of the cell to acid challenges could potentially be part of the set of elements modulating membrane potential response.

Previous studies suggest that for a chemosensitive neuron to achieve that "perfect" non regulatory pH_i response during hypercapnic acidosis is necessary to have an NHE that shows a balance of inhibition by extracellular pH and activation by intracellular pH that cancels out during HA. This hypothesis requires exact intracellular and extracellular pH response profiles but a pK shifted to accommodate for the differences between intracellular and extracellular compartment (110). We suggest that according to our model of the NHE, in which intracellular ion binding is competitive, a simple decrease in affinity for H^+ is enough to blunt the response to HA, but other kinetics models of the NHE have been proposed (111) and it is an open question which one better describes this mechanism in chemosensitive neurons.

On the other hand, based on our results it seems that just the differences in NHE sensitivity wouldn't be sufficient to explain both the pH response and the changes in membrane potential. Even though they are linked (i.e., a change in NHE sensitivity alters both the pH and the membrane potential response to HA) the effect on chemosensitive neurons points in the opposite direction. In other words, the decreased NHE sensitivity cause less pronounced changes in membrane potential. One possibility to reconcile this situation is that chemosensitive neurons exhibit also an increase in bicarbonate permeability that increases even further the lack of pH_i recovery during HA and compensates for the increases in negative current generated during HA that ultimately reflects in an increase in firing rate.

Even though there is no evidence for HCO_3^- mediated currents involved in CO_2 chemoreception, it has been reported that HCO_3^- can increase excitability in hippocampal neurons (20). In addition the $GABA_A$ channel has been shown to be permeable to HCO_3^- (110) with a selectivity of Cl^-:HCO_3^- of 1:5 (72). Activation of the $GABA_A$ channel could lead to an efflux of HCO_3^- with accompanied intracellular acidification. The movement of HCO_3^- will also depolarized the cell, and thus changes in HCO_3^- can potentially affect pH regulation and neuronal excitability via activation of $GABA_A$ channel. Therefore a detailed examination of the role HCO_3^- in central CO_2 sensitivity seems to be important.

There is a final question that remains and surprisingly it has been almost totally ignored, and that is: what elements allow the non-chemosensitive neuron to compensate for the changes induced by HA and actively regulate pH and avoid changes in membrane potential? elements that effectively turn the neuron immune to acid challenges. Based on our model simulation studies we noticed that HA produces small changes in membrane potential, but unless these changes are compensated for, some degree of chemosensitive should be noted in non-chemosensitive neurons and that hasn't been reported in the literature. Clearly, these elements can not be just the absence the ones that allow the chemosensitive to transduce the signal.

In summary, we concluded that ionic changes produced during HA can modulate the response of an excitable cell (via changes in Nernst equilibrium potentials, or via pushing the system beyond the bifurcation point) and therefore they have to be considered in a multiple factor model of CO_2 chemoreception. We also found that a model with I_{Na} and I_K as the only means for excitability doesn't capture the changes in the frequency response, observed experimentally, of the action potential during HA. Finally we found that a Na^+-H^+ exchanger (NHE) that is less sensitive to changes in pH_i than the NHE from non-chemosensitive neurons produces a blunted pH_i response to HA but does not correlate with changes in FR, supporting the idea that CO_2/H^+ chemosensitivity is a multifactor model.

current is given by I = g(V-E) in an HH model

current is given by I = FPφ(Cie^{φ}-Co)/(e^{φ}-1) and φ=zFV/RT in a permeability-based model

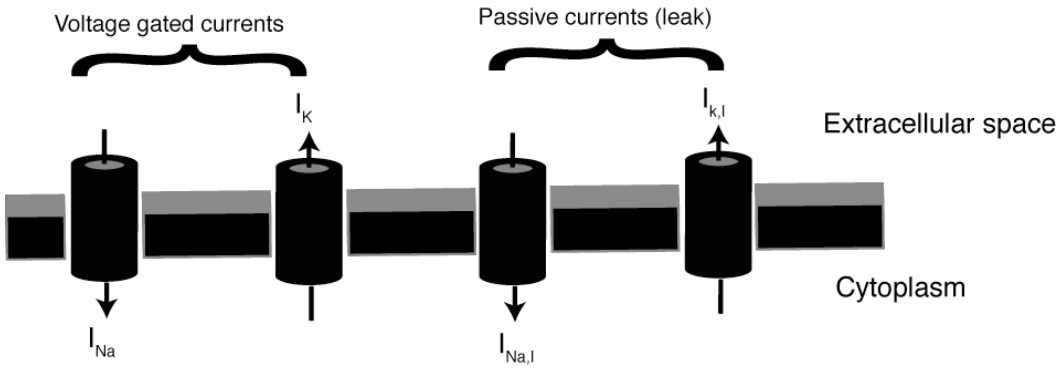

Figure 4.1 Elements and current description for the HH model and the permeability-based model.

The model contains 2 voltage sensitive channels (I_{Na} and I_K) and a leak current divided in Na^+ ($I_{Na,l}$) and K^+ ($I_{K,l}$) components. Current is described by ohm's law in HH model and by the GHK equation in the permeability-based model

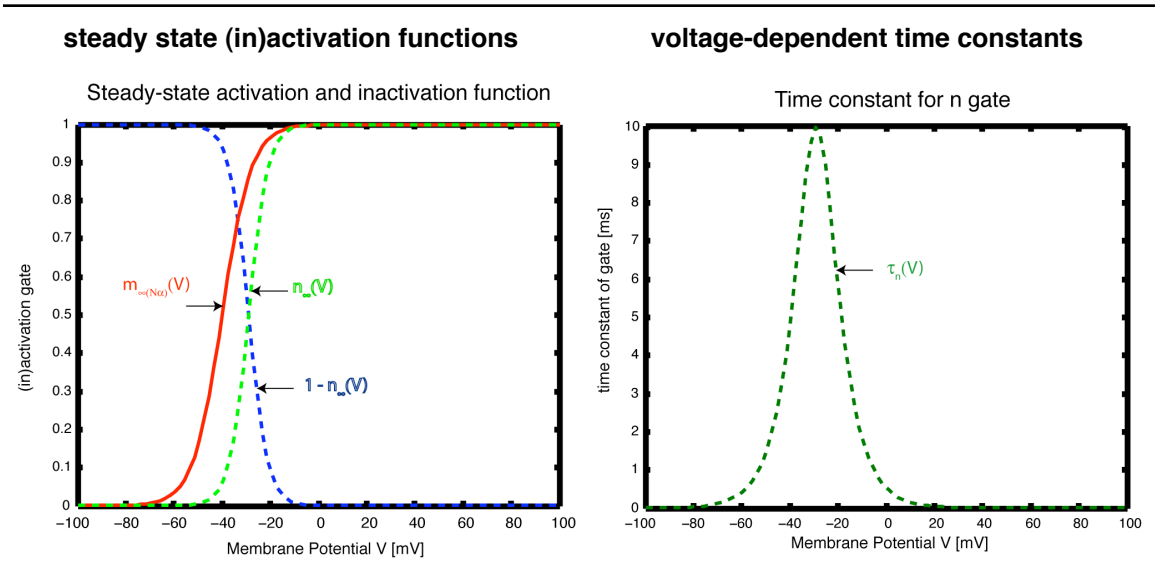

Figure 4.2 Steady-state (in)activation functions and voltage dependent time constant.

A. Activation-Inactivation functions for the voltage gating variables and **B**. time constant for voltage gated K^+ channel. *m* is the activation gate for the Na^+ channel, *1-n* is the inactivation term for the Na^+ channel; and *n* is the activation gate for K^+.

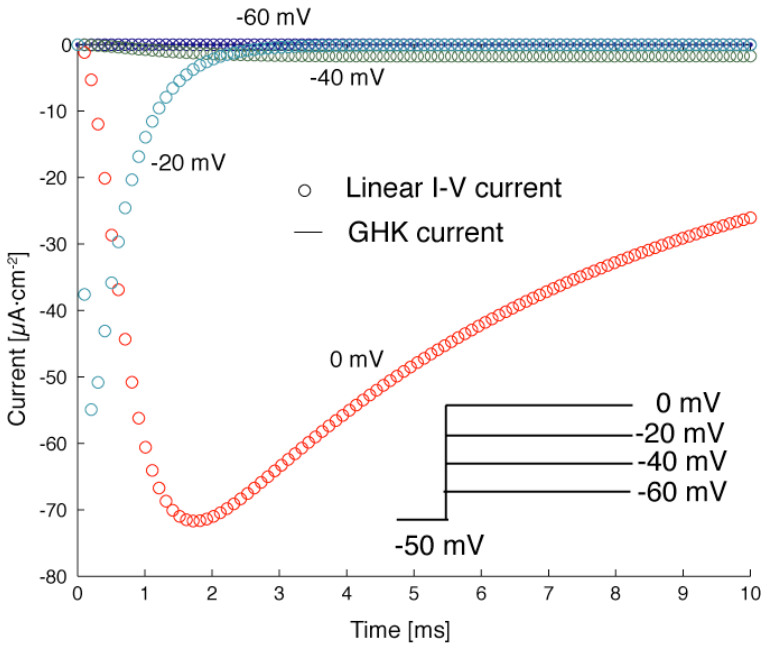

Figure 4.3 Output of optimization routine to find the parameters for I_{Na} in permeability-based model.

Four voltage steps from the baseline voltage (-50 mV) were used to generate the time course of the currents at different holding potentials.

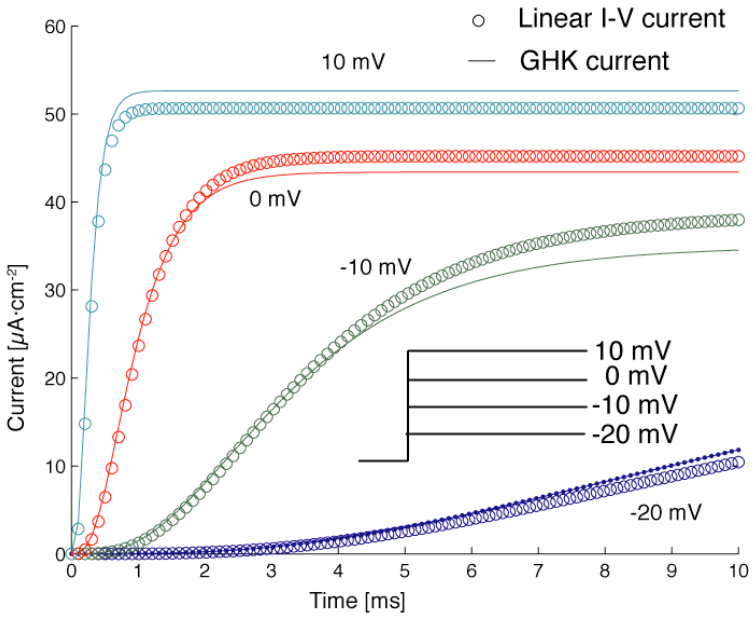

Figure 4.4 Output of optimization routine to find the parameters for I_K in permeability-based model.

Four voltage steps from the baseline voltage (-50 mV) were used to generate the time course of the currents at different holding potentials.

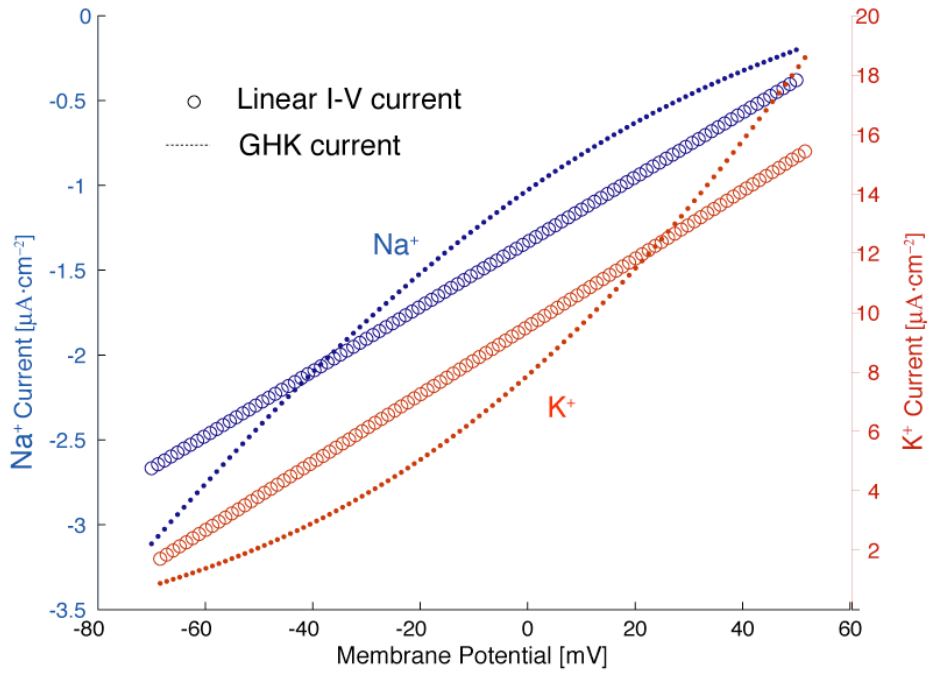

Figure 4.5 Output of optimization routine to find the parameters for $I_{Na,l}$ and $I_{K,l}$ for permeability-based model.

Figure 4.6 Geometrical analysis for HH and GHK models.

Comparison of HH model (left column) an permeability-based model (right column) from a geometrical point of view. The upper two figures show the phase portraits when $I_{app} = 0$. The V nullcline (solid line) meets the n nullcline (dashed line) at the stable Node that corresponds to the steady state of the system(solid red). Two other unstable equilibria are present in the system, a saddle around 40 mV and Focus around -23 mV. An applied current displaces the V nullcline up, and the steady state disappears via saddle node bifurcation on invariant circle as seen on the second two figures from up. The red line represents the trajectory that follows the limit cycle. Numerical solution of the system shows the spiking behavior (third pair of figures from up)which can be modulated by the magnitude of the applied current; consistent with class 1 neuronal excitability, as shown on the bottom. Roughly twice the amount of current can produce 10 time the original FR

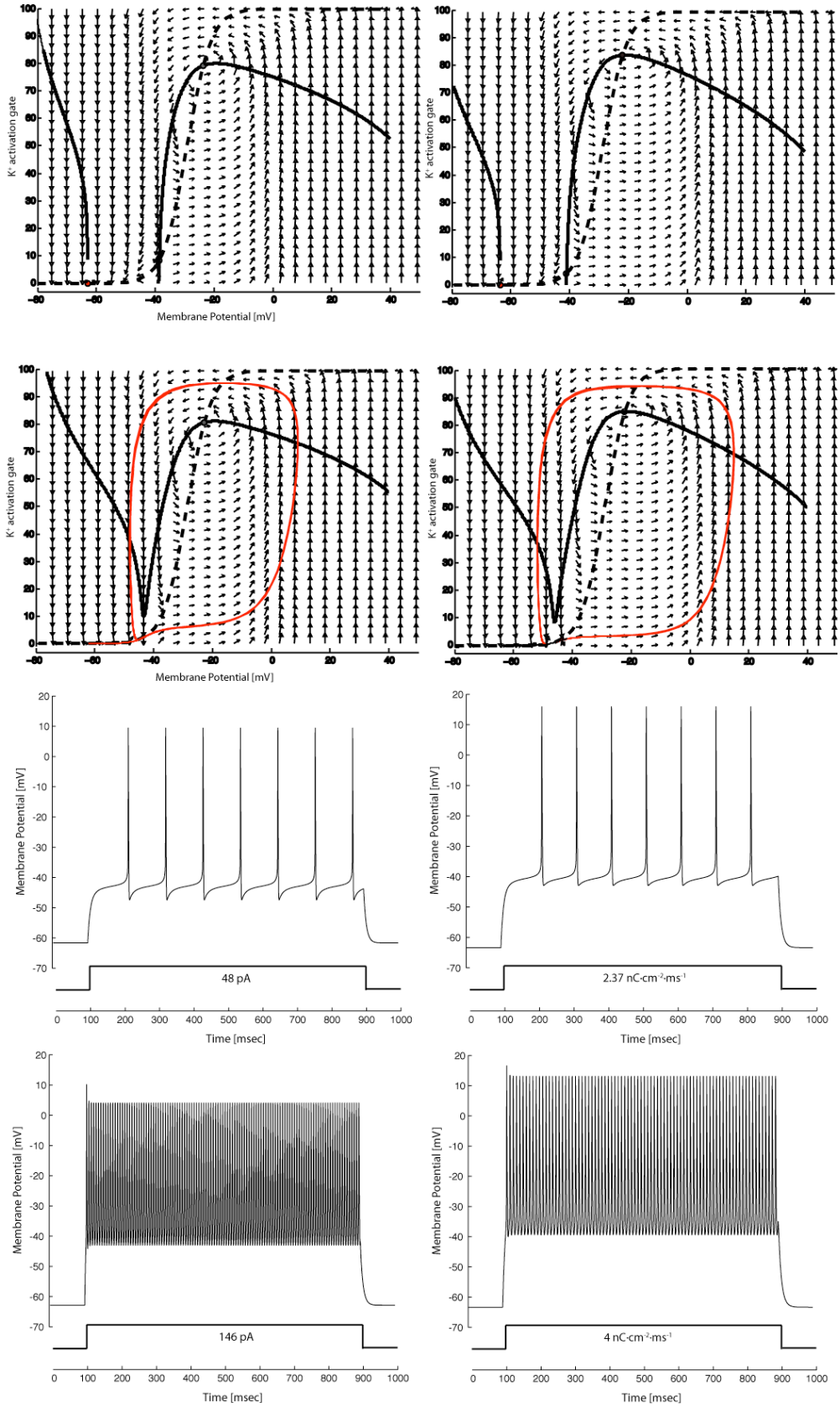
K+ activation gate
Membrane Potential [mV]
Membrane Potential [mV]
48 pA
Time [msec]
2.37 nC·cm-2·ms-1
Time [msec]
146 pA
Time [msec]
4 nC·cm-2·ms-1
Time [msec]

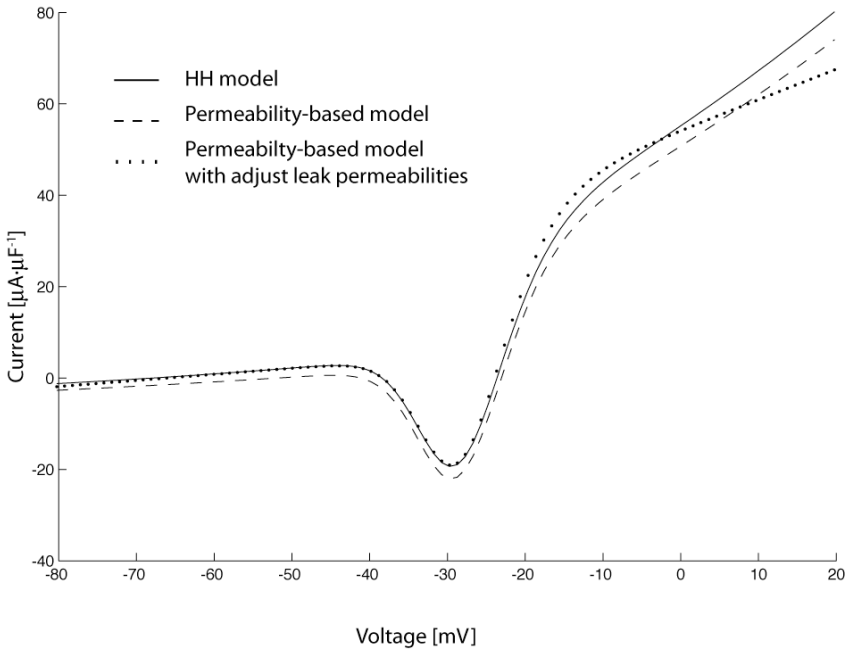

Figure 4.7 Steady-state I-V relation.

The HH model (solid line) has a non-monotonic I-V relation that is resembled by the permeability based model before geometrical analysis (dashed line) and even closer agreement when the permeabilities for the leak currents are adjusted after geometrical analysis (dotted line). The units for currents are given per pF for comparison. (the HH is formulated for total cell capacitance and the permeability-based model has capacitance per unit area)

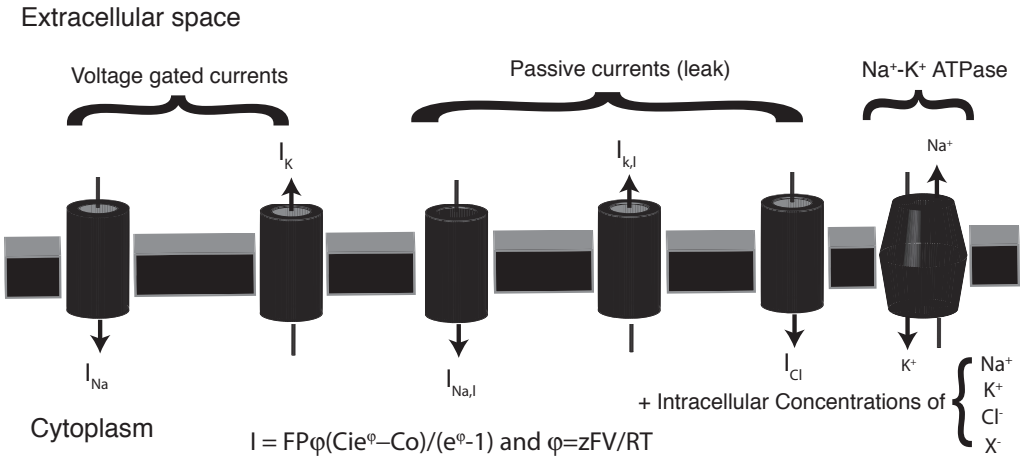

Figure 4.8 Addition of passive diffusion of main ions.

The model contains 2 voltage sensitive channels (I_{Na} and I_K) and a leak current divided in Na^+ ($I_{Na,l}$) , K^+ ($I_{K,l}$) and Cl^- (I_{Cl})components. The model includes the Na^+/K^+ ATPase and follows intracellular concentrations of Na^+, K^+, Cl^- and X^-.

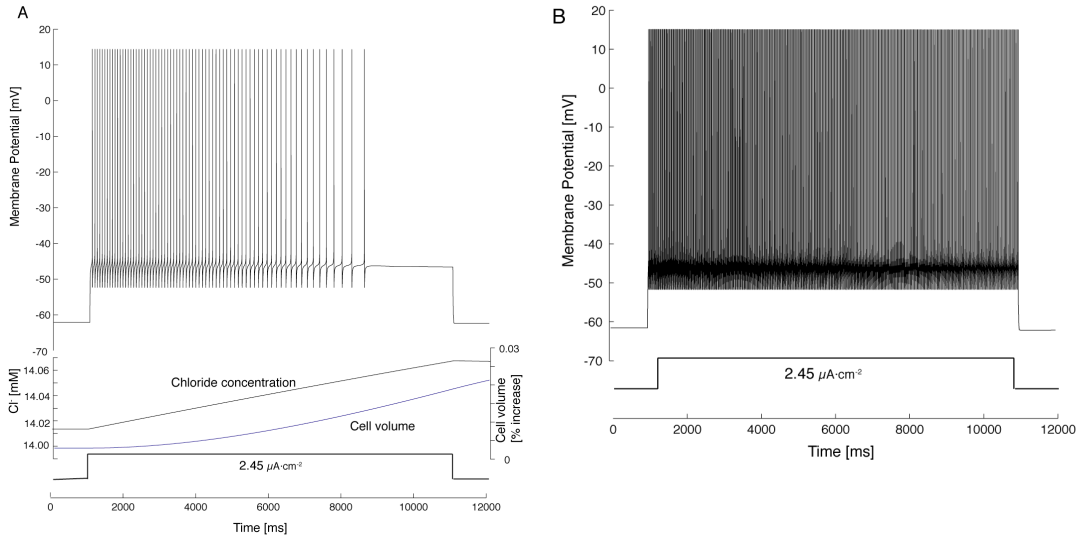

Figure 4.9 Effect of Cl in tonic spiking behavior.

A 10 s stimulus of an applied current (bottom panel) causes spiking behavior (top panel); however, Cl^- accumulation (black trace middle panel) leads to cessation of spiking conditions. The gradual increase of Cl^- decreases cell excitability due to hyperpolarization. When the stimulus is removed, Cl^- accumulation stops, and if integrated long enough restores baseline conditions after a few minutes (not shown in figure). Cell volume changes accompany the increase in Cl^- concentration (blue trace in middle panel, left column) although they are not very significant (0.03%); if uncontrolled, however, they can become pretty large after long-term simulations. ***B.*** the same applied current (bottom panel) when the chloride permeability set to zero causes tonic stable spiking.

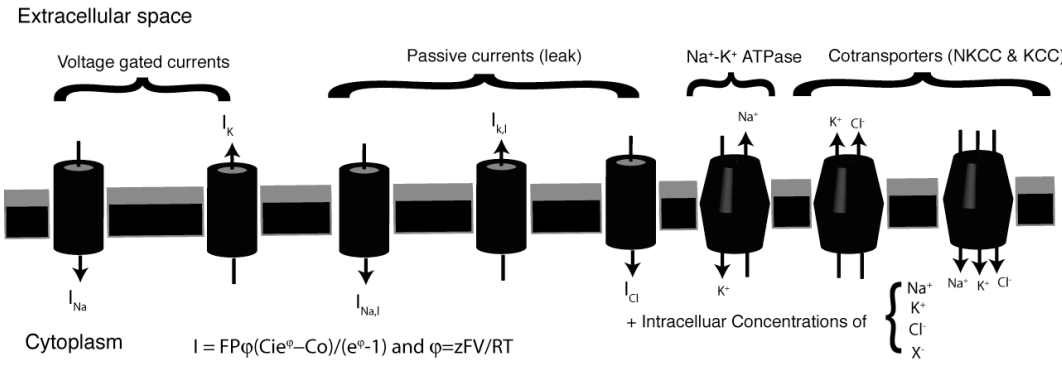

Figure 4.10 Addition of Cl pathways and volume regulation mechanisms.

As before, the model contains 2 voltage sensitive channels (I_{Na} and I_K) and a leak current divided in Na^+ ($I_{Na,l}$) , K^+ ($I_{K,l}$) and Cl^- (I_{Cl}) components. The model includes the Na^+/K^+ ATPase and follows intracellular concentrations of Na^+, K^+, Cl^- and X^-. In addition, the dynamics of the KCC and NKCC cotransporters (pathways for Cl^- that help maintain cell volume and allow for tonic spiking behaviors) were added to the model.

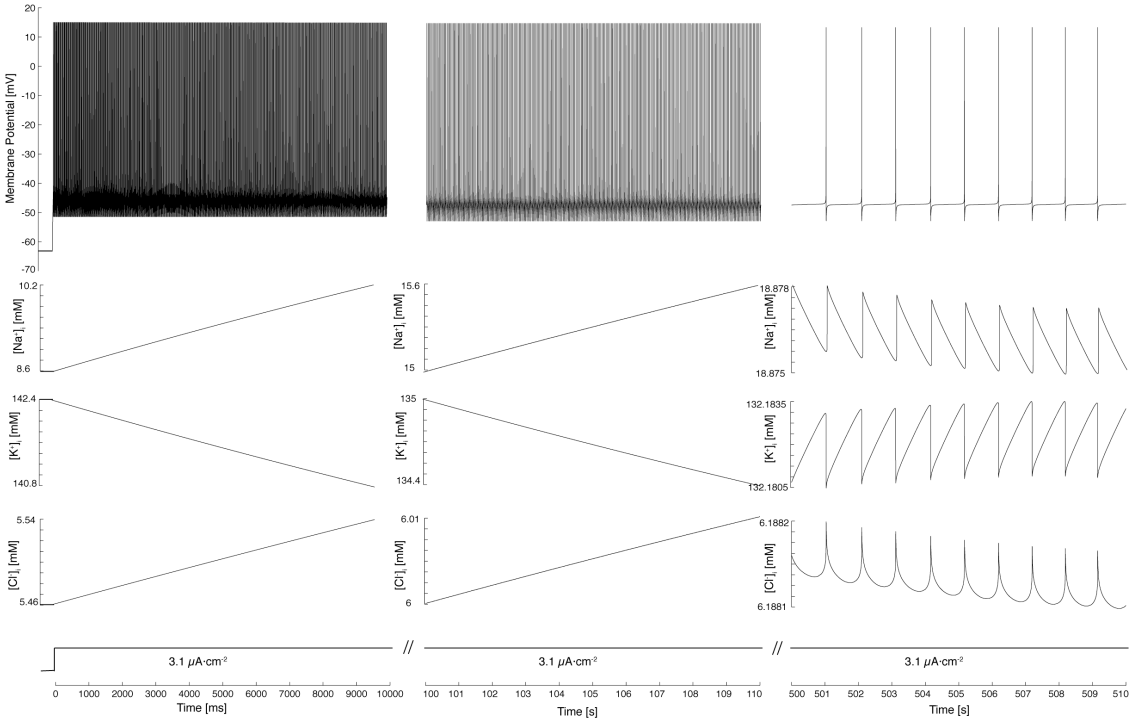

Figure 4.11 Numerical integration of the permeability-based model with Cl^- pathways and volume regulation mechanisms.

Three different moments (one per column) during a ~9 minute integration of 10 second each show the transition of the membrane potential (first row), Na^+ concentration (second row) K^+ concentration (third row), Cl^- concentration (fourth row) as the model is subject to an applied current (last row). Tonic spiking at considerable lower firing rates is achieved after approximately 8 minutes, before that Na^+ increases, K^+ decreases and Cl^- increases until they achieve that dynamical steady state that accompanies the changes in the membrane potential. Note that the scales for the concentrations changes as the simulation progresses.

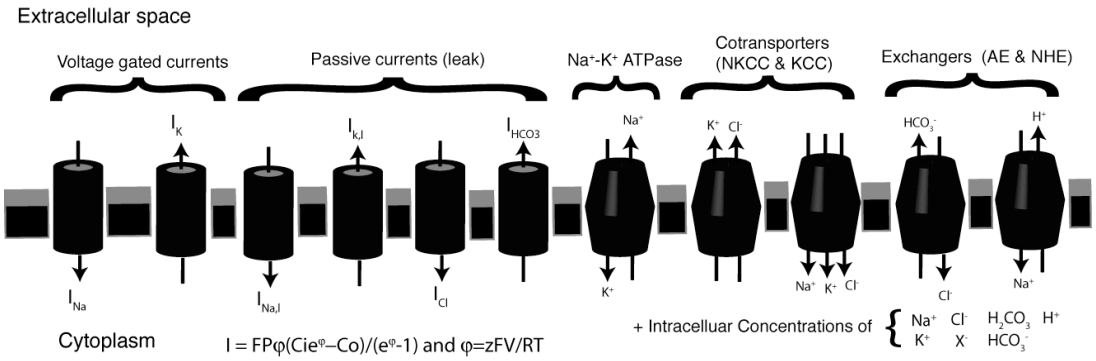

Figure 4.12 elements of the coupled transport-excitable cell model.

The model contains 2 voltage sensitive channels (I_{Na} and I_K) and a leak current divided in Na^+ ($I_{Na,l}$) , K^+ ($I_{K,l}$), Cl^- (I_{Cl}) and HCO_3^- (I_{HCO3}) components. The model includes the active transport of the Na^+/K^+ ATPase and follows intracellular concentrations of Na^+, K^+, Cl^- , H_2CO_3, HCO_3^-, H^+ and X^-. As before the model includes the KCC and NKCC cotransporters to help maintain cell volume and Cl^- regulation. In addition the model has a pH regulation component that includes the NHE and AE, a chemical flux of H_2CO_3 due rapid diffusion of CO_2 across the cell membrane and enzymatic activity of carbonic anhydrase (not shown in figure).

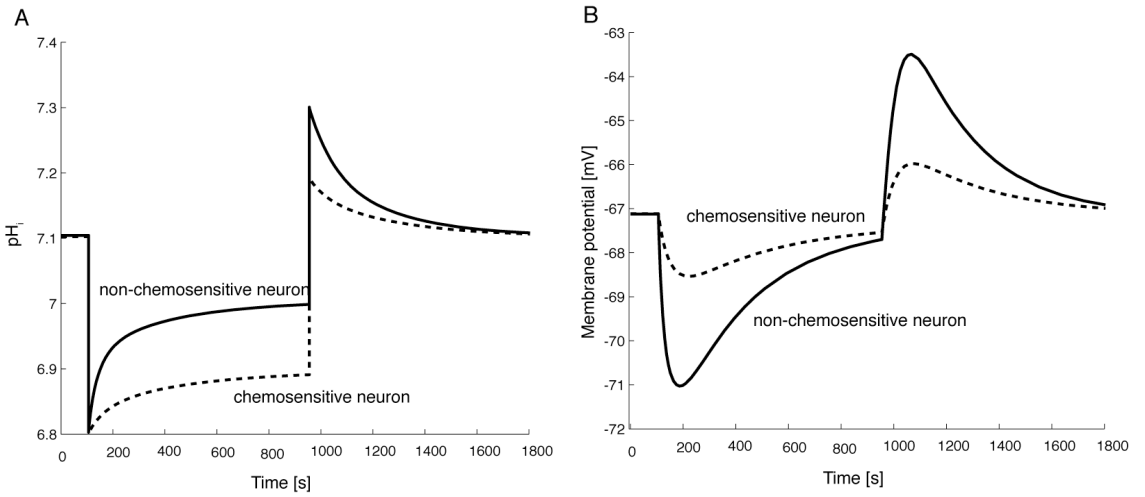

Figure 4.13 Comparison of chemosensitive vs. non-chemosensitive neurons during hypercapnic acidosis

A. pH_i and **B** membrane potential. The chemosensitive neuron (dashed line on both panels) shows blunted pH response in comparison to the non-chemosensitive (solid line). At the same time the membrane potential changes of the chemosensitive neuron are less compared to those of the non-chemosensitive. The chemosensitive neuron has an NHE that is less sensitive to intracellular H^+.

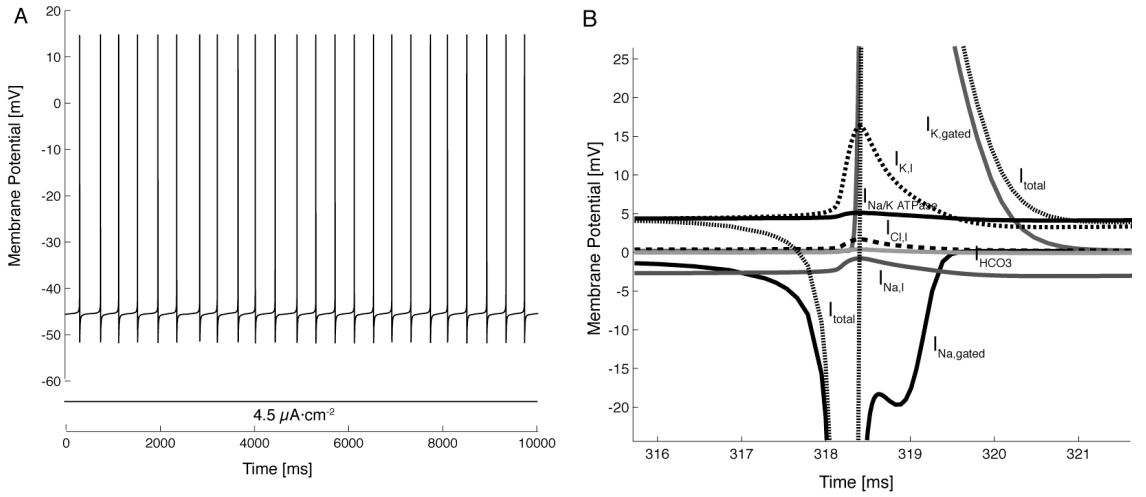

Figure 4.14 The transport-excitable model under spiking conditions.

A. Spiking trace. Application of a depolarizing current of 4.5 $\mu A \cdot cm^{-2}$ generates a series of AP. **B**. Single AP. The shape and duration of a single AP is the consequence of the balance of 7 currents, the more fundamental ones obviously being the voltage gated Na^+ and K^+ currents.

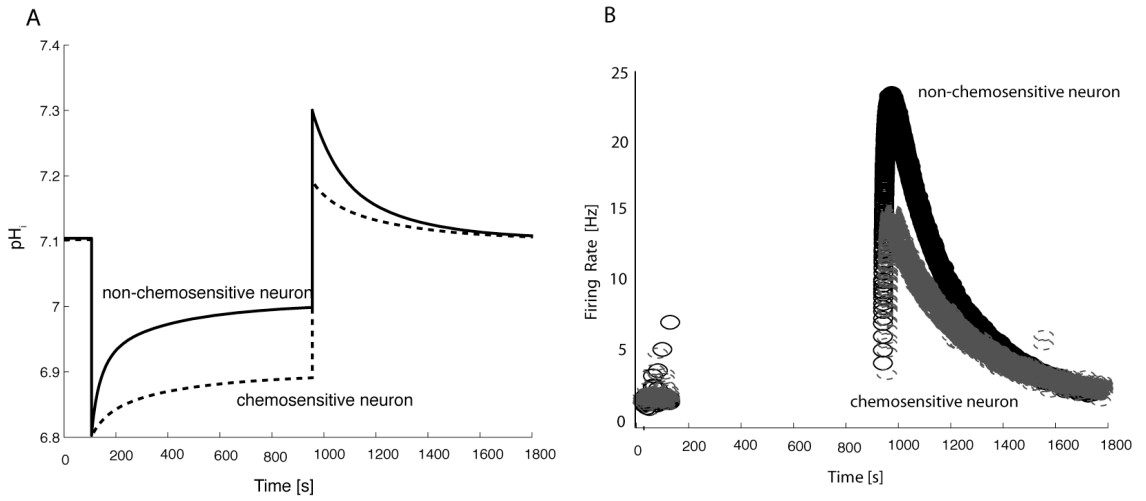

Figure 4.15 comparison of chemosensitive vs. non chemosensitive neurons during hypercapnic acidosis with spiking conditions.

A. pH_i. The chemosensitive neuron (dashed line) shows blunted response in comparison to the nonchemosensitive (solid line) very similar to to the response under resting conditions shown in figure (4.13). **B**. Firing Rate. The changes in firing rate, on the other hand are significantly different for both types of neurons, being lees excitable the chemosensitive neuron.

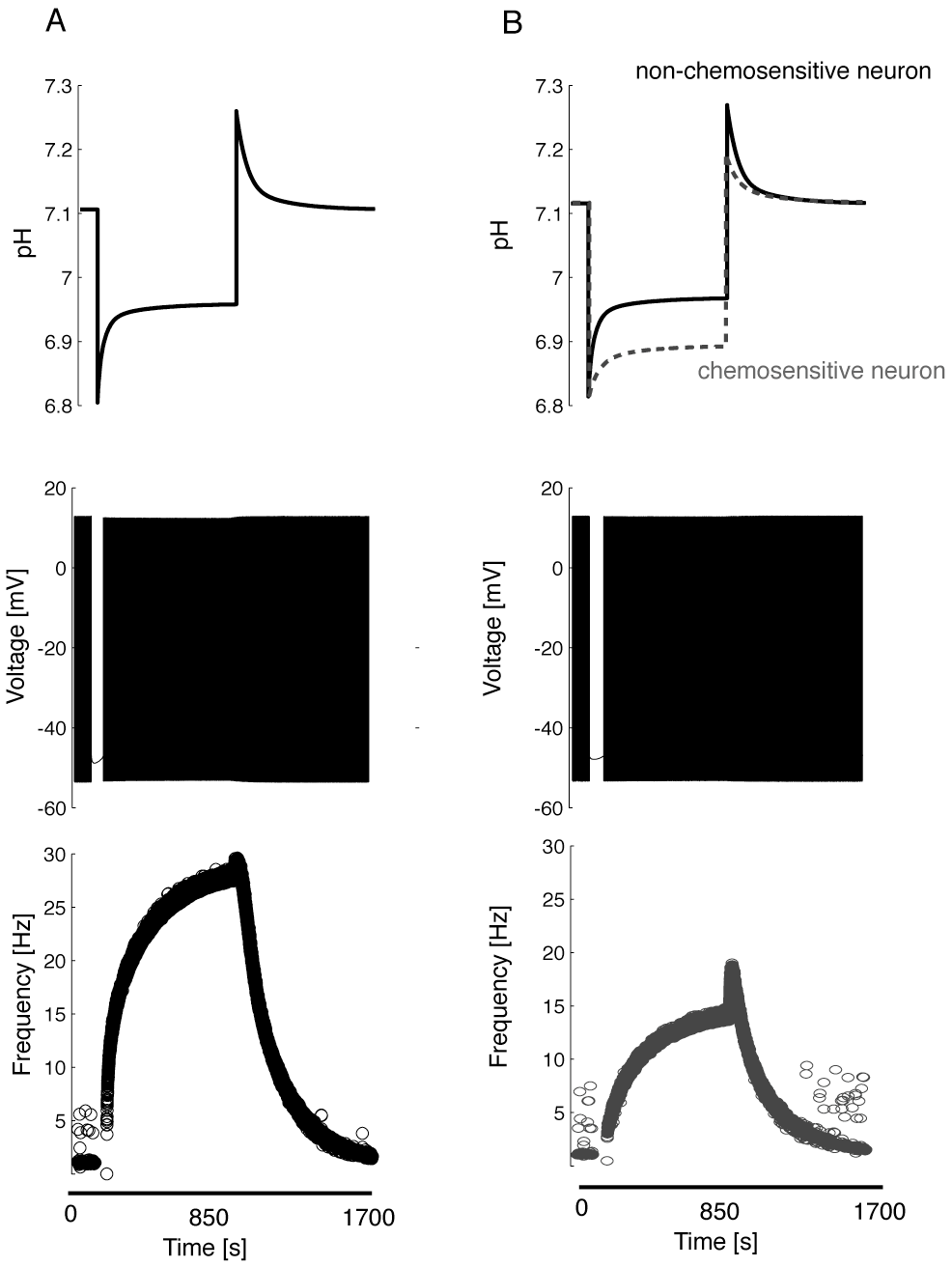

Figure 4.16 effect of increasing bicarbonate permeability on HA

A. non-chemosensitive and **B.** chemosensitive neurons. The pH response to HA is maintained and the differences between chemosensitive and non-chemosensitive neurons are preserved with increased bicarbonate permeability (top panel, solid black is non-chemosensitive and dashed gray is chemosensitive), however the effect of increasing the bicarbonate permeability is dramatic on membrane potential and FR, the neurons transitions from tonic slow spiking (2.4 Hz) to fast rates (up to 30Hz for non-chemosensitive and 20Hz for chemosensitive) suggesting that chemosensitivity could be a combination of signals.

Table 4.1 List of parameters for HH model.

Symbol	Meaning	Value
c_m	Total Cell capacitance	21 pF
E_{Na}	Nernst Equilibrium potential Na^+	70 mV
E_K	Nernst Equilibrium potential K^+	-85 mV
g_{Na}	Fast Na^+ conductance	28 nS
g_K	Delayed rectifier K^+ conductance	11.2 nS
$g_{Na,l}$	Leak Na^+ conductance	0.4 nS
$g_{K,l}$	Leak K^+ conductance	2.4 nS
θ_m	Half-activation for m_∞	-34 mV
σ_m	Half-width and slope for m_∞	-5 mV
θ_n	Half-activation for n_∞	-29 mV
σ_n	Half-width and slope for n_∞	-4 mV
τ_n	Time constant for n_∞	10 ms

Table 4.2 Parameters obtained for I_{Na} in permeability-based model using voltage clamp simulations and numerical optimization

Parameter	Meaning	Initial value	Final value
θ_m	Half activation for m_∞	-34	-33.96
σ_m	Half width and slope for m_∞	-5	-4.87
θ_n	Half activation for n_∞	-29	-29.06
σ_n	Half width and slope for n_∞	-4	-4.06
τ_n	Time constant for n_∞	10	9.95
P_{Na}	Na^+ permeability*	1	0.60

* Note that permeability is given in units of $C \cdot cm^{-1} \cdot mol^{-1} \cdot s^{-1}$.

Table 4.3 Parameters obtained for I_K in permeability-based model using voltage clamp simulations and numerical optimization

Parameter	Meaning	Initial value	Final value
θ_n	Half activation for n_∞	-29	-35.72
σ_n	Half width and slope for n_∞	-4	-4.04
τ_n	Time constant for n_∞	10	20.96
P_K	K^+ permeability *	1	0.32

* Note that permeability is given in units of $C \cdot cm^{-1} \cdot mol^{-1} \cdot s^{-1}$.

Table 4.4 Parameters obtained for $I_{K,l}$ and $I_{K,l}$ in permeability based model using curve fitting for relevant range of voltages

Parameter	Meaning	Initial value	Final value
$P_{Na,l}$	Leak Na^+ permeability *	0.1	0.0079
$P_{K,l}$	Leak K^+ permeability *	0.1	0.06

* Note that permeability is given in units of $C \cdot cm^{-1} \cdot mol^{-1} \cdot s^{-1}$.

Table 4.5 Parameters for permeability-based model after voltage clamp simulations and numerical optimization.

Symbol	Meaning	Value
c_m	Membrane capacitance	1 μF cm^{-2}
C^i_{Na}	Intracellular Na^+	10 mM
C^o_{Na}	Extracellular Na^+	140 mM
C^i_K	Intracellular K^+	140 mM
C^o_K	Extracellular K^+	5 mM
P_{Na}	Fast Na^+ Permeability	6.22 x 10^{-6} cm·s^{-1}
P_K	delayed rectifier K^+ permeability	3.32 x 10^{-6} cm·s^{-1}
$P_{Na,l}$	Leak Na^+ permeability	8.20 x 10^{-8} cm·s^{-1}
$P_{K,l}$	Leak K^+ permeability	6.22 x 10^{-7} cm·s^{-1}
θ_m	Half activation for m_∞	-34 mV
σ_m	Half width and slope for m_∞	-5 mV
θ_n	Half activation for n_∞	-29 mV
σ_n	Half width and slope for n_∞	-4 mV
τ_n	Time constant for n_∞	10 ms

Table 4.6 Steady-state value after numerical integration of the models under resting and spiking conditions.

Steady State - $I_{app} = 0$			Spiking		
Variable	Model 1	Model 2	Variable	Model 1	Model 2
V	-62.65 mV	-47.67 mV	FR	9 Hz	70 Hz
n	0.0002	0.0093	Amplitude	60 mV	40 mV

Table 4.7 Parameters obtained for $I_{K,l}$ and $I_{K,l}$ in permeability based model after geometrical analysis

Parameter	Meaning	previous value	adjusted value
$P_{Na,l}$	Leak Na^+ permeability	0.0079	0.005
$P_{K,l}$	Leak K^+ permeability	0.06	0.09

Table 4.8 New parameters for the permeability based model that incorporates passive diffusion of ions*

Symbol	Meaning	Value
P_{Cl}	Cl^- permeability	1.03×10^{-7} cm·s^{-1}
P_X	X^- permeability	0 cm·s^{-1}
C^o_{Na}	Extracellular Na^+	145 mM
C^o_K	Extracellular K^+	5 mM
C^o_{Cl}	Extracellular Cl^-	140 mM
C^o_X	Extracellular X^-	10 mM
i_{max}	Maximum Na^+/K^+ pump current	5 µA/µF
K_{Na}	half saturation concentration for Na^+ on Na^+/K^+ pump model	10 mM
K_K	half saturation concentration for K^+ on Na^+/K^+ pump model	1.5 mM

*these parameters complement, and are in addition to, the already defined in Table 4.5 and Table 4.7.

Table 4.9 Numerical integration of the model and adjustment of ion permeabilities to achieve normal resting membrane potentials and adequate intracellular concentrations of the ions.

Steady State - $I_{app} = 0$			Permeabilities for simulation 1 and 2 x Farady's constant ($C \cdot cm \cdot sec^{-1} \cdot mol^{-1}$)		
Variable	Simulation 1	Simulation 2	Variable	Simulation 1	simulation 2
V	-71.63 mV	-61.55 mV	P_{Na}	0.6	1.8
n	0.00002	0.0003	P_K	0.32	0.9
W	9.2×10^{-8} mm^3	9.2×10^{-8} mm^3	$P_{Na,l}$	0.005	0.009
C^i_{Na}	5.53 mM	8.13 mM	$P_{K,l}$	0.09	0.09
C^i_K	145.49 mM	142.87 mM	P_{Cl}	0.01	0.01
C^i_{Cl}	9.78 mM	13.99 mM	P_X	0	0
C^i_X	139.18 mM	135 mM			

Table 4.10 New parameters for permeability-based model that incorporate Cl^- pathways and volume regulation*

Symbol	Meaning	Value
E_{NKCC}	Expression of Enzyme (moles of ions exchanged per mol of cotransporter)	1×10^{-7}
E_{KCC}	Expression of Enzyme (moles of ions exchanged per mol of cotransporter)	8×10^{-7}

*these parameters complement, and are in addition to, the already defined in Table 4.5, Table 4.7 and Table 4.8

Table 4.11 Numerical integration of the model and comparison with result obtained before adding the Cl^- and volume regulation pathways (previous instance of the model)

Variable	Steady State value (with Cl^- pathways)	Steady State value (before the addition of Cl^- pathways)
V	-63.33 mV	-61.55 mV
n	0.00002	0.0003
W	9.2×10^{-8} mm^3	9.2×10^{-8} mm^3
C^i_{Na}	8.75 mM	8.13 mM
C^i_K	142.29 mM	142.87 mM
C^i_{Cl}	5.46 mM	13.99 mM
C^i_X	143.47 mM	135 mM

Table 4.12 Additional and re-adjusted parameters for transport-excitable model

Symbol	Meaning	Value (units)
C_{CO2}	Level of Carbonic acid (changes for different perturbations)	40 (mmHg) Normocapnia 80 (mmHg) Hypercapnia
k_h	hydration rate for CO_2 in reaction: $CO_2+H_2O \rightleftharpoons H_2CO_3$	0.18 (s^{-1})
k_d	dehydration rate for CO_2 in reaction: $CO_2+H_2O \rightleftharpoons H_2CO_3$	64 (s^{-1})
K_{HCO3}	Equilibrium constant for Bicarbonate Buffer	0.34 (mM)
P_{HCO3}	HCO_3^- permeability	0.01 ($C \cdot cm \cdot s^{-1} \cdot mol^{-1}$)
P_H	H^+ permeability	0 ($C \cdot cm \cdot s^{-1} \cdot mol^{-1}$)
E_{NHE}	Expression of Enzyme	2
E_{AE}	Expression of Enzyme	1×10^{-8}
i_{max}	Maximum Na^+/K^+ pump current	15 μA/μF
$P_{Na,l}$	Leak Na^+ permeability	0.01 ($C \cdot cm \cdot s^{-1} \cdot mol^{-1}$)
C_{Cl}^o	Extracellular Cl^-	125 (mM)
C_X^o	Extracellular X^-	0 (mM)
C_{H2CO3}^o	Extracellular H_2CO_3	0.0034 (mM)
C_{HCO3}^o	Extracellular HCO_3^-	23.99 (mM)
C_H^o	Extracellular H (pH)	7.4

*these parameters complement redefine and/or are in addition to, the already defined in Table 4.5, Table 4.7, Table 4.8 and Table 4.10.

Table 4.13 Numerical integration of the model and comparison with result obtained before adding the pH regulation component (previous instance of the model)

Variable	State state value (with pH regulation)	Steady State value(before pH regulation)
V	-67.12 mV	-63.33 mV
n	0.00001	0.00002
W	$9.2x10^{-8}$ mm^3	$9.2x10^{-8}$ mm^3
C^i_{Na}	7.71 mM	8.75 mM
C^i_K	141.77 mM	142.29 mM
C^i_{Cl}	14.99 mM	5.46 mM
C^i_X	0.0034 mM	not a state variable
C^i_{H2CO3}	14.58 MM	not a state variable
C^i_{HCO3}	$pH_i = 7.1$	not a state variable
C^i_X	119.93 mM	143.47 mM

Table 4.14 Numerical integration of the transport-excitable model with I_{app} = 4.5 μA·cm^{-2}

Variable	Steady State - I_{app} = 4.5	Steady State - I_{app} = 0
V	spiking FR = 2.5 Hz	-63.33 mV
n	varies	0.00002
W	9.2×10^{-8} mm^3	9.2×10^{-8} mm^3
C^i_{Na} *	9.66 mM	7.71 mM
C^i_K *	139.82 mM	141.77 mM
C^i_{Cl} *	14.63 mM	14.99 mM
C^i_X *	0.0034 mM	0.0034 mM
C^i_{H2CO3} *	14.62 MM	14.58 MM
C^i_{HCO3} *	pH_i = 7.1	pH_i = 7.1
C^i_X *	118.83 mM	119.93 mM

*Note that state variables change slightly during the AP so the values on the table are average values.

Chapter 5 - Future Work

There has been a long debate about the role of intracellular pH (pH_i) or extracellular pH (pH_o) as the main signal for hypercapnia, but there is evidence that both pH_i and pH_o could be acting as independent stimuli (83). In principle, pH_i and pH_o could affect independently the ability of acid-base regulation transporters to move ions across the cell membrane. One possibility for chemosensitive neurons is to have an NHE that is both less sensitive to pH_i and more sensitive to pH_o; thus, during HA, the decrease pH_i and pH_o would strongly prevent pH_i regulation. This idea is feasible, and can be be tested using a mathematical model. Furthermore, this approach would allow for identification of what, if anything, would be the effect of such a change on the membrane potential response to HA.

We want to compare our model to the recently published models for central chemosensitivity. For this purpose, we will include all the voltage- and pH-sensitive currents described in these models, but will retain our pH regulation component and passive diffusion of the ions. In this way, we can better quantify the effects of the GHK description of the currents and the effects that ionic concentration changes have in excitability.

Ideally, the model should be able to point to possible characteristics of chemosensitive neurons that then can be corroborated using experimental techniques. For example, the model suggests a NHE sensitivity to pH_i; therefore, it would be important to determine the characteristics of the NHE in central CO_2 chemosensitive neurons.

The model also revealed that HCO_3^- might be part of the chemosensitivity response. Thus comparison of HCO_3^- conductance between chemosensitive and non-chemosensitive neurons seems to be an attractive experiment.

In addition to all of the cellular elements described in this document, some elements are still missing, and we believe that their contributions are important to test. Some of these elements include:

- Na^+ dependent Cl^-/HCO_3^- exchanger
- TASK channels
- I_{CAN} Current
- Type A K^+ current
- Ca^{++} activated potassium current
- Persistent Na^+ current.
- Na^+-Ca^{++} Exchanger
- Ca^{++} Pump

As mentioned repeatedly, we want to update our current models for cotransporters and voltage-gated descriptions with recent data that is more relevant to neurons in the brainstem, and when possible, measurements from chemosensitive and non-chemosensitive neurons.

Finally, we also want to extend our analysis to neurons in different chemosensitive areas of the brainstem. Different regions seem to be characterized by different cellular elements that could be potentially be doing the same job by different, but comparable, means. Regions of interest include the RTN, LC, pre-BötC, and VLM.

References

1. **Aharonovitz O, Kapus A, Szászi K, Coady-Osberg N, Jancelewicz T, Orlowski J, and Grinstein. S**. Modulation of Na+/H+ exchange activity by Cl *Am J Physiol Cell Physiol* 281: C133 - C141, 2001.
2. **Amin-Naves J, Giusti H, and Hoffmann A**. Central ventilatory control in the south american lungfish, *Lepidosiren paradoxa*: contributions of pH and CO_2. *Journal of Comparative physiology* 177: 529-534, 2007.
3. **Arita H, Ichikawa K, Kuwana S, and Kogo N**. Possible Locations of pH-dependent central chemoreceptors: intramedullary regions with acidic shift of extracellular fluid pH during hypercapnia. *Brain research* 485: 285 -293, 1989.
4. **Aronson P, Suhm M, and Nee J**. Interaction of external H+ with the Na+-H+ exchanger in renal microvillus membrane vesicles. . *J Biol Chem* 258: 6767 - 6771, 1983.
5. **Aronson PS**. Kinetic properties of the plasma membrane Na^+-H^+ exchanger. *Annual reviews in Physiology* 47: 545-560, 1985.
6. **Aronson PS, Nee J, and Suhm MA**. Modifier role of internal H^+ in activating the Na^+/H^+ exchanger in renal microvillus membrane vesicles. *Nature* 299: 161-163, 1982.
7. **Attaphitaya S, Nehrke K, and Melvin JE**. Acute inhibition of brain-specific Na^+/H^+ exchanger isoform 5 by protein kinases A and C and cell shrinkage. *AJP - Cell Physiology* 281: C1146-C1157, 2001.
8. **Bayliss DA, Talley EM, Sirois JE, and Lei Q**. TASK-1 is a highly modulated pH-sensitive [`]leak' K+ channel expressed in brainstem respiratory neurons. *Respiration Physiology* 129: 159-174, 2001.
9. **Bebout DE, and Hempleman SC**. Chronic hypercapnia resets CO_2 sensitivity of avian intrapulmonary chemoreceptors. *AJP - Regulatory Integrative Comparative Physiology* 276: R317 - R322, 1999.
10. **Benjamin B, and Johnson E**. A quantitative description of the Na-K-2Cl cotransporter and its conformity to experimental data. *Am J Physiol* F473 - F482, 1997.
11. **Berg J, and Tymoczko J**. Biochemestry. *WH Freeman and Co* %th Edition: 2002.
12. **Berger MG, Vandier C, Bonnet P, Jackson WF, and Rusch NJ**. Intracellular acidosis differentially regulates KV channels in coronary and pulmonary vascular muscle. *AJP - Heart and Circulatory Physiology* 275: H1351-1359, 1998.
13. **Bernard DG, Li A, and Nattie E**. Evidence for central chemoreception in the midline raphe. *Journal of Applied Physiology* 80: 108-115, 1996.

14. **Bevensee MO, and Boron WF**. Effects of acute hypoxia on intracellular-pH regulation in astrocytes cultured from rat hippocampus. *Brain research* 1193: 143-152, 2008.

15. **Bickler PE, Litt L, Banville DL, and Severinghaus JW**. Effects of acetazolamideon on cerebral acid base balance. *J Appl Physiol* 65: 422 - 427, 1988.

16. **Boron WF**. Intracellular pH regulation in epithelial cells. *Annual reviews in Physiology* 48: 377 - 388, 1986.

17. **Boron WF**. Regulation of intracellular pH. *Advances in Physiology Education* 28: 160-179, 2004.

18. **Boron WF, and Boulpaep EL**. Intracellular pH regulation in the renal proximal tubule of the salamander. Basolateral HCO3- transport. *The Journal of General Physiology* 81: 53-94, 1983.

19. **Bouyer PG, Bradley SR, Zhao J, Wang W, Richerson GB, and Boron WF**. Effect of extracellular acid-base disturbances on the intracellular pH of neurons cultured from rat medullary raphé or hippocampus. *Jounal of Physiology* 559: 85-101, 2004.

20. **Bruehl C, and Witte OW**. Relation Between Bicarbonate Concentration and Voltage Dependence of Sodium Currents in Freshly Isolated CA1 Neurons of the Rat. *Journal of Neurophysiology* 89: 2489-2498, 2003.

21. **Busa WB**. Mechanisms and consequences of pH-mediated cell regulation. *Annual reviews in Physiology* 48: 389 - 402, 1986.

22. **Butera RJ, Jr., Rinzel J, and Smith JC**. Models of respiratory rhythm generation in the pre-Botzinger complex. II. Populations Of coupled pacemaker neurons. *Journal of neurophysiology* 82: 398-415, 1999.

23. **Chang H, and Fujita T**. A numerical model of acid-base transport in rat distal tubule. *AJP - Renal Physiology* 281: F222-F243, 2001.

24. **Chang H. FT**. A numerical model of acid-base transport in rat distal tubule. . *The American Physiological Society* F222 – F243, 2001.

25. **Chernov MM, Daubenspeck JA, Denton JS, Pfeiffer JR, Putnam RW, and J.C.Leiter**. A computational analysis of central CO_2 chemosensitivity in *Helix aspersa*. *AJP - Cell Physiology* 292: 278-291, 2007.

26. **Chesler M**. Regulation and modulation of pH in the brain. *Physiological Reviews* 83: 1183-1221, 2003.

27. **Church J, Baxter KA, and McLarnon JG**. pH modulation of Ca2+ responses and a Ca2+-dependent K+ channel in cultured rat hippocampal neurones. *The Journal of Physiology* 511: 119-132, 1998.

28. **Clay JR**. A paradox concerning ion permeation of the delayed rectifier potassium ion channel in squid giant axons. *J Physiol* 444: 499-511, 1991.

29. **Clay JR**. Excitability of the squid giant axon revisited. *Journal of neurophysiology* 80: 903-913, 1998.

30. **Clay JR, Paydarfar D, and Forger DB**. A simple modification of the Hodgkin and Huxley equations explains type 3 excitability in squid giant axons. *Journal of The Royal Society Interface* 5: 1421-1428, 2008.

31. **Coates EL, Li A, and Nattie E**. Widespread sites of brain stem ventilatory chemoreceptors. *Journal of Applied Physiology* 71: 5 -14, 1993.

32. **Collip JB**. The sub-arachnoid and intra-arterial administration of sodium bicarbonate and other electrolytes. *American Journal of Physiology* 52: 483 - 498, 1920.

33. **Corcoran AE, Hodges MR, Wu Y, Wang W, Wylie CJ, Deneris ES, and Richerson GB**. Medullary serotonin neurons and central CO2 chemoreception. *Respiratory Physiology & Neurobiology* 168: 49-58, 2009.

34. **Cordovez JM, Clausen C, Moore LC, and Solomon IC**. A mathematical model of pH_i regulation in central CO_2 chemoreception. *Advances in Experimental Medicine and Biology - Springer New York* 605: 306-311, 2008.

35. **Dean JB, Bayliss DA, Erickson JT, Lawing WL, and Millhorn DE**. Depolarization and stimulation of neurons in nucleus tractus solitarii by carbon dioxide does not require chemical synaptic input. *Neuroscience* 36: 207-216, 1990.

36. **Del Negro CA, Johnson SM, Butera RJ, and Smith JC**. Models of respiratory rhythm generation in the pre-Botzinger complex. III. Experimental tests of model predictions. *Journal of neurophysiology* 86: 59-74, 2001.

37. **Del Negro CA, Kam K, Hayes JA, and Feldman JL**. Asymmetric control of inspiratory and expiratory phases by excitability in the respiratory network of neonatal mice in vitro. *The Journal of physiology* 587: 1217-1231, 2009.

38. **Dev NB, and Loeschcke HH**. A cholinergic mechanism involved in the respiratory chemosensitivity of the medulla oblongata in the cat. *Pflügers Archives* 379: 29 - 36, 1979.

39. **Douglas RM, Trouth CO, Pan Y, Mckenzie JC, and Winston n S**. Identification of brainstem H+ - ion-chemosensitive regions by c-fos immunocytochemestry. *Book chapter - find reference* 1993.

40. **Duffin J**. Functional organization of respiratory neurones: a brief review of current questions and speculations. *Experimental Physiology* 89: 517 - 529, 2004.

41. **Duffin J**. Modelling the respiratory chemoreflex control of Acid-base balance. *Conf Proc IEEE Eng Med Biol Soc* 6: 5836-5839, 2005.

42. **Duffin J**. Role of Acid-Base balance in the chemoreflex control of breathing. *Journal of Applied Physiology* 99: 2255-2265, 2005.

43. **Eric R. Kandel, James Harris Schwartz, and Thomas m. Jessell**. Principles of Neural science. *McGraw-Hill* 4th Edition: 2000.

44. **Feldman**. Breathing: Rhytmicity, Plasticity, Chemosensitivity. *Annual reviews in Neuroscience* 26: 239-266, 2003.

45. **Feldman JL, and Ellenberger HH**. central coordination of respiratory and cardiovascular control in mammals. *Annual reviews in Physiology* 50: 593 - 606, 1988.

46. **Filosa JA, Dean JB, and Putnam RW**. Role of intracellular and extracellular pH in the chemosensitive response of rat locus coeruleus neurons. *Jounal of Physiology* 541: 493-509, 2002.

47. **Filosa JA, and Putnam RW**. Multiple targets of chemosensitive signaling in locus coeruleus neurons: role of K+ and Ca2+ channels. *AJP - Cell Physiology* 284: C145-155, 2003.

48. **Fukuda Y, and Loeschcke HH**. A cholinergic mechanism involved in the neuronal excitation by H+ in the respiratory chemosensitive structures of the ventral medulla oblongata of rats in vitro. *Pflügers Archives* 379: 125 - 135, 1979.

49. **Gadsby DC, Bahinski A, Nakao M, Joseph FH, and Gerhard G**. Chapter 14 Voltage Dependence of Na/K Pump Current. In: *Current Topics in Membranes and Transport*Academic Press, 1989, p. 269-288.

50. **Gasbjerg P, Knauf P, and Brahm J**. Kinetics of the bicarbonate transport in human red blood cells membranes at body temperature. *J gen Physiol* 108: 565-575, 1996.

51. **Gaultier C, and Gallego J**. Development of respiratory control: Evolving concepts and perspectives. *Respiratory physiology and Neurobiology* 149: 3-15, 2005.

52. **Goldman DE**. Potential, impedance, and rectifcation in membranes. *J Gen Physiol* 27: 37 - 60, 1943.

53. **Goldstein JI, Mok JM, Simon CM, and Leiter JC**. Intracellular pH regulation in neurons from chemosensitive and nonchemosensitive regions of *Helix aspersa*. *AJP - Regulatory Integrative Comparative Physiology* 279: R414 - R423, 2000.

54. **Gray Js**. The multiple factor theory of the control of respiratory ventilation. *Science* 103: 739 - 744, 1946.

55. **Guckenheimer J, and Holmes P**. Nonlinear Oscillations, Dynamical Systems and Bifurcations of Vector Fields. *AMS Springer-Verlag, New York* 42: 1983.

56. **Guyenet PG**. The 2008 Carl Ludwig Lecture: retrotrapezoid nucleus, CO2 homeostasis, and breathing automaticity. *J Appl Physiol* 105: 404-416, 2008.

57. **Guyenet PG, Mulkey DK, Stornetta RL, and Bayliss DA**. Regulation of Ventral Surface Chemoreceptors by the Central Respiratory Pattern Generator. *The Journal of Neuroscience* 25: 8938-8947, 2005.

58. **Guyenet PG, Stornetta RL, Bayliss DA, and Mulkey DK**. Retrotrapezoidal nucleus: a litmus test for the identification of central chemoreceptors. *Experimental Physiology* 90: 247-257, 2005.

59. **Haldane JS, Kellas AM, and Kennaway EL**. *Journal of physiology* 1iii: 181, 1919.

60. **Hepleman SC, Adamson TP, Begay RS, and Solomon IC**. CO_2 transduction in avian intrapulmonary chemoreceptors is critically dependent on transmemebrane Na^+/H^+ exchange. *AJP - Regulatory Integrative Comparative Physiology* 284: 1551-1559, 2002.

61. **Heymans C**. A look at an old but still current problem. *Annual reviews in Physiology* 25: 1-16, 1963.

62. **Heymans C**. Chemoreceptors and regulation of respiration. *Acta Physiol Scand* 22: 1-13, 1951.

63. **Heymans C, De Vleeschhouwer GR, and De Schaepdryver AF**. [The cerebrospinal fluid and stimulation of respiration by CO-2]. *J Physiol (Paris)* 57: 627-628, 1965.

64. **Hille B**. Ion channels of excitable membranes. *Sinauer associates, Inc* 2001.

65. **Hodgkin AL, and Katz B**. The effect of sodium ions on the electrical activity of the giant axon of the squid. *J Physiol* 108: 37 - 77, 1949.

66. **Hodgkin L, and Huxley AF**. A quantitative description of membrane current and its application to conduction and excitation in nerve. *Journal of Physiology* 117: 500 - 544, 1952.

67. **Issa FG, and Remmers JE**. Identification of a subsurface area in the ventral medulla sensitive to local changes in P_{CO2}. *Journal of Applied Physiology* 72: 439 - 446, 1992.

68. **Itada N, and Forster RE**. Carbonic anhydrase activity in intact red blood cells measured with 18O exchange. *Journal of Biological Chemistry* 252: 3881-3890, 1977.

69. **Izhikevich EM**. Dynamical Systems in Neuroscience: The geometry of excitability and bursting. *MIT Press* 2007.

70. **JF. H, and C. H**. Sur les modifications directes et sur la regulation reflexe de l'activite du centre respiratoire de lat tete isolee du

chien. *Arch Int Pharmacodyn Ther* 33: 273–372, 1927.

71. **Jiang C, Rojas A, Wang R, and Wang X**. CO2 central chemosensitivity: why are there so many sensing molecules? *Respiratory physiology and Neurobiology* 145: 115-126, 2004.

72. **Kaila K, and Ransom B**. pH and brain function. *Wiley-Liss, Inc* 1998.

73. **Kersh AE, Hartzler LK, Havlin K, Hubbell BB, Nanagas V, Kalra A, Chua J, Whitesell R, Ritucci NA, Dean JB, and Putnam RW**. pH regulating transporters in neurons from various chemosensitive brainstem regions in neonatal rats. *Am J Physiol Regul Integr Comp Physiol* 2009.

74. **Kinney H, Randall L, Sleeper L, Willinger M, Belliveau R, Zec N, Rava L, Dominici L, Iyas S, Randall B, Habbe D, Wilson H, Mandell F, McClain M, and Welty T**. Serotonergic brainstem abnormalities in Northern Plains Indians with the sudden infant death syndrome. *Journal of Neuropathology and Experimental Neurology* 62: 1178-1191, 2003.

75. **Kneppper M**. NH4+ transport in the kidney. *Kidney Int suppl* 33: S95 - 102, 1991.

76. **Kogo N, and Arita H**. In vivo study on medullary H^+ sensitive neurons. *Journal of Applied Physiology* 69: 1408 - 1412, 1990.

77. **Kondo T, Kumagai M, Ohta Y, and Bishop B**. Ventilatory responses to hypercapnia and hypoxia following chronic hypercapnia in the rat. *Respiration Physiology* 122: 35-43, 2000.

78. **Lahiri S, Baby SM, Giulio CD, and Roy A**. CO2/H Homeostasis: Role of Central and peripheral Chemoreceptors. *Book chapter - find reference* 2007.

79. **Lahiri S, Baby SM, Giulio CD, and Roy A**. CO2/H Homeostasis: Role of Central and peripheral Chemoreceptors in adult mammals. *Handbook of Neurochemestry and molecular neurobiology* Springer US: 229 - 240, 2007.

80. **Lahiri S, and Forster RE**. CO2/H+ sensing: peripheral and central chemoreception. *The International Journal of Biochemistry & Cell Biology* 35: 1413-1435, 2003.

81. **Lahiri S, and Forster RE**. CO_2/H^+sensing: peripheral and central chemoreception. *The International Journal of Biochemestry & Cell Biology* 35: 1413 - 1435, 2003.

82. **Lauf PK, and Adragna NC**. K-Cl cotransport: properties and molecular mechanism. *Cell Physiol Biochem* 10: 341-354, 2000.

83. **Leiter JC**. Intrinsic chemosensitivity: How is it measured; what does it mean; and how does it help us understand the ventilatory response to CO2? *Respiratory Physiology & Neurobiology* 166: 13-15, 2009.

84. **Leusen I**. Regulation of cerebrospinal fluid composition with reference to breathing. *Physiological Reviews* 52: 1- 56, 1972.

85. **Li A, and Nattie EE**. Focal central chemoreceptor sensitivity in the RTN studied with a CO2 diffusion pipette in vivo. *J Appl Physiol* 83: 420-428, 1997.

86. **Loeschcke HH**. Central Chemosensitivity and the reaction theory. *Journal of Physiology* 332: 1-24, 1982.

87. **Luo CH, and Rudy Y**. A dynamic model of the cardiac ventricular action potential. I. Simulations of ionic currents and concentration changes. . *Circ Res* 74: 1071-1096., 1994.

88. **Lytle C, and Manus TM**. A minimal kinetic model of [Na-K-2Cl] cotransport with ordered binding and glide symmetry. . *J Gen Physiol* 88: 1986.

89. **Ma E, and Haddad GG**. Expression and localization of Na+/H+ exchangers in rat central nervous system. *Neuroscience* 79: 591-603, 1997.

90. **Marcano M, Yang H-M, Nieves-González A, Clausen C, and Moore LC**. Parameter estimation for mathematical models of NKCC2 cotransporter isoforms. . *Am J Physiol Renal Physiol* 296: F369-F381, 2009.

91. **Mercado A, Song L, Vazquez N, Mount D, and G. G**. Functional comparison of the K+-Cl- cotransporters KCC1 and KCC4. . *J Biol Chem* 275: 30326 - 30334, 2000.

92. **Milsom WK**. Phylogeny of CO2/H chemoreception in vertebrates. *Respiratory physiology and Neurobiology* 131: 29 - 41, 2002.

93. **Mulkey DK, Stornetta RL, Weston MC, Simmons JR, Parker A, Bayliss DA, and Guyenet PG**. Respiratory control by ventral surface chemoreceptor neeurons in rats. *Nature Neuroscience* 7: 1360-1369, 2004.

94. **Nakamura Y, and Takahashi T**. Developmental changes in potassium currents at the rat calyx of Held presynaptic terminal. *The Journal of physiology* 581: 1101-1112, 2007.

95. **Nattie E**. CO2, Brainstem chemoreceptors and breathing. *Progress in Neurobiology* 59: 299-331, 1999.

96. **Nattie E, and Li A**. Central chemoreception 2005: a brief review. *Auton Neurosci* 126-127: 332-338, 2006.

97. **Nattie EE**. Central chemosensitivity, sleep, and wakefulness. *Respiration Physiology* 129: 257-268, 2001.

98. **Nattie EE**. Diethyl pyrocarbonate inhibits rostral ventrolateral medullary H + sensitivity. *J Appl Physiol* 64: 1600-1606, 1988.

99. **Nattie EE**. The retrotrapezoidal nucleus and the 'drive' to breathe. *The Journal of Physiology* 2006.

100. **Nattie EE, and Adams JM**. DIDS decreases CSF HCO3- and increases breathing in response to CO2 in awake rabbits. *J Appl Physiol* 64: 397-403, 1988.

101. **Nattie G, and Li A**. Multiple central chemoreceptor sites: cell types and function in vivo. *Adv Exp Med Biol* 605: 343-347, 2008.

102. **Necakov A, Peever JH, Shen L, and Duffin J**. Acetazolamide and respiratory chemosensitivity to CO2 in the neonatal rat transverse medullary slice. *Respiratory physiology and Neurobiology* 132: 279-287, 2002.

103. **Neubauer JA, and Martin AA**. Contribution of Carbonic Anhydrase to CO_2 chemosensitivity in cultured ventral medullary neurons- Ventral brainstem mechanisms and control of respiration and blood presure. *Marcel Dekker Inc NY* edited by C. Ovid Trouth, Richard M Millis, Heidrun F. Kiwull-Schone and Marianne E. Schlafke: 551 - 561, 1994.

104. **Nottingham S, Leiter JC, Wages P, Buhay S, and Erlichman JS**. Developmental changes in intracellular pH regulation in medullary neurons of the rat. *AJP - Regulatory Integrative Comparative Physiology* 281: R1940-R1951, 2001.

105. **Oyamada Y, Andrzejewski M, M¸ckenhoff K, Scheid P, and Ballantyne D**. Locus coeruleus neurones in vitro: pH-sensitive oscillations of membrane potential in an electrically coupled network. *Respiration Physiology* 118: 131-147, 1999.

106. **Pappenheimer JR, Fencl V, Heisey SR, and Held D**. Role of cerebral fluids in control of respiration as studied in unanesthetized goats. *AJP - Legacy* 208: 436-450, 1965.

107. **Pineda J, and Aghajanian GK**. Carbon dioxide regulates the tonic activity of locus coeruleus neurons by modulating a proton- and polyamine-sensitive inward rectifier potassium current. *Neuroscience* 77: 723-743, 1997.

108. **Plata C, Meade P, Vázquez N, Hebert S, and Gamba G**. Functional properties of the apical Na+-K+-2Cl– cotransporter isoforms. . *J Biol Chem* 277: 11004 - 11012, 2002.

109. **Putnam RW, Conrad SC, Gdovin MJ, Erlichman JS, and Leiter JC**. Neonatal maturation of the hypercapnic ventilatory response and central CO_2 chemosensitivity. *Respiratory physiology and Neurobiology* 149: 165-179, 2005.

110. **Putnam RW, Filosa JA, and Ritucci NA**. Cellular mechanisms involved in CO_2 and acid signaling in chemosensitive neurons. *AJP - Cell Physiology* 287: 1493-1526, 2004.

111. **Putney LK, Denker SP, and Barber DL**. THE CHANGING FACE OF THE Na+/H+ EXCHANGER, NHE1: Structure, Regulation, and Cellular Actions. *Annual Review of Pharmacology and Toxicology* 42: 527-552, 2003.

112. **Remmers JE**. A century of control of breathing. *American Journal of Respiratory Critical Care Medicine* 172: 6 - 11, 2005.

113. **Remmers JE, Torgerson C, Harris M, Perry SF, Vasilakos K, and Wilson RJA**. Evolution of central respiratory chemoreception: a new twist on an old story. *Respiration Physiology* 129: 211 - 217, 2001.

114. **Ren J, and Greer JJ**. Modulation of Respiratory Rhythmogenesis by Chloride-Mediated Conductances during the Perinatal Period. *Journal of Neuroscience* 26: 3721-3730, 2006.

115. **Ribas-Salgueiro JL, Gaytan SP, Pasaro R, and Ribas J**. Highly H+-sensitive neurons in the caudal ventrolateral medulla of the rat. *Journal of Physiology* 549: 181 - 194, 2003.

116. **Richerson GB**. Response to CO_2 of neurons in the rostral ventral medulla in vitro. *Journal of Neurophysiology* 73: 933 - 944, 1995.

117. **Richerson GB**. Serotonergic neurons as carbon dioxide sensors that maintain ph homeostasis. *Nat Rev Neurosci* 5: 449-461, 2004.

118. **Richerson GB, Wang W, Hodges MR, Dohle CI, and Diez-Sampedro A**. Homing in on the specific phenotype(s) of central respiratory chemoreceptors. *Experimental Physiology* 90: 259-269, 2005.

119. **Ridderstråle Y, and Wistrand PJ**. Membrane-associated carbonic anhydrase activity in the brain of CA II-deficient mice. *Journal of Neurocytology* 29: 263-269, 2000.

120. **Rinzel J**. Excitation dynamics: insights from simplified membrane models. *Fed Proc* 44: 2944 - 2946, 1985.

121. **Ritucci NA, Chambers-Kersh L, Dean JB, and Putnam RW**. Intracellular pH regulation in neurons from chemosensitivity and nonchemosensitive areas of the medulla. *AJP - Regulatory Integrative Comparative Physiology* 275: R1152-R1163, 1998.

122. **Ritucci NA, Dean JB, and Putnam RW**. Intracellular pH responses to hypercapnia in neurons from chemosensitive areas of the medulla. *AJP - Regulatory Integrative Comparative Physiology* 42: 1997.

123. **Ritucci NA, Dean JB, and Putnam RW**. Somatic Vs. dendritic responses to hypercapnia in chemosensitive locus coeruleus neurons from neonatal rats. *AJP - Cell Physiology* 289: 1094-1104, 2005.

124. **Ritucci NA, Erlichman JS, Leiter JC, and Putnam RW**. The response of membrane potential (V_m) and intracellular pH (pH_i) to hypercapnia in neurons and astrocytes from rat retrotrapezoid nucleus (RTN). *AJP - Regulatory Integrative Comparative Physiology* 289: 2005.

125. **Roberts EL, He J, and Chih C-P**. Rat hippocampal slices need bicarbonate for the recovery of synaptic transmission after anoxia. *Brain research* 875: 171-174, 2000.

126. **Roos A, and Boron WF**. Intracellular pH. *Physiological Reviews* 61: 296 - 434, 1981.

127. **Shams H**. Differential effects of CO2 and H+ as central stimuli of respiration in the cat. *Journal of Applied Physiology* 58: 357-364, 1985.

128. **Solomon IC, and Dean JB**. Gap junctions in CO_2 chemoreception and respiratory control. *Respiratory Physiology and Neurobiology* 131: 155-173, 2002.

129. **Solomon IC, Edelman NH, and Ill MHOn**. CO_2/H^+ chemoreception in the cat pre-Bötzinger complex in vivo. *Journal of Applied Physiology* 88: 1996 - 2007, 2000.

130. **Stewart RE, DeSimone JA, and Hill DL**. New perspectives in a gustatory physiology: transduction, development, and plasticity. *AJP - Cell Physiology* 272: C1-26, 1997.

131. **Summers BA, Overholt JL, and Prabhakar NR**. Augmentation of L-Type Calcium Current by Hypoxia in Rabbit Carotid Body Glomus Cells: Evidence for a PKC-Sensitive Pathway. *Journal of Neurophysiology* 84: 1636-1644, 2000.

132. **Sun M-K, and Reis DJ**. GABA-mediated inhibition of pacemaker neurons of rostral ventrolateral medulla by clonidine in vitro. *European Journal of Pharmacology* 276: 291-296, 1995.

133. **Szabo E, Numata M, Shull G, and Orlowski J**. Kinetic and pharmacological properties of human brain Na+/H+ exchanger isoform 5 in Chinese hamster ovary cells. *J Biol Chem* 275: 6302 - 6307, 2000.

134. **T JM**. The influence of ammonium salts on cell reaction. *J Gen Physiol* 2: 181–187, 1922.

135. **Takakura ACT, Moreira TS, Colombari E, West GH, Stornetta RL, and Guyenet PG**. Peripheral chemoreceptor inputs to retrotrapezoid nucleus (RTN) CO2-sensitive neurons in rats. *The Journal of Physiology* 572: 503-523, 2006.

136. **Thomas T, and Spyer KM**. ATP as mediator of mammalian central CO_2 chemoreception. *Journal of Physiology* 523: 441 - 447, 2000.

137. **Trouth CO, Odek-Ogunde M, and Holloway JA**. Morphological observations on superficial medullary CO_2 - chemosensitive areas. *Brain research* 246: 1982.

138. **Vandenberg CA, and Bezanilla F**. A sodium channel gating model based on single channel, macroscopic ionic, and gating currents in the squid giant axon. *Biophysical journal* 60: 1511-1533, 1991.

139. **Vorstrup S, Jensen KE, Thomsen C, Henriksen O, Lassen NA, and Paulson OB**. Neuronal pH regulation: constant normal intracellular pH is maintained in brain during low extracellular pH induced by acetazolamide--31P NMR study. *J Cereb Blood Flow Metab* 9: 417-421, 1989.

140. **Wang W, Pizzonia JH, and Richerson GB**. Chemosensitivity of Rat medullary raphe neurons in primary tissue culture. *Journal of Physiology* 511: 433-450, 1998.

141. **Wang W, and Richerson GB**. Changes in glucose do not alter baseline firing rate or chemosensitivity of serotonin neurons cultured from the medullary raphe. *Respir Physiol Neurobiol* 157: 235-241, 2007.

142. **Wang W, Tiwary JK, Bradley SR, Zaykin AV, and Richerson GB**. Acidosis-Stimulated Neurons of the Medullary raphe are serotonergic. *Journal of Neurophysiology* 85: 2224 - 2235, 2001.

143. **Wegner H, Reeh PW, Brehm S, Kreysel HW, and Steen KH**. Diltiazem blocks the PH-induced excitation of rat nociceptors together with their mechanical and electrical excitability in vitro. *Journal of Neurophysiology* 75: 1-10, 1996.

144. **Weinstein AM**. A Kinetically defined Na^+/K^+ Antiporter within a mathematical model of the rat proximal tubule. *Journal of General Physiology* 105: 617-641, 1995.

145. **Wellner-Keitz MC, and Shaums H**. CO_2 sensitive neurons in organotypic cultures of the fetal rat medulla. *Respiration Physiology* 111: 137-151, 1997.

146. **Wiemann M, and Bingmann D**. Ventrolateral neurons of medullary organotypic cultures: intracellular pH regulation and bioelectric activity. *Respiration Physiology* 129: 57 - 70, 2001.

147. **Wiemann M, Frede S, Bingmann D, Kiwull P, and Kiwull-Schone H**. Sodium/Proton exchanger 3 in the medulla oblongata and set point of breathing control. *American journal of respiratory and critical care medicine* 172: 244-249, 2005.

148. **Wiemann M, Piechatzek L, Gopelt K, Kiwull-Schone H, Kiwull P, and Bingmann D**. The NHE3 inhibitor AVE1599 stimulates phrenic nerve activity in the rat. *J Physiol Pharmacol* 59: 27-36, 2008.

149. **Wiemann M, Schwark JR, Bonnet U, Jansen HW, Grinstein S, Baker RE, Lang HJ, Wirth K, and Bingmann D**. Selective inhibition of the Na+/H+ exchanger type 3 activates CO2/H+-sensitive medullary neurones. *Pflugers Arch* 438: 255-262, 1999.

150. **Wilson RJA, Harris MB, Remmers JE, and Perry SF**. Evolution of air-breathing and central CO_2/H^+ respiratory chemosensitivity: new insights

from an old fish? *The Journal of Experimental Biology* 203: 3505 - 3512, 2000.

151. **Winterstein H**. Chemical control of pulmonary ventilation. III. The reaction theory of respiratory control. *N Engl J Med* 255: 331-337, 1956.

152. **Winterstein H**. The actions of substances introduced into the cerebrospinal fluid and the problem of intracranial chemoreceptors. *Pharmacol Rev* 13: 71-107, 1961.

153. **Winterstein H**. The reaction theory of respiratory regulation. *Experientia* 5: 261-265, 1949.

154. **Winterstein H, and Gokhan N**. [Ammonium chloride acidosis and the reaction theory of respiratory regulation.]. *Arch Int Pharmacodyn Ther* 93: 212-232, 1953.

155. **Xu F, Zhang Z, and Frazier DT**. Microinjection of acetazolamide into the fastigal nucleus augments respiratory output in the rat. *J Appl Physiol* 91: 2342-2350, 2001.

156. **Zhao J, Zhou Y, and Boron WF**. Effect of isolated removal of either basolateral HCO-3 or basolateral CO2 on HCO-3 reabsorption by rabbit S2 proximal tubule. *AJP - Renal Physiology* 285: F359-369, 2003.

Appendix A

A.1 State equations for the transport model

We consider a cell surrounded by an infinite bath with constant concentration of main ions. We apply mass balance to derive the rate of change in cell volume and intracellular concentrations and we incorporate conservation of mass and electroneutrality constraints.

In the model cell volume W (cm^3) is determined by water flux J_w ($cm \cdot s^{-1}$) and is given by

$$\frac{dW}{dt} = -AJ_W , \tag{A.1}$$

where A represents a surface area of 1 cm^2 (positive flux is efflux).

Water flux occurs via osmosis, and it can be computed as

$$J_{\mathrm{W}} = P_{\mathrm{w}} \sum \sigma_j (C^{\mathrm{o}}_j - C^{\mathrm{i}}_j) , \tag{A.2}$$

where C^{o}_j and C^{o}_j are extra and intracellular concentrations (mM) of solute j, σ_j is the reflection coefficient (typically equal to 1) and P_{w} is water "permeability" (2×10^{-7} $cm \cdot s^{-1} \cdot mM^{-1}$). Note that extracellular concentrations are constant and values for these can be found on Table 2.2.

Intracellular solute concentrations are determined by solute flux J_j ($cm \cdot sec^{-1} \cdot mM^{-1}$) and water fluxes, and are given by

$$\frac{W}{A}\frac{dC}{dt} = C^i_j J_W - J_j . \tag{A.3}$$

Our model contains expressions like equation A.3 where subscript j might represent Na^+, K^+, Cl^-, negatively charged particles (i.e., proteins) X^-, zero charge particles (i.e., glucose) Y^0, H^+, H_2CO_3, HCO_3^-, $H_2PO_4^-$, $HPO_4^=$, NH_4^+ and NH_3 as specified by each model description. See appendix C for a description of the numerical method used to solve the system of differential equations.

Ion movement across the cell membrane is consider to follow the Goldman-Hodgkin and Katz (GHK) (28, 52, 65) constant field approximation in the transport model and for transport-excitable cell model. The GHK equation can be informally derived as follows from the Nernst-Planck equation, and flux is given by

$$J_j = P_j z_j U \left[\frac{C^i_j \exp(z_j U) - C^o_j}{\exp(z_j U) - 1} \right], \tag{A.4}$$

where J_j is flux ($mol \cdot cm^{-2} \cdot sec^{-1}$), U is the normalized membrane potential, z_j is valence and P_{j} is permeability ($cm \cdot s^{-1}$). It should be noted that when z_j is zero,

the GHK equation describes simple diffusion. Values for the permeabilities in this model can be found in Table 2.1.

For determination of cell membrane potential, a thermodynamic constraint on solute flow is that at all times the cell and bathing solution must both remain electrically neutral, namely,

$$\sum_j z_j C_j^i = \sum_j z_j C_j^o = 0. \tag{A.5}$$

Net transcellular current I_T (as a function of V) is given by

$$I_T(V) = F\sum_j z_j J_j \,, \tag{A.6}$$

where J_j is total flux of solute j (moles·cm^{-2}·s^{-1}), irrespective of the actual transport mechanism (e.g., passive, active, exchange, co-transport, etc). Implementation of the electroneutrality constrain is done numerically using a root finding algorithm (e.g., Newton's method) that solves for membrane potential such that $I_T(V) = 0$.

A.2 State equations for the transport-excitable cell model

The time course of the membrane potential derived from an equivalent circuit of the cell membrane and using Kirchoff's law is given by the sum of the ionic currents and cell capacitance (c_m)

$$\frac{dV}{dt} = -\frac{1}{c_m}\sum_j I_j \,, \tag{A.7}$$

where t is time (ms) and j denotes the ionic species (the ionic species are defined in the document for each model formulation and include electrogenic components like the Na^+-K^+ ATPase). Ionic channels are transmembrane proteins with aqueous pores through which ions can flow down their electrochemical gradient. The electrical conductance of individual channels may be controlled by gating particles (gates) that switch the channel between open and close states. The gate may sensible to: i) Membrane voltage, ii) intracellular agents(e.g. Ca^{++}, pH) and iii) extracellular agents (e.g NMDA, GABA). When the channels are sensitive to voltage they are said to be voltage gated, the gates are divided in two types: those that activate or open the channel and those that inactivate or close the channel. If the probability of an activation gate being open is denoted by a and the probability of an inactivation gate being open is denoted by b, the the proportion of open channels in the population is $a^p b^q$ where p and q are usually integers that are determined by analysis of current records from voltage-clamp experiments.

The individual ionic currents I_j, whether they are voltage sensitive or not, are described by Ohm's law in the conductance based model (equation A.8 below)

and by the GHK equation in the permeability based model (equation A.9), and can be represented in general by the expressions

$$I_j = \bar{g}_j a^p b^q (V - E_j), \tag{A.8}$$

$$I_j = \bar{P}_j z_j U a^p b^q \frac{(C_j^i \exp(z_j U) - C_j^o)}{\exp(z_j U) - 1} F z_j, \tag{A.9}$$

where V is membrane potential (mV), E is the Nernst equilibrium potential (mV), $\bar{g}_j$ is the maximum conductance (nS), $\bar{P}_j$ represents maximum permeability in (cm·s^{-1}), C_j^i and C_j^o are the intracellular and extracellular concentrations respectively (mM), and U is the normalized potential.

Our model assumes instantaneous activation of the fast Na^+ current (I_{Na})and a linear relation between the K^+ activation gate (n) and the Na^+ inactivation gate (h). Thus, for I_{Na} the activation/inactivation kinetics represented by $a^p b^q$ in equations A.8 and A.9 is given by $m_\infty^3(1-n)$ where m_∞ is the steady-state activation function (see equation A.10 below). The fast potassium current (I_K) has only and activation gate (n), thus $q = 0$ and the function is given by n^4. Finally, the voltage insensitive leak currents $I_{Na,l}$ and $I_{K,l}$ (have p and q equal to zero) so they do not have activation/inactivation functions.

The dynamics of the gating variable n is described according to

$$\frac{dn}{dt} = \frac{n_\infty - n}{\tau_n}, \tag{A.10}$$

and the steady state value of the activation functions m and n is described by:

$$m_\infty = \frac{1}{1 + \exp[(V - \theta_m)/\sigma_m]}, \tag{A.11}$$

$$n_\infty = \frac{1}{1 + \exp[(V - \theta_n)/\sigma_n]}, \tag{A.12}$$

and the voltage dependent time constant for the n gate is given by

$$\tau_n = \frac{\bar{\tau}_n}{\cosh[(V - \theta_n)/2\sigma_n]}, \tag{A.13}$$

where m_∞ and n_∞ are a sigmoid with half-activation (at $V = \theta_m$ *or* $V = \theta_n$) and slope proportional to $1/\sigma_m$ or $1/\sigma_n$ respectively. τ_n is a bell-shaped curve with a maximum at $V = \theta_n$ of $\bar{\tau}_n$ and half width determined by σ_n.

A.3 Unit Analysis for the models

The units used for all model descriptions in this document are fundamentally the same (see list of symbols at the begging of the document). However there a few changes that differ form one model to another and might generate some confusion to the unexperienced reader:

1. The transport model uses units of seconds [s] for time. Dynamics of transport phenomena usually are well captured by this time scale, in particular changes that take place during acid-base perturbations are in the order of minutes. So as one computes fluxes (J = permeability [$cm^{-2} \cdot s^{-1}$] × concentration [$mmol \cdot lt^{-1}$]) in the transport model the units come out in $\mu mol \cdot cm^{-2} \cdot s^{-1}$ and the units of volume are cm^3 so the rate of change of concentration ($dC/dt = A[cm^2] \times J[\mu mol \cdot cm^{-2} \cdot s^{-1}]/W[cm^3]$) is $mmol \cdot L^{-1} \cdot s^{-1}$.
2. The transport-excitable model uses units of miliseconds for time, so the fluxes are in $nmol \cdot cm^{-2} \cdot ms^{-1}$ (note that this will give the same amount of flux as the transport model) but the volume is mm^3, so the rate of change in concentration is scaled to $mmol \cdot L^{-1} \cdot ms^{-1}$
3. The HH model in chapter 4 has voltage in units of mV and conductance in nS, so current is given in (pA) for a single neuron (total cell capacitance 21 (pF). The transport-excitable model has currents in units $\mu C \cdot cm^{-2} \cdot s^{-1}$ ($\mu A \cdot cm^{-2}$) so cell capacitance is defined in $\mu F \cdot cm^{-2}$, so for comparison of the currents and the curve fitting section, we scaled them by cell capacitance, so both models yield currents in $pA \cdot pF^{-1}$.

Appendix B- Cell membrane transport elements

B.1 The Na^+-K^+ ATPase

The description of the Na^+-K^+ ATPase used here is taken from (87) an implements a model of the pump in which $3Na^+$ are exchanged for $2K^+$. An additional feature of this model is the voltage dependency of the pump current at different levels of C^o_{Na} a property measured and reported by (49). The pump current is given by:

$$i_p = i_{max} f_{NaK} \frac{1}{1+(K_{Na}/C^i_{Na})^{3/2}} \frac{C^o_K}{C^o_K + K_K} \tag{B.1}$$

where

$$f_{NaK} = \frac{1}{1+0.1245\exp[-U/10]+0.052\exp[(C^o_{Na}/67.3)-\exp(U)]} \tag{B.2}$$

where i_{max} is maximum pump current (μA/μF), K_{Na} and K_K are the half saturations concentrations for Na^+ and K^+ respectively (mM), C^i_{Na} ,C^o_{Na} and C^o_K and intra and extracellular concentration of Na^+ and K^+ respectively (mM), and U is the normalized potential. Parameters for the Na^+-K^+ ATPase can be found in Table 2.1.

B.2 Buffering Capacity

The transport model

In the transport model the intrinsic buffering capacity of the cell is given by three buffers systems in equilibrium:

$$CO_2 + H_2O \xleftrightarrow{k_h/K_d} H_2CO_3 \xleftrightarrow{K_{HCO3}} H^+ + HCO_3^- \tag{B.3}$$

$$H_2PO_4^- \xleftrightarrow{K_{HPO4}} H^+ + HPO_4^= \tag{B.4}$$

$$NH_4^+ \xleftrightarrow{K_{NH3}} H^+ + NH_3 \tag{B.5}$$

The total buffer concentration in each one of the systems is given by:

$$B_{Bicarbonate} = C_{H_2C0_3} + C_{HC0_3^-} \tag{B.6}$$

$$B_{Phosphate} = C_{H_2P0_4^-} + C_{HP0_4^=} \tag{B.7}$$

$$B_{Ammonia} = C_{NH_4^+} + C_{NH_3} \tag{B.8}$$

the total acid concentration of acid (C_{HT}) would be given by

$$C_{HT} = C_{H^+} + C_{H_2CO_3} + C_{H_2PO_4^-} + C_{NH_4^+} \tag{B.9}$$

The equilibrium constant for each one of the buffers dictates that at equilibrium:

$$K_j = \frac{C_{H^+} C_A}{C_{HA}} \tag{B.10}$$

where j denotes the buffer system and *A* and *HA* stands for the weak acid and associated base in each one of the reactions in the system described by equations B.3 to B.5. Then, knowing the equilibrium constants for each one of the buffer systems *K* (eq. B.10) and the total acid concentration C_{HT} (eq. B.9) it is possible to find the concentration of protons C_H that adhere to the isohydric principle. The solution has the following form:

$$C_{HT} = C_{H^+} + \sum_j \frac{C_{H^+} B_j}{C_{H^+} + K_j} \tag{B.11}$$

where j denotes the buffer system and *B* and *K* are the respective total buffer concentration (eqs. B.6 - B.8) and the equilibrium constants for each one of the systems (eq. B.10).

The flux of H_2CO_3 (mM) is given by the balance of the hydration/dehydrations rates of CO_2 and adjusted by volume/area ratio so it is consistent with the expression in eq. A.4:

$$J_{H_2CO_3} = \frac{W}{A}(C^i_{H_2CO_3} k_d - C_{CO_2} k_h) \tag{B.12}$$

Note that equation B.12 is special case of equation A.4 when $z = 0$, and equation B.12 could be rewritten as :

$$J_{H_2CO_3} = P_{H_2CO_3}(C^i_{H_2CO_3} - C^o_{H_2CO_3}) \tag{B.13}$$

where $P_{H_2CO_3} = W \cdot k_d / A$ which is an interesting way to see how carbonic anhydrase speeds up the reaction described in equation B.3. Also note that using equations B.6 to B.8 in combination with equation B.11 allows to compute the concentration of HA and A for each one of the buffers during the simulation.

The transport-excitable model

In the transport-excitable cell model only bicarbonate is consider as a buffer and the rationale presented before for the three buffers is maintained but a few modifications are necessary:

In this scenario the total amount of acid (HT) is given by:

$$C^i_{HT} = C^i_H + C^i_{H_2CO_3} \tag{B.14}$$

and the total amount of buffer (AT) is:

$$C_{AT} = C_{H_2CO_3} + C_{HCO_3^-} \tag{B.15}$$

at equilibrium we know that:

$$K = \frac{C_{H^+} C_{HCO_3^-}}{C_{H_2CO_3}} \tag{B.16}$$

where K is the equilibrium constant for the reaction, and combining equations B. 15 and B.16 and solving for bicarbonate and carbonic acid, we find that

$$C_{HCO_3^-} = C_{AT}\left(\frac{K}{C_{H^+} + K}\right) \tag{B.17}$$

and

$$C_{H_2CO_3} = C_{AT}\left(\frac{C_{H^+}}{C_{H^+} + K}\right) \tag{B.18}$$

and substituting these expression back in equation B.14 and solving for H^+, we get:

$$(C_{H^+})^2 + C_{H^+}\left(K + C_{AT} + C_{HT}\right) - KC_{HT} = 0 \tag{B.19}$$

which can be solved using the quadratic formula.

The expressions for the rate of change for total acid and total buffer are as follows:

$$\frac{dC^i_{HT}}{dt} = \frac{A}{W}\left(C^i_{HT} J_w - J_{H_2CO_3} - J_{H^+}\right) \tag{B.20}$$

and

$$\frac{dC^i_{AT}}{dt} = \frac{A}{W}\left(C^i_{AT} J_w - J_{H_2CO_3} - J_{HCO_3^-}\right) \tag{B.21}$$

The flux of carbonic acid is computed as described in the previous section. The flux of H^+ and HCO_3^+ follow the same analysis of any other charge particle and include the fluxes through the particular exchangers.

B.3 The Sodium Hydrogen Exchanger (NHE)

The NHE model is based on published kinetics(144) and (5) (NHE1), (149) (NHE3) and (7) (NHE1,MHE3 and NHE5). The transporter has binding site that competes for Na^+, NH_4^+ and H^+, can move hydrogen or ammonium out of the cell in exchange for sodium, see Figure B.1. Ion binding is rapid relative to membrane translocation; binding is assumed in equilibrium. The model incorporates an internal modifier (not shown on figure) that enhances the transport (increases the permeation coefficient for each one of ions p_{Na}, p_H, and p_{NH4}) in response to a rise in intracellular H^+, an experimental finding in renal

microvillus vesicles (4) Intracellular acidification causes an increase in Na^+ flux via the exchanger. The modifier is described by two parameters in the original Weinstein paper: f_M (= 2) is the factor rise in p_{Na}, *and* k (= 1×10^{-6} M) is the C_H^i producing half-maximal effect. A third parameter, f_m that was used in the original definition of the modifier (see equation B.26) has no use in this model and therefore is set to zero.

All the parameters with the exception of *k and* E_{NHE} (total amount of carrier) were adapted from the original NHE model (4). For the kinetic formulation, the authors used experimental data from renal microvillus membrane vesicles to find the kinetic properties of the exchanger (4). In our model, k was adjusted to fit more recent experimental data for each one of the isoforms. Thus, to estimate k for the NHE1 we used published kinetic properties (5) and also an elegant study that compares the activity of NHE1, NHE3 and NHE5 in terms of pH sensitivity (7). k for the NHE3 in our model was estimated from experiments comparing the sensitivity of three different isoforms of the NHE transfected into chinese hamster ovary cells termed AP-1(1) and adjusted using other experimental measurements (7). Finally k for NHE5 was fitted from studies using NHE-deficient PS120 brain rat cells to characterize NHE5 kinetic (7).

In the mathematical model the fluxes of Na^+, H^+ and NH_4^+ through the exchanger are given by:

$$J_{NHE}^{Na} = -\left(\frac{p_H E_{NHE}}{s}\right)\left(p_{Na}(C_{Na}^o C_H^i - C_{Na}^i C_H^o) + p_{NH4}(C_{Na}^o C_{NH4}^i - C_{Na}^i C_{NH4}^o)\right) \quad \text{(B.22)}$$

$$J_{NHE}^{H} = -\left(\frac{p_H E_{NHE}}{s}\right)\left(p_{Na}(C_{Na}^i C_H^o - C_{Na}^o C_H^i) + p_{NH4}(C_H^o C_{NH4}^i - C_H^i C_{NH4}^o)\right) \quad \text{(B.23)}$$

$$J_{NHE}^{HN4} = -\left(\frac{p_H E_{NHE}}{s}\right)\left(p_{Na}(C_{Na}^i C_{NH4}^o - C_{Na}^o C_{NH4}^i) + p_{NH4}(C_{NH4}^o C_H^i - C_{NH4}^i C_H^o)\right) \quad \text{(B.24)}$$

$$\begin{aligned} s = {} & (1 + C_{Na}^o + C_H^o + C_{NH4}^o)(p_{Na} C_{Na}^i + p_H C_H^i + p_{NH_4} C_{NH4}^i) + \\ & (1 + C_{Na}^i + C_H^i + C_{NH4}^i)(p_{Na} C_{Na}^o + p_H C_H^o + p_{NH_4} C_{NH4}^o) \end{aligned} \quad \text{(B.25)}$$

where E_{NHE} is total amount of the transporter (an adjustable paramater) and the internal modifier affects the permeabilities by a factor m, where:

$$m = \frac{f_M C_H^i + f_m k}{C_H^i + k} \quad \text{(B.26)}$$

B.4 The Chloride Bicarbonate Exchanger (AE)

Kinetics of an anion exchanger by (23), are incorporated into the model. The transporter has a binding site for Cl^- and HCO_3^-, the rates constants (k_1-k_{12}) (see Table A.2) are appropriate for rat distal tubule, and the values are

thermodynamically consistent; zero net transport occurs when $C^o_{HCO3}C^o_{Cl} = C^i_{HCO3}C^i_{Cl}$ see Figure B.2.

The transporter also has an internal modifier site (not shown on Figure B.2) that binds to Cl^- or HCO_3^-, occupancy of the site effectively reduces the amount of functional enzyme, thereby reducing net transport. Parameters were obtained from human red blood cells experiments by (50).

Assuming that the reaction cycle is at steady state the system of differential equations representing the rate of change of enzyme occupancy can be reduced to a linear system of algebraic equations, and noting that the total amount of enzyme is zero, the system can be organized as follows:

$$\begin{bmatrix} k_1C^o_{Cl} & -k_2 & 0 & 0 & 0 & 0 & -k \\ 0 & k_9 & -k_{10} & 0 & 0 & 0 & -k \\ 0 & 0 & k_6 & -k_5C^i_{Cl} & 0 & 0 & -k \\ 0 & 0 & 0 & k_7C^i_{HCO3} & -k_8 & 0 & -k \\ 0 & 0 & 0 & 0 & k_{12} & -k_{11} & -k \\ -k_3C^o_{HCO3} & 0 & 0 & 0 & 0 & k_4 & -k \\ 1 & 1 & 1 & 1 & 1 & 1 & 0 \end{bmatrix} \begin{bmatrix} j_1 \\ j_2 \\ j_3 \\ j_4 \\ j_5 \\ j_6 \\ J_{AE} \end{bmatrix} = \begin{bmatrix} 0 \\ 0 \\ 0 \\ 0 \\ 0 \\ 0 \\ e_t \end{bmatrix} \quad \text{(B.27)}$$

where,

$$k = \frac{1}{1 + C^i_{Cl} / k_{Cl} + C^i_{HCO3} / k_{HCO_3}} \quad \text{(B.28)}$$

The flow of chloride through the exchanger (J_{AE}) is equal and opposite in direction to the HCO_3^- flux, and it is found by solving the linear system of equations.

B.5 The Sodium, Potassium, Chloride Cotransporter (NKCC)

A Kinetic model of the NKCC2 cotransporter (88, 90) is incorporated into the model (see Table B.3 for parameters and Figure B.3 for kinetic diagram), based on reports thats this particular isoform is expressed in neurons (114). Other quantitative descriptions of the Na^+-K^+-Cl^- cotransporter have been reported (10) and they include off-binding/on-binding rates constants and translocation rates constants very similar to one defined by Lytle and Mc Manus (88). We, however, used a newer and simplified version by Marcano and colleagues in which sequential binding of the ions, first Na^+ then Cl^- then K^+ and finally Cl^-, happens on the extracellular compartment before a transformational change of the enzyme takes place, and the scheme reverses on the cytosol effectively moving the ions inside the cell in an electroneutral fashion(90). The rate constants and binding constants were taken from published data collected from experiments

measuring Rb^+ uptake in transfected *Xenopus* oocytes (108), and the parameter values are thermodynamically consistent. E_{NKCC} (the total amount of enzyme) is defined below in the section about volume regulation.

Assuming that the reaction cycle is at steady state the system of differential equations representing the rate of change of enzyme occupancy can be reduced to a linear system of algebraic equations, and noting that the total amount of enzyme is constant, the system can be organized as follows:

$$\begin{bmatrix} k_{on} & -k_1 & 0 & 0 & 0 & 0 & 0 & 0 & 0 & 0 & -1 \\ 0 & k_{on}C^o_{Cl} & -k_2 & 0 & 0 & 0 & 0 & 0 & 0 & 0 & -1 \\ 0 & 0 & k_{on}C^o_{K} & -k^o_3 & 0 & 0 & 0 & 0 & 0 & 0 & -1 \\ 0 & 0 & 0 & k_{on}C^o_{Cl} & -k_4 & 0 & 0 & 0 & 0 & 0 & -1 \\ 0 & 0 & 0 & 0 & k_{ff} & -k_{bf} & 0 & 0 & 0 & 0 & -1 \\ 0 & 0 & 0 & 0 & 0 & k_1 & -k_{on}C^i_{Na} & 0 & 0 & 0 & -1 \\ 0 & 0 & 0 & 0 & 0 & 0 & k_2 & k_{on}C^i_{Cl} & 0 & 0 & -1 \\ 0 & 0 & 0 & 0 & 0 & 0 & 0 & k^i_3 & k_{on}C^i_{K} & 0 & -1 \\ 0 & 0 & 0 & 0 & 0 & 0 & 0 & 0 & k_4 & k_{on}C^i_{Cl} & -1 \\ 0 & 0 & 0 & 0 & 0 & 0 & 0 & 0 & 0 & k_{fe} & -1 \\ -k_{be} & 1 & 1 & 1 & 1 & 1 & 1 & 1 & 1 & 1 & 0 \end{bmatrix} \begin{bmatrix} j_1 \\ j_2 \\ j_3 \\ j_4 \\ j_5 \\ j_6 \\ j_7 \\ j_8 \\ j_9 \\ j_{10} \\ J_{NKCC} \end{bmatrix} = \begin{bmatrix} 0 \\ 0 \\ 0 \\ 0 \\ 0 \\ 0 \\ 0 \\ 0 \\ 0 \\ 0 \\ E_{NKCC} \end{bmatrix} \quad \text{(B.29)}$$

solution of the linear systems gives the flux of Na^+, K^+ and Cl^- (J_{NKCC}) through the cotransporter. The ions are moved to the intracellular compartment under most physiological conditions in a 1:1:2 (Na^+:K^+:Cl^-) stoichiometry.

B.6 The Potassium, Chloride Cotransporter (KCC)

Kinetics of the KCC1 were assumed to follow the same kinetic description as the NKCC cotransporter, so the structure of the model follows the one presented in he previous section and uses the model proposed by Marcano and colleagues(90). See Figure B.4 and Table B.4 for a diagram and the associated parameters. Data from experiments measuring Rb^+ uptake in *Xenopus* oocytes was used to estimate the rate constants (91). The cotransporter has a binding site for K^+ and Cl^-, and the values are thermodynamically consistent. E_{KCC} (the total amount of the transporter) is defined below in the section about volume regulation.

Assuming that the reaction cycle is at steady state the system of differential equations representing the rate of change of enzyme occupancy can be reduced to a linear system of algebraic equations, and noting that the total amount of enzyme is constant, the system can be organized as follows:

$$\begin{bmatrix} k_{on}C^{o}_{K} & -k_1 & 0 & 0 & 0 & 0 & -1 \\ 0 & k_{on}C^{o}_{Cl} & -k_2 & 0 & 0 & 0 & -1 \\ 0 & 0 & k_f & -k_f & 0 & 0 & -1 \\ 0 & 0 & 0 & k_1 & -k_{on}C^{i}_{K} & 0 & -1 \\ 0 & 0 & 0 & 0 & k_2 & -k_{on}C^{i}_{Cl} & -1 \\ -k_e & 0 & 0 & 0 & 0 & k_e & -1 \\ 1 & 1 & 1 & 1 & 1 & 1 & 0 \end{bmatrix} \begin{bmatrix} j_1 \\ j_2 \\ j_3 \\ j_4 \\ j_5 \\ j_6 \\ J_{KCC} \end{bmatrix} = \begin{bmatrix} 0 \\ 0 \\ 0 \\ 0 \\ 0 \\ 0 \\ E_{KCC} \end{bmatrix} \quad \text{(B.30)}$$

solution of the linear systems gives the flux of K^+ and Cl^- (J_{KCC}) through the cotransporter. The ions are removed from the intracellular compartment under most physiological conditions in a 1:1 (K^+:Cl^-) stoichiometry.

B.7 Control of cell Volume

The NKCC and KCC not only provide the means in the model for Cl^- regulation, but they are known to be involved in volume regulation in different tissues (10). In addition, there is evidence that respiratory neurons have sensitivity to Cl^- mediated currents that depend on C^{o}_{K} (114). Therefore, we decided to implement an active mechanism for regulation of the level of expression of these sources of Cl^- fluxes.

We assumed that cell volume changes are being minimized by the cell machinery, and osmotic perturbations should reflect in gradual and not very extensive changes in cell volume and that this elements should compensate for changes seen with out their presence. To achieve this we implemented a simple approach that assumes that the amount of expression of the enzyme for both cotransporters is a function of cell volume (see Figure B.5). The function has a lower limit (E^{MIN}_{NKCC}, E^{MIN}_{KCC}) and an upper limit (E^{MAX}_{NKCC} and E^{MAX}_{KCC}) that determine the slope, or the rate of change of enzyme expression as volume changes. So, for the NKCC as cell volume diminishes from a set point (V_{set} - base line cell volume) the amount of expression of the enzyme augments until it reaches the maximum value. The increase in NKCC expression brings into the cell Cl^- along with Na^+ and K^+ and drives water into cell, compensating for the original decrease in cell volume. Similarly, as cell volume increases from the base line level the amount of expression of the KCC augments until it reaches the maximum value. The increase in KCC activity removes Cl^- from the cell K^+ and drives water out of the cell, compensating for the original increase in cell volume.

Thus, To find E^{MIN}_{NKCC}, E^{MIN}_{KCC} we assumed no volume regulation ($E^{MIN}_{NKCC} = E^{MAX}_{NKCC}$ and $E^{MIN}_{KCC} = E^{MAX}_{KCC}$) and carefully adjusted the level of the enzyme for both cotransporters to achieve a Cl^- level around 15mM and a volume of 0.3 cm^3. The increased Cl^- concentration is important for the efficiency of these

cotransporters in cell volume regulation; in Figure B.6 we show a simulation of HA at two different levels of Cl^-, and verified that increased levels have better effect in volume regulation. We found that $E_{NKCC}^{MIN} = 1\times10^{-4}$ and $E_{KCC}^{MIN} = 5\times10^{-11}$ provided the desired C_{Cl}^{i}.

To estimate E_{NKCC}^{MAX} we initially increased the osmolarity of the extracellular solution, causing the cell to shrink and recorded the change in cell volume (see Figure B.7 up), we then gradually increased the amount of E_{NKCC}^{MAX} effectively increasing the slope of function and increasing volume regulation capabilities, we stop when a compensation of 60% in cell volume (compensation of the change observed with out volume regulation) occurred after a 10 mOsm hypertonic challenge and recorded E_{NKCC}^{MAX} as the suggested value for the model.

Similarly, to estimate E_{KCC}^{MAX} we initially decreased the osmolarity of the extracellular solution, causing the cell to swell and recorded the change in cell volume (see Figure B.7 down), we then gradually increased the amount of E_{KCC}^{MAX} effectively increasing the slope of function and increasing volume regulation capabilities, we stop when a compensation of 60% in cell volume occurred after a 10 mOsm hypotonic challenge and recorded E_{KCC}^{MAX} as the suggested value for the model . We found $E_{NKCC}^{MAX} = 1\times10^{-3}$ and $E_{KCC}^{MAX} = 1\times10^{-6}$ to be reasonable values of the parameters.

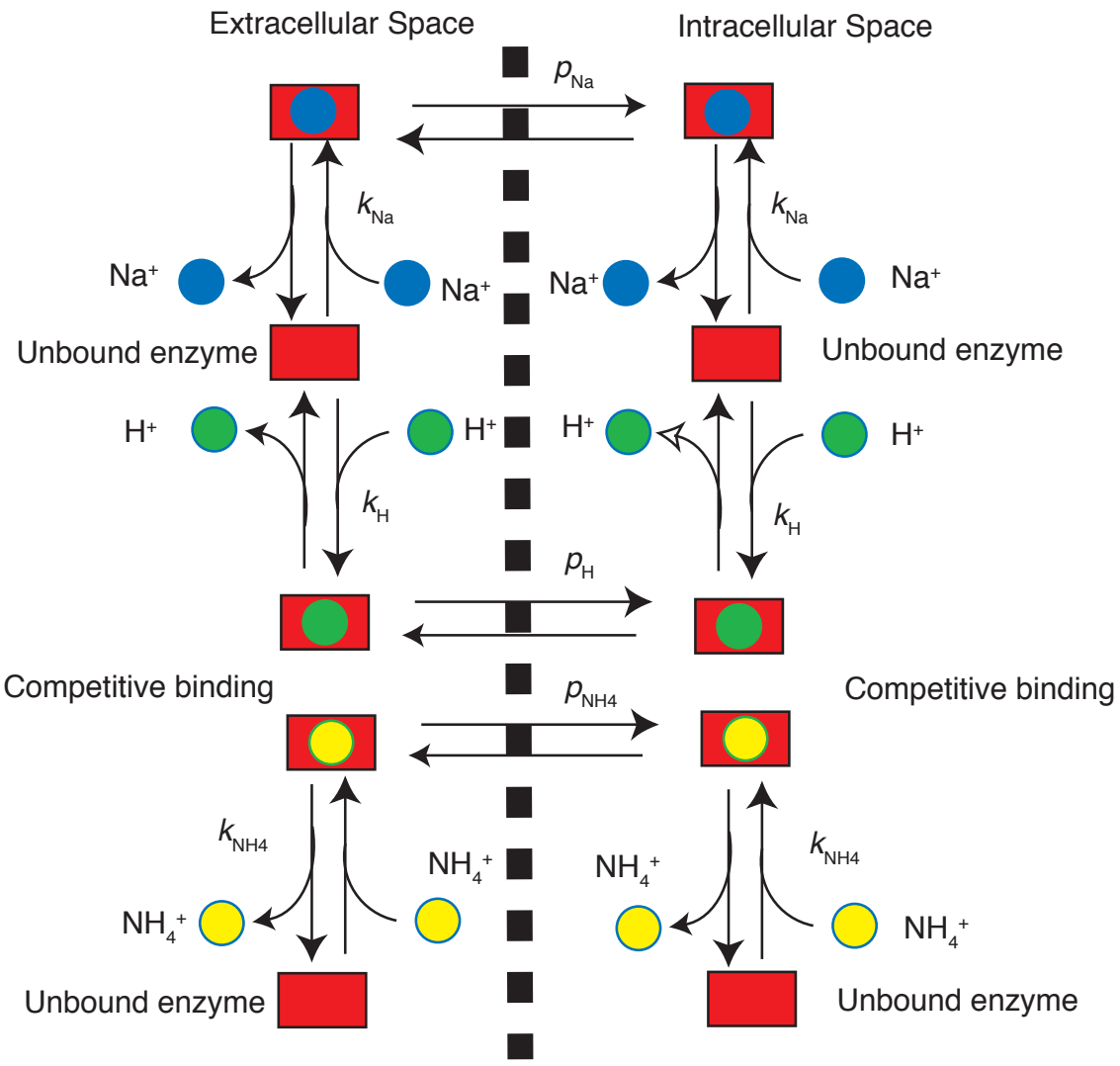

Figure B.1 Kinetic diagram of the NHE.

The transporter has binding site that competes for Na^+, NH_4^+ and H^+, and can move hydrogen or ammonium out of the cell in exchange for sodium.

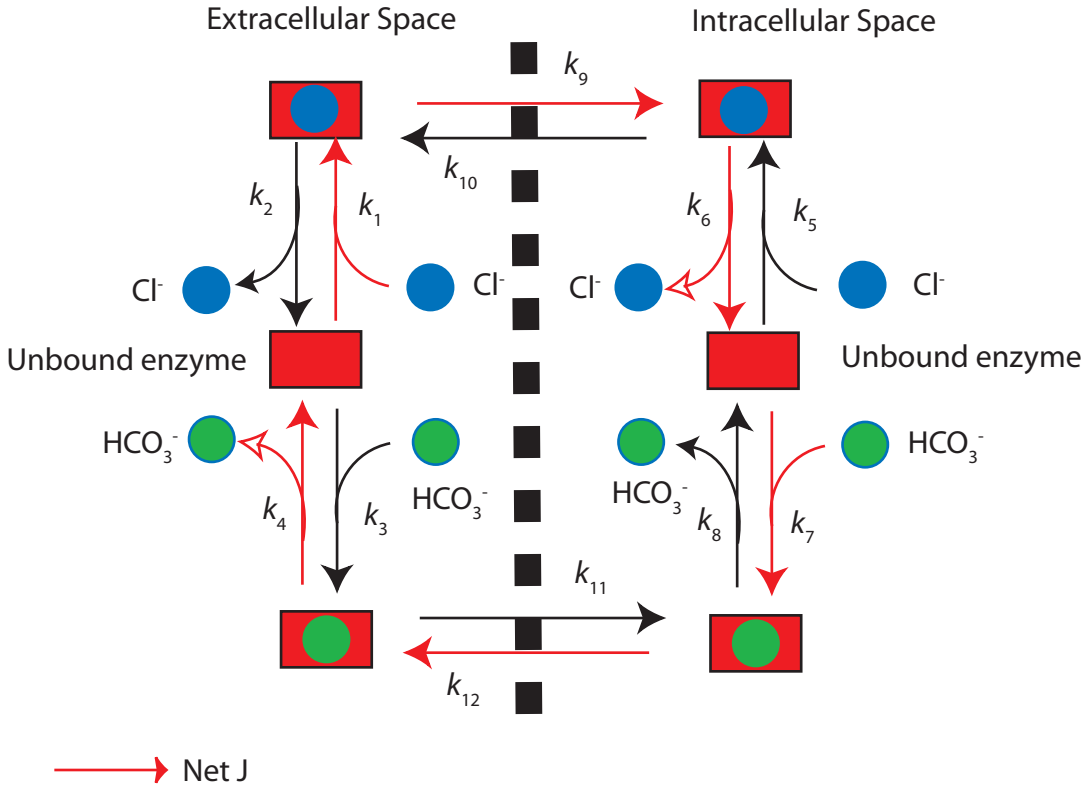

Figure B.2 Kinetic diagram of the AE.

The transporter has a binding site for Cl^- and HCO_3^-, the rates constants (k_1-k_{12}) (see Table B.2) are appropriate for rat distal tubule, and the values are thermodynamically consistent; zero net transport occurs when $C^o_{HCO3}C^o_{Cl} = C^i_{HCO3}C^i_{Cl}$.

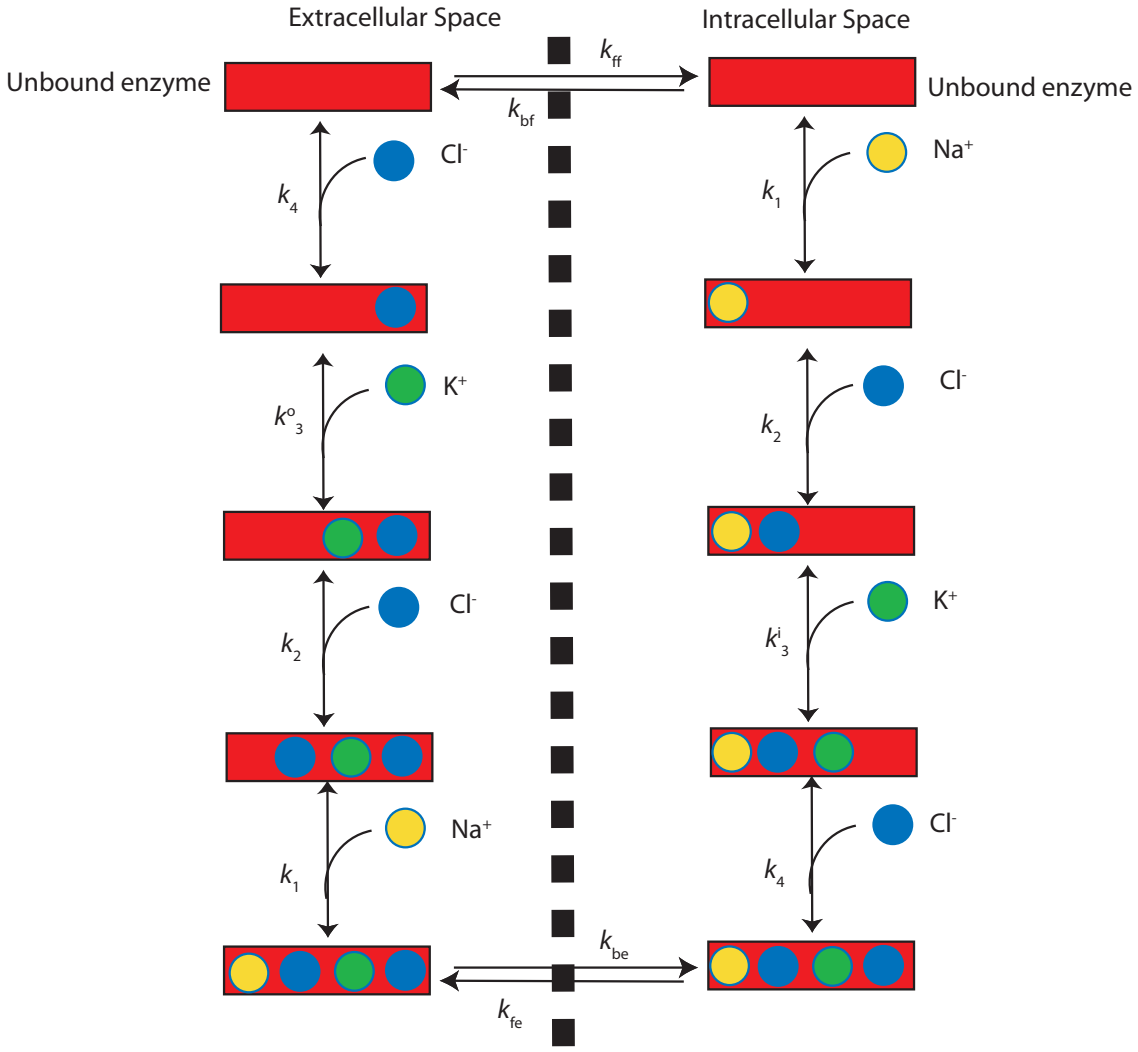

Figure B.3 Kinetic diagram of the NKCC.

Kinetics of the NKCC2 cotransporter are incorporated into the model (see Table B.3 for parameters). The cotransporter has a binding site for Na^+, K^+ and Cl^- . the rates constants and binding constants were taken form published data collected from experiments measuring Rb^+ uptake in transfected *Xenopus* oocytes (108), and the values are thermodynamically consistent. E_{NKCC} (the total amount of enzyme) is defined in the section about volume regulation.

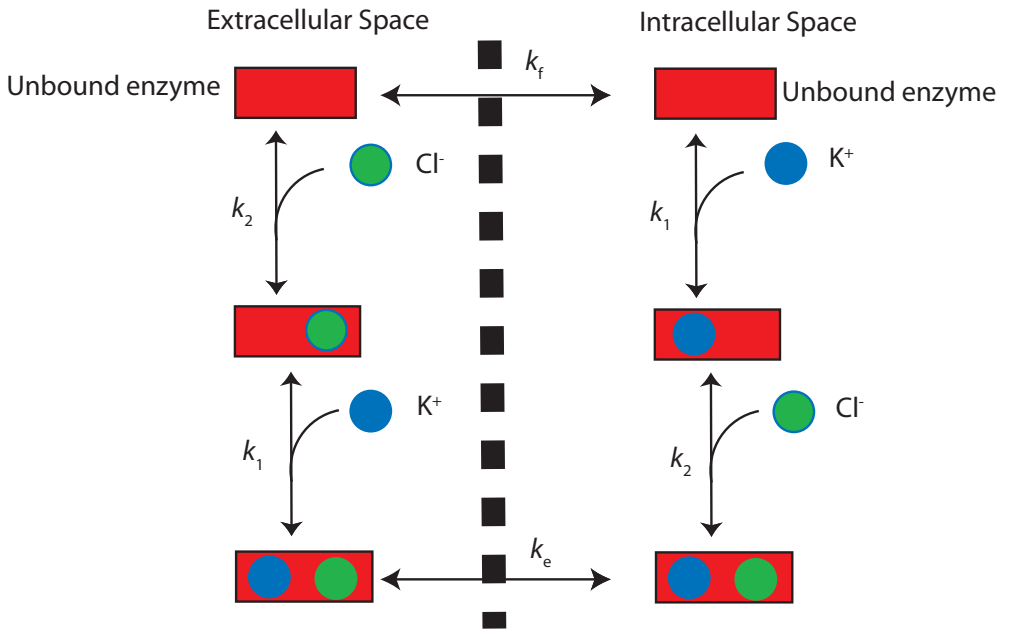

Figure B.4 Kinetic diagram of the KCC.

Kinetics of the KCC1 were assumed to follow the same kinetic description as the NKCC cotransporter, so the structure of the model follows the one presented by (90) see Table B.4 for parameters. Data from experiments measuring Rb^+ uptake in *Xenopus* oocytes (91) was used to estimate the rate constants. The cotransporter has a binding site for K^+ and Cl^-, and the values are thermodynamically consistent. E_{KCC} (the total amount of enzyme) is defined in the section about volume regulation.

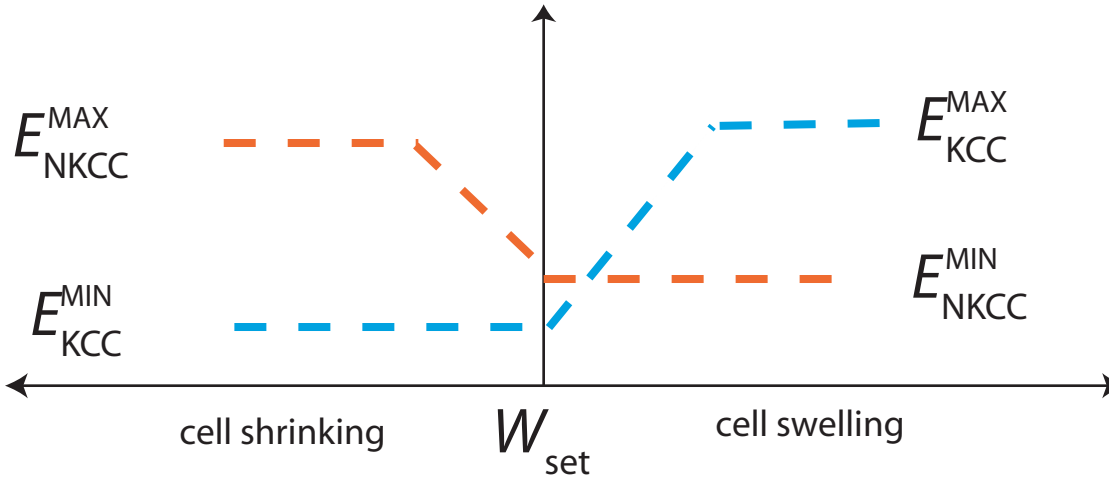

Figure B.5 Empirical function to adjust E_{NKCC} and E_{KCC} models as function of cell volume.

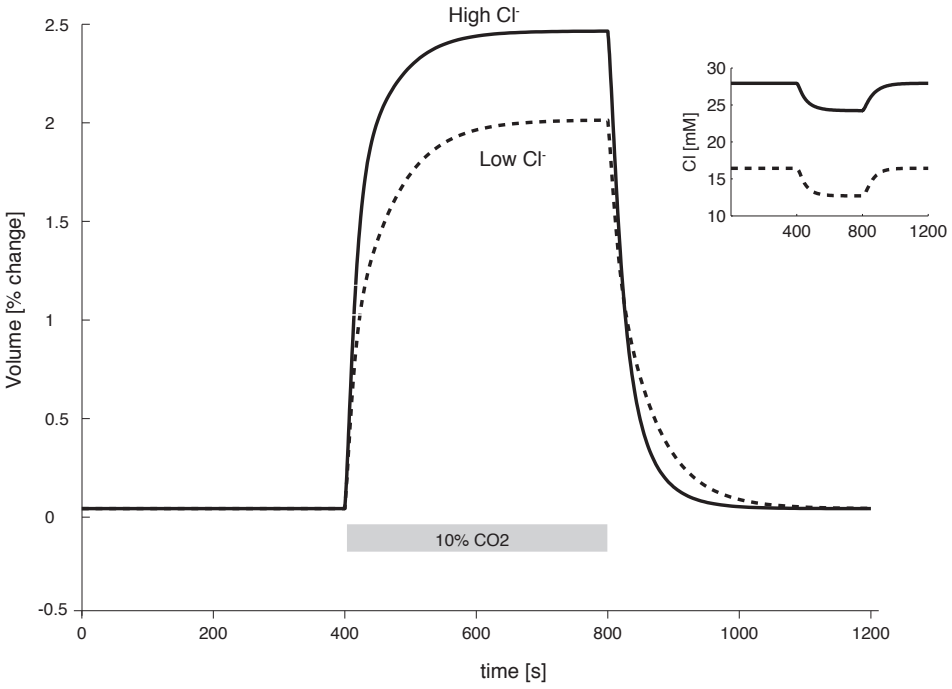

Figure B.6 Cl^- levels impact the ability to regulate cell volume.

The level of volume compensation is a function of intracellular Cl^- concentration. An increase in intracellular Cl^- from 15 mM (dashed line) to 28 mM (solid line) produces a change from 76% compensation to 80% compensation during HA.

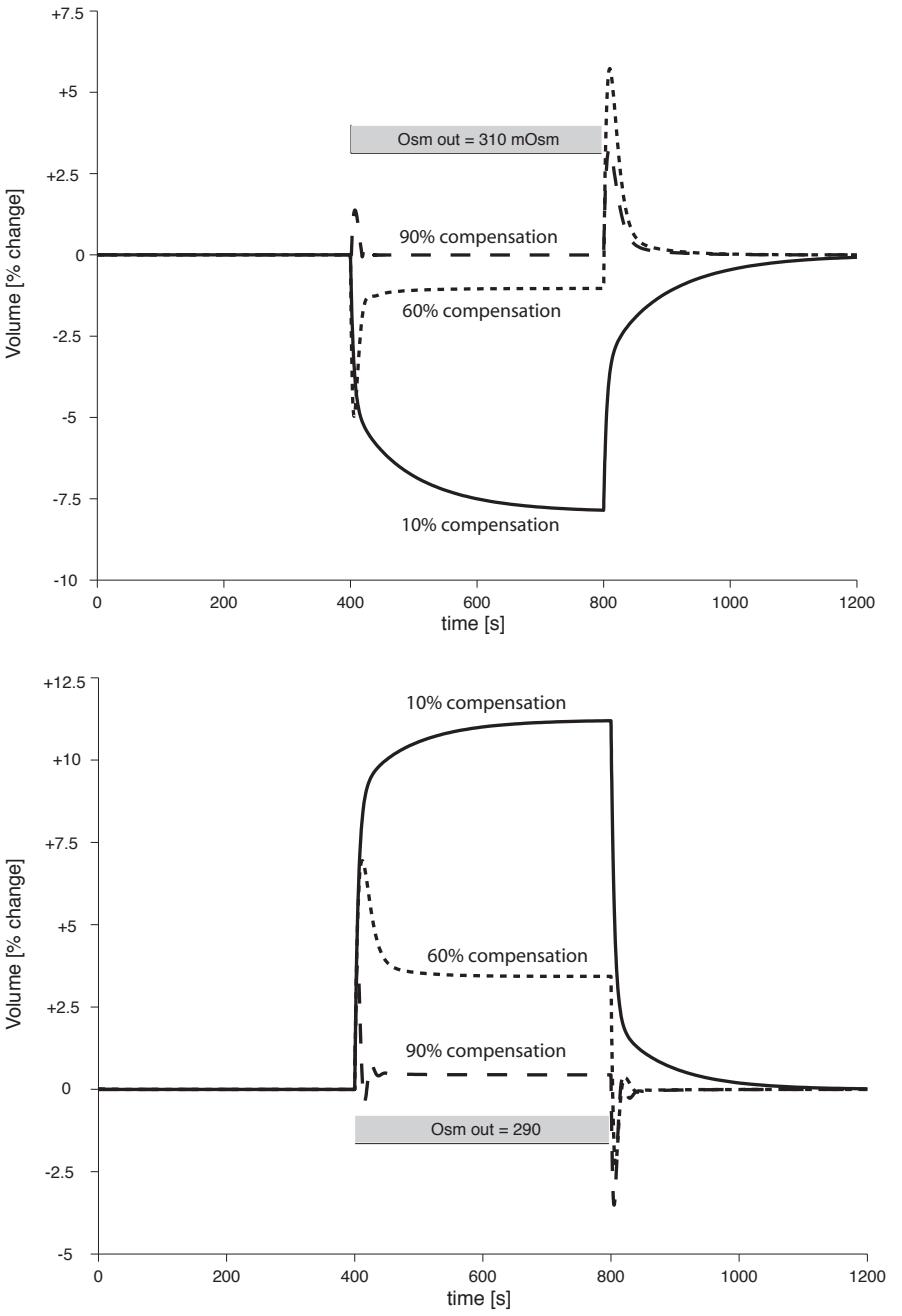

Figure B.7 Setting the E_{NKCC}^{MAX} and E_{KCC}^{MAX}

As the osmolarity of the extracellular compartment was increased (up) or decreased (down), cell volume was compensated by increasing the activity of the NKCC (left) and KCC(right). We assumed that 60% compensation (i.e., only 60% of the changed observed without volume regulation) was a reasonable level of NKCC and KCC-mediated cell volume regulation.

Table B.1 Parameters and diagram for a mathematical model of the NHE.

parameter [units] (description)	Value
k_{Na} [mM] (equilibrium constant)	30
k_{H} [mM] (equilibrium constant)	7.2×10^{-7}
k_{NH4} [mM] (equilibrium constant)	27
p_{Na} [cm·s^{-1}] (Permeation coefficient)	1.6×10^{-3}
p_{H} [cm·s^{-1}] (Permeation coefficient)	4.8×10^{-2}
p_{NH4} [cm·s^{-1}] (Permeation coefficient)	1.6×10^{-3}
E_{NHE} [M·cm^{-3}] (total amount of carrier-not shown in Figure B.1)	(see text)
f_M [mM] (not shown in Figure B.1)	2
f_m [mM] (not shown in Figure B.1)	0
k [mM] (not shown in Figure B.1)	(see text)

Table B.2 Parameters and diagram for a mathematical model of the AE.

parameter [units] (description)	Value
k_1[L·mmol^{-1}·s^{-1}](binding rate constant)	1×10^5
k_2[s^{-1}](rate constant)	7.87×10^6
k_3[L·mmol^{-1}·s^{-1}] (binding rate constant)	1×10^5
k_4[s^{-1}] (rate constant)	8.28×10^6
k_5[L·mmol^{-1}·s^{-1}] (binding rate constant)	1×10^5
k_6[s^{-1}] (rate constant)	7.87×10^6
k_7[L·mmol^{-1}·s^{-1}] (binding rate constant)	1×10^5
k_8[s^{-1}] (rate constant)	8.28×10^6
k_9[s^{-1}] (rate constant)	5.14×10^5
k_{10}[s^{-1}] (rate constant)	9.26×10^4
k_{11}[s^{-1}] (rate constant)	3.24×10^5
k_{12}[s^{-1}] (rate constant)	5.83×10^4
k_{Cl}[mmol·L^{-1}] (dissociation constant of the modifier site not shown in Figure B.2)	5.28×10^3
k_{HCO3}[mmol·L^{-1}] (dissociation constant of the modifier site not shown in Figure B.2)	4.23×10^2

Table B.3 Parameters and diagram for a mathematical model of the NKCC.

parameter [units] (description)	Value
k_{on} [L·mol^{-1}·s^{-1}] ion binding rate constant (not shown in Figure B.3)	400
k_1 [L·mol^{-1}] (on-off binding rate constant)	881.25
k_2 [L·mol^{-1}] (on-off binding rate constant)	18433
k^i_3 [L·mol^{-1}] (on-off binding rate constant)	33613
k^o_3 [L·mol^{-1}] (on-off binding rate constant)	11204
k_4 [L·mol^{-1}] (on-off binding rate constant)	7326
k_{ff} [s^{-1}] Translocation constant	50.4
k_{bf} [s^{-1}] Translocation constant	3.7
k_{fe}[s^{-1}]Translocation constant	37.8
k_{be}[s^{-1}] Translocation constant	1544.73

Table B.4 Parameters and diagram for a mathematical model of the KCC.

parameter [units] (description)	Value
k_{on} [L·mol^{-1}·s^{-1}] (ion binding rate constant -not shown in Figure B.4)	400
k_1 [L·mol^{-1}] (on-off binding rate constant)	42288
k_2 [L·mol^{-1}] (on-off binding rate constant)	4608
k_f [s^{-1}] Translocation constant	908
k_e [s^{-1}] Translocation constant	378

Appendix C- Numerical methods

All computations for the transport model were performed on an apple MacBook Pro with a 2.93 GHz intel core 64 bit duo processor on a Mac OSX 10.6 platform running Matlab and Simulink version R2009a (Mathworks Natick, MA). Some of the simulations using the transport-excitable model (which can last up to 8 hours before achieving steady-sate) were performed on a workstation with 3GHz dual quad-core 64 bit Intel Xeon processors on a Fedora Core 8 Linux platform running Matlab and Simulink version R2009a.

Solution of state equations for the transport model

The system of nonlinear differential equations (including the diffusion delay) was solved numerically using an explicit Runge-Kutta (4,5) formula and the Dormand-Prince algorithm, built-in in Matlab® (Matlab, Mathworks Natick, MA.) in a function known as ODE45 solver. The absolute and relative tolerance for the solver were set at 10^{-6} and 10^{-3} respectively.

Solution of state equations for the transport-excitable model

The system of nonlinear differential equations was solved numerically using ODE15s, a built-in function in Matlab®, which is a multi-step variable order solver based on numerical differentiation formulas designed for stiff systems. The absolute and relative tolerance for the solver were set at 10^{-6} and 10^{-3} respectively.

Solution of equation describing total cell current in transport model to find membrane potential

In the transport model the cell is assumed to maintain electroneutrality, so no net charge accumulation is possible. Net transcellular current I_T (as a function of V) is given by

$$I_T(V) = F\sum_j z_j J_j \,, \tag{C.1}$$

where J_j is total flux of solute *j*. We used the built in function *fzero* in Matlab® to find V so I_T is equal to zero. The algorithm implemented in *fzero*, was originated by T. Dekker and uses a combination of bisection, secant, and inverse quadratic interpolation methods. The function tolerance and variable tolerance were set 10^{-8} and 10^{-4} respectively.

Solution of equations describing total acid concentration in transport model to find C_H^i

In the transport model the concentration of intracellular H^+ (C_H^i) is given by

$$C_{HT} = C_{H^+} + \sum_j \frac{C_{H^+} B_j}{C_{H^+} + K_j}, \quad \text{(C.2)}$$

where C_{HT} is the total acid concentration, j denotes the buffer system and B and K are the respective equilibrium constant and total buffer concentration. C_H^i is found using *fzero* as described in the previous section for membrane potential. The function tolerance and variable tolerance were set 10^{-8} and 10^{-4}, respectively.

Implementation of diffusion delay

The change in concentration of any species in the model that resulted as consequence of an introduced perturbation was reflected by the following equation:

$$\frac{dC}{dt} = \tau(C_{bulk} - C), \quad \text{(C.3)}$$

where C_{bulk} refer to the level of the perturbation (i.e., increased level in CO_2), τ is the time constant and C is the concentration of the specie or species. τ was chosen to be 10 s, which represents approximately a 100 µm unstirred layer for diffusion. Equation C.3 was solved using the methods described for the state variables of the transport model.

Implementation of the phase-plane diagrams

The phase-plane analysis elaborated for the conductance and permeability based models was based on the two dimensional system defined by:

$$F(V,n) = -\frac{1}{c_m}\sum I_j, \quad \text{(C.4)}$$

$$G(V,n) = \frac{n_\infty - n}{\tau_n}, \quad \text{(C.5)}$$

where I_j (ionic current) is defined by equation A.8 and A.9 for the conductance based model and permeability based model respectively, and n_∞ and τ_n are described by equations A.11 and A.12 respectively. The functions F and G replaced the original derivatives defined in equations A.7 and A.10 to denote them as a system of non-linear equations that can be solved in more traditional ways. The curves in Figure 4.6 denoted as nullclines are the solution of F and G when they are equal to zero. Note that when G is equal to zero $n = n_\infty$ and F was solved for n as function of V and the roots of the polynom that creates this re-arrangement were computed for each value of V between -80 and 40. The roots of the polynom were computed using the built in function *roots* in Matlab® that computes the eigenvalues of the companion matrix.

The arrows in phase-plan diagram represents the strength of the vector filed for the range of the state-variables. Each arrow is result of a vector that denotes the solution of $F + G$ evaluated at particular choices of V and n.

Computation of Jacobian and eigenvalues

The Jacobian of the system C.4 - C.5 was obtained using the symbolic toolbox in Matlab® and the built in function *jacobian*. The eigenvalues when specific points were used to evaluate the Jacobian, were computed using the built in function in Matlab® *eig* that uses the standard package LAPACK with several different routines that change given the nature of the matrix.

Solution of the system to find steady-states

The points that simultaneously make the system of equations C.4 - C.5 equal to zero are the fixed points of the system. To find the set of point (V,n) such that F and G are simultaneously equal to zero, we used Newton's method. Newton's method was implemented by computing the analytic Jacobian of the two dimensional system using the symbolic toolbox in Matlab®. The function tolerance and variable tolerance were set to 10^{-5}. The eigenvalues of the Jacobian obtained when the matrix was evaluated at steady-state were used to determine stability of the fixed point as explained in chapter 4.